

1992

The branching fraction of long-lived kaon going to muon-anti-muon

Michael David Chapman
College of William & Mary - Arts & Sciences

Follow this and additional works at: <https://scholarworks.wm.edu/etd>



Part of the [Physics Commons](#)

Recommended Citation

Chapman, Michael David, "The branching fraction of long-lived kaon going to muon-anti-muon" (1992). *Dissertations, Theses, and Masters Projects*. Paper 1539623816.
<https://dx.doi.org/doi:10.21220/s2-ztsa-fe04>

This Dissertation is brought to you for free and open access by the Theses, Dissertations, & Master Projects at W&M ScholarWorks. It has been accepted for inclusion in Dissertations, Theses, and Masters Projects by an authorized administrator of W&M ScholarWorks. For more information, please contact scholarworks@wm.edu.

INFORMATION TO USERS

This manuscript has been reproduced from the microfilm master. UMI films the text directly from the original or copy submitted. Thus, some thesis and dissertation copies are in typewriter face, while others may be from any type of computer printer.

The quality of this reproduction is dependent upon the quality of the copy submitted. Broken or indistinct print, colored or poor quality illustrations and photographs, print bleedthrough, substandard margins, and improper alignment can adversely affect reproduction.

In the unlikely event that the author did not send UMI a complete manuscript and there are missing pages, these will be noted. Also, if unauthorized copyright material had to be removed, a note will indicate the deletion.

Oversize materials (e.g., maps, drawings, charts) are reproduced by sectioning the original, beginning at the upper left-hand corner and continuing from left to right in equal sections with small overlaps. Each original is also photographed in one exposure and is included in reduced form at the back of the book.

Photographs included in the original manuscript have been reproduced xerographically in this copy. Higher quality 6" x 9" black and white photographic prints are available for any photographs or illustrations appearing in this copy for an additional charge. Contact UMI directly to order.

U·M·I

University Microfilms International
A Bell & Howell Information Company
300 North Zeeb Road, Ann Arbor, MI 48106-1346 USA
313/761-4700 800/521-0600



Order Number 9236122

The branching fraction of $K_L \rightarrow \mu\bar{\mu}$

Chapman, Michael David, Ph.D.

The College of William and Mary, 1992

Copyright ©1993 by Chapman, Michael David. All rights reserved.

U·M·I
300 N. Zeeb Rd.
Ann Arbor, MI 48106

THE BRANCHING FRACTION OF $K_L \rightarrow \mu\bar{\mu}$

A Dissertation
Presented to
The Faculty of the Department of Physics
The College of William and Mary

In Partial Fulfillment
Of the Requirements for the Degree of
Doctor of Philosophy

by
Michael David Chapman
May 1992

THE BRANCHING FRACTION OF $K_L \rightarrow \mu\bar{\mu}$

Michael David Chapman

May 1992

WMHEG-92-1

**Supported in part by the
National Science Foundation
Grant PHY-8921480**

APPROVAL SHEET

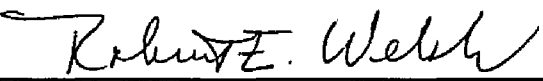
This dissertation is submitted in partial fulfillment of
the requirements for the degree of

Doctor of Philosophy



Michael D. Chapman

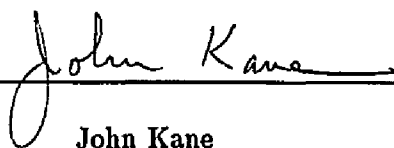
Approved, May 1992



Robert E. Welsh



Morton Eckhause



John Kane



Marc T. Sher



Robert Orwoll

Department of Chemistry

DEDICATION

**To my parents, William and Ursula
for their support and patience**

Contents

Acknowledgements	vii
List of Tables	viii
List of Figures	ix
Abstract	xii
1 Introduction	1
2 Theoretical Background	4
2.1 The GIM Mechanism	4
2.2 The Unitarity Limit	5
2.3 Heavy Quark Masses	6
2.4 Beyond the Standard Model	8
3 Experimental Apparatus	11
3.1 Overview	11
3.2 BNL B-5 Beamline	12
3.3 E791 Spectrometer	13
3.4 Drift Chambers	14
3.5 Trigger Scintillator Counters	15
3.6 Čerenkov Counters	15
3.7 Lead Glass Array	17
3.8 Muon Hodoscope	18
3.9 Muon Rangefinder	18
4 Data Acquisition	20
4.1 Overview	20

4.2	Level 0 and Level 1 Triggers	21
4.3	Level 2 Trigger	22
4.4	Level 3 Trigger	22
4.5	Readout Electronics	24
4.5.1	Time-to-Digital Converters	24
4.5.2	Amplitude-to-Digital Converters	25
4.5.3	Latch Modules	25
4.6	Readout Architecture	25
4.7	Acquisition Rates	27
5	Data Reduction	29
5.1	Overview	29
5.2	Track Finding	29
5.2.1	Pattern Recognition	29
5.2.2	PASS 1	32
5.3	Track Fitting	34
5.3.1	QT Fitting	34
5.3.2	FT Fitting	35
5.3.3	PASS 2	37
5.4	Event Identification	38
5.4.1	Track Counter Association	38
5.4.2	Event Stripping	45
6	Data Analysis	47
6.1	Overview	47
6.2	$K_L \rightarrow \mu\bar{\mu}$ Sample	48
6.2.1	Event Quality Cuts	48
6.2.2	Track Quality Cuts	50
6.2.3	Particle Identification	52
6.2.4	Number of $K_L \rightarrow \mu\bar{\mu}$	52
6.3	$K_L \rightarrow \pi\bar{\pi}$ Normalization Sample	55
6.3.1	Event Selection Cuts	55
6.3.2	Number of $K_L \rightarrow \pi\bar{\pi}$	56
6.4	Corrections Factors	56

6.4.1	Level 1 Efficiency	57
6.4.2	Level 3 Efficiency	57
6.4.3	Hadronic Interactions	58
6.4.4	K_s Contamination	58
6.4.5	Particle ID Efficiencies	60
6.5	Geometric Acceptance	61
6.5.1	Standard Monte Carlo	61
6.5.2	Extended Monte Carlo	62
6.6	$K_L \rightarrow \mu\bar{\mu}$ Branching Fraction	64
6.7	Conclusions	67
A	The Muon Rangefinder	68
A.1	Overview	68
A.2	Construction	68
A.2.1	Marble	69
A.2.2	Instrumented Planes	70
A.2.3	Electronics	74
A.3	Particle Identification	75
A.4	Performance	76
A.5	Polarimeter	77
B	The GEANT Monte Carlo Extension	79
	Bibliography	83

ACKNOWLEDGEMENTS

I would like to thank the following people for their contributions to this work:

Dr. Robert E. Welsh, my advisor, for his advice and encouragement.

Dr. John R. Kane and Dr. Morton Eckhause for their help during the experiment, and in proofreading this work.

Fellow graduate students Dr. John Ginkel and Michael Witkowski for their help during the experiment and in the data analysis.

Fellow graduate student Dr. Chris Kenney, for his assistance during the experiment and data analysis. And also for his excellent diagrams of various experimental apparatus taken from his thesis (Figures 8–11,13–16,18,45–48).

Dr. Paul P. Guss, Dr. Donald Joyce, Dr. A. Dayle Hancock, Dr. Yunan Kuang, Dr. Robert J. Whyley and Dr. Rolf G. Winter for their help during the experiment and analysis.

Mr. William Vulcan for his assistance during the experiment, and for his advice.

Dr. Robert A. Orwoll and Dr. Marc T. Sher for their comments on this work.

Ms. Dianne Fannin, Ms. Paula Spratley, and Ms. Sylvia Stout for their help, and for always knowing what needed to be done.

The staff of the BNL AGS facility and Computer Center.

And finally, all of my E791 collaborators: K. Arisaka, L. Auerbach, S. Axelrod, J. Belz, K. Biery, G. Bonneaud, P. Buchholtz, R. Cousins, G. Daniel, M. Diwan, J. Frank, G. Hart, A. Heinson, V. Highland, J. Horvath, G. Hoffman, G. Irwin, T. Kaarsberg, S. Kettell, W. Kinnison, P. Knibbe, J. Konigsberg, J. Kubic, K. Lang, D. Lee, J. Margulies, C. Mathiazhagen, W. McFarlane, R. Mckee, P. Mélése, E. Milner, W. Molzon, D. Ouimette, P. Riley, J. Ritchie, D. Roberts, P. Rubin, A. Schwartz, G. Sanders, M. Sivertz, W. Slater, Q. Trang, J. Urheim, D. Wagner, W. Wales, D. Woycheshin, A. Yamashita and H. Ziock.

List of Tables

1	Previous $K_L \rightarrow \mu\bar{\mu}$ experimental results.	3
2	Physics events classified by L1 trigger.	27
3	PASS1 events written to tape.	34
4	PASS2 events written to tape.	38
5	Comparison of the fraction of events, by Level 1 trigger type, which have missing crates to the fraction of events in the PASS2 input.	49
6	Results of Quality and Track cuts on Minimum Bias Sample	55
7	Summary of Analysis results for FT and QT fitting packages.	64
8	Systematic uncertainties in $B(K_L \rightarrow \mu\bar{\mu})$	66
9	Identification efficiencies for various tight MRG cuts.	76

List of Figures

1	Weak diagram for the $K^+ \rightarrow \mu^+ \bar{\nu}_\mu$ decay mode.	86
2	First and second order weak diagrams for $K_L \rightarrow \mu \bar{\mu}$. A) First order weak, up quark. B) First order weak, charm quark. C) Second order weak, up quark. D) First order weak, charm quark.	87
3	$K_L \rightarrow \gamma\gamma$ contribution to $K_L \rightarrow \mu \bar{\mu}$	88
4	Top mass measurement $K_L \rightarrow \mu \bar{\mu}$ diagrams.	89
5	Bounds on the top quark mass for various models. Figure taken from Buras[20].	90
6	Higgs boson exchange contributions to $K_L \rightarrow \mu \bar{\mu}$	91
7	$K_L \rightarrow \mu \bar{\mu}$ leptoquark diagrams.	92
8	The AGS B-5 beamline.	93
9	Top view of the E791 detector.	94
10	Partial drift chamber cross-section.	95
11	Trigger scintillator bank.	96
12	Side and top view of a Čerenkov counter.	97
13	The lead glass array.	98
14	The muon hodoscope, with iron filter.	99
15	Top and side view of the muon rangefinder.	100
16	Level 0 trigger logic.	101
17	Level 1 trigger logic.	102
18	Overview of the readout architecture.	103
19	PASS1 flowchart.	104
20	PASS2 flowchart.	105
21	TIMEPZ distribution for $K_L \rightarrow \mu \bar{\mu}$ candidates.	106
22	Vertex χ^2 distribution for $K_L \rightarrow \mu \bar{\mu}$ candidates. Dashed line represents Monte Carlo distribution.	107

23	Track χ^2 distribution for $K_L \rightarrow \mu\bar{\mu}$ candidates. Dashed line represents Monte Carlo distribution.	108
24	Front/back momentum match for $K_L \rightarrow \mu\bar{\mu}$ candidates.	109
25	Muon hodoscope confidence level distribution for $K_L \rightarrow \mu\bar{\mu}$ candidates. . .	110
26	MRG actual minus expected stop gap distribution for $K_L \rightarrow \mu\bar{\mu}$ candidates.	111
27	Scatterplot of θ_c^2 versus invariant mass for $K_L \rightarrow \mu\bar{\mu}$ candidates.	112
28	Mass projection of $K_L \rightarrow \mu\bar{\mu}$ scatterplot.	113
29	θ_c^2 projection of $K_L \rightarrow \mu\bar{\mu}$ scatterplot.	114
30	θ_c^2 projection of $K_L \rightarrow \mu\bar{\mu}$ scatterplot.	115
31	Vertex χ^2 distribution for $K_L \rightarrow \pi\bar{\pi}$ candidates. Dashed line represents Monte Carlo distribution.	116
32	Track χ^2 distribution for $K_L \rightarrow \mu\bar{\mu}$ candidates. Dashed line represents Monte Carlo distribution.	117
33	Front/back momentum match for $K_L \rightarrow \pi\bar{\pi}$ candidates.	118
34	$K_L \rightarrow \pi\bar{\pi}$ mass distribution. Dashed line is the Monte Carlo distribution. .	119
35	Reconstructed K_L mass from $K_L \rightarrow \pi\bar{\pi}$ events. Dashed line represents Monte Carlo.	120
36	Reconstructed K_L z -decay vertex from $K_L \rightarrow \pi\bar{\pi}$ events. Dashed line represents Monte Carlo.	121
37	Systematics study for variations of the mass window cut.	122
38	Systematics study for variations of the θ_c^2 cut.	123
39	Systematics study for variations of the front/back momentum match cut. .	124
40	Systematics study for variations of the vertex χ^2 cut.	125
41	Systematics study for variations of the track χ^2 cut.	126
42	Systematics study for variations of the z -decay vertex cut.	127
43	Systematics study for variations of the MHO confidence level cut.	128
44	Systematics study for various subgroups of the data. A) By direction of bend in first magnet. B) By run number. C) BY reconstructed K_L momentum. D) By reconstructed z -decay vertex.	129
45	MRG extrusion cross-section.	130
46	Diagram of a MRG X-plane.	131
47	Diagram of a MRG Y-plane.	132
48	Diagram of the MRG gas system.	133

49	GEANT program flowchart.	134
50	GEANT dynamic storage.	135
51	MCGTEX program flowchart.	136
52	MCGTEX dynamic storage.	137

ABSTRACT

This thesis presents the results of a measurement of the branching fraction of the $K_L \rightarrow \mu\bar{\mu}$ decay. This decay is GIM suppressed in the Standard Model, and provides a useful test of that model. Additionally, the degree of deviation from the unitarity limit provides a useful test for several other models. The experiment was performed at the Brookhaven National Laboratory Alternating Gradient Synchrotron facility. The apparatus consisted of a two-magnet mass spectrometer, together with dual electromagnetic and muon particle identification systems. A total of 281 $K_L \rightarrow \mu\bar{\mu}$ events were observed. Normalizing to the 15,768 $K_L \rightarrow \pi\bar{\pi}$ events observed results in a branching fraction of $\Gamma(K_L \rightarrow \mu\bar{\mu})/\Gamma(K_L \rightarrow \text{all}) = (7.6 \pm 0.5) \times 10^{-9}$.

THE BRANCHING FRACTION OF $K_L \rightarrow \mu\bar{\mu}$

Chapter 1

Introduction

One of the great success stories of the last thirty years is that of the Standard Model. Born in 1964 as an attempt to bring order to the chaotic world of “elementary” particles[1], it has since grown into a comprehensive model of the structure of matter and its interactions. The Standard Model is an experimentally based $SU(3)_C \times SU(2)_L \times U(1)_Y$ gauge theory which successfully accounts for all observed experimental data.

In spite of all its success, the Standard Model has fundamental problems. Several questions arise from the apparent existence of structure among fermions. The basic constituents of fermions, leptons and quarks, are divided into three generations, each consisting of one lepton pair and one quark pair. The first point is the complete absence of the second member of the third generation quark doublet, the top quark. The suppression of flavor-changing neutral currents, and renormalization in weak interaction gauge theory, strongly suggest that quarks come in pairs. Yet no experimental evidence exists for a top quark to accompany the bottom quark. Also missing from the picture is the Higgs boson, which arises from the electro-weak gauge theory accounting for particle mass in the Standard Model. Furthermore, the quark, lepton and Higgs masses are themselves not predicted. Only slightly less worrisome is the very existence of three generations. Why not two, or four or even more generations? Also, does not the existence of these generations, which differ only in mass, possibly argue for further sub-structure, just as mass structure of hadrons implied the existence of quarks? And while CP-violation is allowed under the Standard Model, thanks to the quark mixing angles, they themselves have arbitrary values. Finally, what of gravity, which does not even enter into the Standard Model?

Many theories have been advanced to solve these questions. To aid in the formulation

of these theories, and to determine their validity, requires experiments which push the limits of Standard Model predictions to see if violations occur. One such experiment is E791, performed at Brookhaven National Laboratory. E791 studied three rare kaon decay modes. The primary goal was to search for the $K_L \rightarrow \mu^\pm e^\mp$ decay mode to a sensitivity of 10^{-12} . Since the lepton conservation number is not conserved under this decay, it is strictly forbidden under the Standard Model. Observation of this decay, or evidence for its absence, explores both the generation and mass structure of quarks and leptons[2]. The other decay modes of interest are $K_L \rightarrow e\bar{e}$ and $K_L \rightarrow \mu\bar{\mu}$. Both are permitted under the Standard Model, and their rates can be predicted. $K_L \rightarrow e\bar{e}$ is expected to have a branching fraction of 2.3×10^{-12} , and its observation at a higher rate would indicate new physics processes not anticipated under the Standard Model.

This dissertation is concerned with an experimental determination of the $K_L \rightarrow \mu\bar{\mu}$ decay mode. As with $K_L \rightarrow e\bar{e}$, $K_L \rightarrow \mu\bar{\mu}$ provides a test of the predictive powers of the Standard Model. Additionally, as shall be discussed in the next chapter, it can probe the mass and mixing angles of the top quark. Historically, the experimental evidence for the suppression of this decay mode was instrumental in the development of the Glashow-Iliopoulos-Maiani mechanism, as is also discussed in the next chapter. Table 1 shows the experimental history of $K_L \rightarrow \mu\bar{\mu}$ [3,4,5,6,7]. As can be seen, the uncertainties in the measurements prior to E791 and KEK137 were very large. In order for the $K_L \rightarrow \mu\bar{\mu}$ measurement to be of use in testing the Standard Model, a more accurate measurement is required. Additionally, the 1988 runs for E791 and KEK137 are not in good agreement with each other, nor with the expected rate.

This thesis is organized into six chapters. The second chapter deals with the theoretical concerns underlying $K_L \rightarrow \mu\bar{\mu}$. Chapters 3-5 deal with the E791 experimental layout, data acquisition and data reduction respectively. Finally, the data is analyzed and a final result for the branching fraction is produced in Chapter 6. Two appendices dealing with the details of the muon rangefinder and the computer Monte Carlo programs are also provided.

Authors	Year	Events	$B(K_L \rightarrow \mu\bar{\mu})$
Carithers <i>et al.</i>	1973	6	$12_{-4}^{+8} \times 10^{-9}$
Fukushima <i>et al.</i>	1976	3	$8.8_{-5.5}^{+10.7} \times 10^{-9}$
Shochet <i>et al.</i>	1979	15	$8.1_{-1.8}^{+2.8} \times 10^{-9}$
Inagaki <i>et al.</i> (KEK137)	1989	54	$(8.4 \pm 1.1) \times 10^{-9}$
Mathiazhagen <i>et al.</i> (E791)	1989	87	$(5.8 \pm 0.6 \pm 0.4) \times 10^{-9}$

Table 1: Previous $K_L \rightarrow \mu\bar{\mu}$ experimental results.

Chapter 2

Theoretical Background

2.1 The GIM Mechanism

In the late 1960s, the theoretical work on weak interactions had reached an impasse, which can be illustrated *via* the $K_L \rightarrow \mu\bar{\mu}$ decay. Many of the weak interaction models of the time, including Weinberg-Salam, necessitated the existence of neutral gauge bosons which mediated neutral current processes. These neutral currents were modeled on the charged currents, illustrated by the decay $K^+ \rightarrow \mu^+\bar{\nu}_\mu$ shown in Figure 1. Unfortunately, no neutral current processes had been observed at the time. Even more disastrous was the experimental evidence that strangeness-changing neutral currents did not exist at the expected rates. Taking $K^+ \rightarrow \mu^+\bar{\nu}_\mu$ as a model, $K_L \rightarrow \mu\bar{\mu}$ should occur *via* the first order exchange of a Z^0 boson, as shown in the diagram in Figure 2a, and at roughly the same rate. Yet, then current experiments placed $\Gamma(K_L \rightarrow \mu\bar{\mu}) < 2.1 \times 10^{-7}$ [8]. Including the second order exchange of two W^\pm bosons in the theoretical calculation, as shown in the diagram in Figure 2c, simply made the disagreement worse.

To explain this suppression of $\Delta S = 1$ neutral currents, Glashow, Iliopoulos and Maiani (GIM) postulated the existence of a second quark doublet[9]:

$$\begin{pmatrix} c \\ s \cos \theta_c - d \sin \theta_c \end{pmatrix}$$

to accompany the known quark and lepton doublets:

$$\begin{pmatrix} u \\ s \cos \theta_c - d \sin \theta_c \end{pmatrix} \quad \begin{pmatrix} \nu_e \\ e \end{pmatrix} \quad \begin{pmatrix} \nu_\mu \\ \mu \end{pmatrix}$$

with the new quark flavor referred to as charm (c). Under GIM, the first order weak decay of $K_L \rightarrow \mu\bar{\mu}$ requires a second component encompassing the new doublet, as shown in Figure 2b. The diagrams in Figure 2a and Figure 2b exactly cancel each other[10]. Similarly, the second order exchange requires another diagram including the charm contribution, as shown in Figure 2d. If the mass of the charm and up quarks were identical, these diagrams would also cancel[11]. (NB: While this discussion is limited to the first two quark doublets, it is easily generalized to three or more generations[10].) Thus, the suppression of the $K_L \rightarrow \mu\bar{\mu}$ decay was explained by these fortuitous cancellations. The discovery of the ψ meson in 1974 would vindicate the GIM postulation of the charm quark.

2.2 The Unitarity Limit

The first and second order weak interactions suppressed by GIM are not the only avenues available for $K_L \rightarrow \mu\bar{\mu}$. Figure 3 provides an example of a combination first order weak, fourth order electromagnetic process, involving two photons in an intermediate stage. It is possible, utilizing this process, to relate $\Gamma(K_L \rightarrow \mu\bar{\mu})$ to $\Gamma(K_L \rightarrow \gamma\gamma)$ and hence establish a lower bound on $\Gamma(K_L \rightarrow \mu\bar{\mu})$, referred to as the *unitarity limit*.

In 1970, Martin, de Rafael and Smith calculated the relationship between $\Gamma(K_L \rightarrow \gamma\gamma)$ and $\Gamma(K_L \rightarrow \mu\bar{\mu})$ [12]. Starting with a general expression for the amplitude of $K_L \rightarrow \mu\bar{\mu}$, and assuming CP invariance, Martin *et al.* obtained the following equation:

$$\Gamma(K_L \rightarrow \gamma\gamma) = \frac{M_k}{4\pi} \left(1 - \frac{4m_\mu^2}{M_k^2}\right)^{\frac{1}{2}} |F_2|^2 \quad (1)$$

To obtain a lower bound on $\Gamma(K_L \rightarrow \mu\bar{\mu})$, required knowledge of the form factor F_2 , which Martin *et al.* proceeded to obtain from $\Gamma(K_L \rightarrow \gamma\gamma)$, resulting in the following equation:

$$\begin{aligned} \Gamma(K_L \rightarrow \mu\bar{\mu}) \geq & \frac{M_k}{4\pi} \beta_\mu \left[\frac{\alpha m_\mu}{\sqrt{2} M_2 \beta_\mu} \ln \left(\frac{1 + \beta_\mu}{1 - \beta_\mu} \right) \right. \\ & \left. \left(\frac{4\pi}{M_k} \Gamma(K_L \rightarrow \gamma\gamma) - \frac{\Gamma(K_2 \rightarrow \text{all})}{8M_k} M_k^2 \sigma_{0-1}^{(\gamma\gamma)}(M^2) \right)^{\frac{1}{2}} \right. \\ & \left. - \frac{1}{2\beta_\mu} \left[\beta_\mu M_k \sigma_2(M^2) \right]^{\frac{1}{2}} \left(\frac{\Gamma_2}{M_k} \right) \right]^2 \quad (2) \end{aligned}$$

where $\beta_\mu = (1 - 4m_\mu^2/M_k^2)^{1/2}$, and Γ_2 is the rate for $K_2 \rightarrow \text{all}$ states excluding $\gamma\gamma$. Since the cross-sections $\sigma_2(M^2)$ (total cross-section for $\mu^+\mu^-$ in the 1S_0 state to all final states

other than $\gamma\gamma$) and $\sigma_{0-1}^{(\gamma\gamma)}(M^2)$ (total cross-section for $\gamma\gamma$ to states with angular momentum $J = 0$ and parity $P = -1$) were not measurable, the latter two terms in Equation 2 were dropped. The final relation between $K_L \rightarrow \mu\bar{\mu}$ and $K_L \rightarrow \gamma\gamma$ is then:

$$\frac{\Gamma(K_L \rightarrow \mu\bar{\mu})}{\Gamma(K_L \rightarrow \gamma\gamma)} \geq \alpha^2 \left(\frac{m_\mu}{M_k}\right)^2 \frac{1}{2\beta_\mu} \ln^2 \left(\frac{1+\beta_\mu}{1-\beta_\mu}\right) \quad (3)$$

or $\Gamma(K_L \rightarrow \mu\bar{\mu}) \geq 1.2 \times 10^{-5} \Gamma(K_L \rightarrow \gamma\gamma)$. Substituting the present value for the ratio of $\Gamma(K_L \rightarrow \gamma\gamma)$ to $\Gamma(K_L \rightarrow \text{all})$ of 5.70×10^{-4} [13], one obtains the following lower bound on $K_L \rightarrow \mu\bar{\mu}$:

$$\frac{\Gamma(K_L \rightarrow \mu\bar{\mu})}{\Gamma(K_L \rightarrow \text{all})} \geq 6.8 \times 10^{-9}. \quad (4)$$

Several assumptions were made in deriving Equation 3. The first two, *CPT* invariance and unitarity of the scattering matrices, are fairly safe. The derivation further assumes *CP* invariance, which is violated at low levels for K_L decays. The validity of this assumption was questioned when an early $K_L \rightarrow \mu\bar{\mu}$ measurement[14] appeared to violate the unitarity bound. Several models were proposed which permitted *CP* violation (see Ref [15]). However, these models produced $\Gamma(K_S \rightarrow \mu\mu)$ which were themselves in disagreement with experimental data. The next assumption was that the absorptive portion of the $K_L \rightarrow \mu\bar{\mu}$ amplitude ($\text{abs}F_2$) is dominated by the two photon intermediate state. Martin *et al.* also performed an order-of-magnitude calculation for the contributions of two other intermediate states, $\pi\pi\gamma$ and 3π , to $\text{abs}F_2$ and found their contributions to be less than 10^{-13} , implying that $\gamma\gamma$ domination is a safe assumption. The final assumption, that the absorptive portion of the $K_L \rightarrow \gamma\gamma$ amplitude vanishes, is also considered to be safe[12]. Martin *et al.* determined that corrections to Equation 3 could be as much as 20%.

2.3 Heavy Quark Masses

The unitarity limit provides a lower bound on the rate for $K_L \rightarrow \mu\bar{\mu}$. Any deviation above this limit must, by definition, be due to processes other than the $\gamma\gamma$ process. Thus, a measurement of $\Gamma(K_L \rightarrow \mu\bar{\mu})$ serves to place upper bounds on the rates for other processes. Since the rate of second order weak interactions is dependent on the number and mass of the heavier quarks, $\Gamma(K_L \rightarrow \mu\bar{\mu})$ can be used to predict these quantities.

In 1974, Gaillard and Lee[16] performed just such a calculation based on the mass difference between K_L and K_S , constrained by the experimental value for $\Gamma(K_L \rightarrow \gamma\gamma)$ and

the experimental limit on $\Gamma(K_L \rightarrow \mu\bar{\mu})$, within a four quark model to estimate the mass of the then conjectural charm quark (m_c). Gaillard and Lee obtained the following expression for the K_L - K_S mass difference:

$$m_{K_L} - m_{K_S} \simeq \frac{1}{m_k} \langle \bar{K}^0 | -\mathcal{L}_{eff} | K^0 \rangle \quad (5)$$

where \mathcal{L}_{eff} is the effective Lagrangian. Evaluating $\langle \bar{K}^0 | -\mathcal{L}_{eff} | K^0 \rangle$ results in:

$$\begin{aligned} \frac{m_{K_L} - m_{K_S}}{m_k} &\simeq \frac{\alpha G_F}{4\pi\sqrt{2}} f_k^2 \epsilon_0 \sin^2 \theta_c \cos^2 \theta_c \\ &\simeq \epsilon_0 \times 5 \times 10^{-12} \end{aligned} \quad (6)$$

where $\epsilon_0 = \delta/(m_W^2 \sin^2 \theta_W)$ or

$$\epsilon_0 \simeq 1.4 \times 10^{-3} \quad (7)$$

based on the experimental value for the K_L - K_S mass difference. They proceeded to show that Equation 7 was consistent with either $m_c \simeq m_u$ and large with $m_c - m_u \simeq 1 \text{ GeV}/c^2$, or $m_c \gg m_u$ and $m_c \simeq 1.5 \text{ GeV}/c^2$. Utilizing the non-suppression of $K_L \rightarrow \gamma\gamma$ and the suppression of $K_L \rightarrow \mu\bar{\mu}$ they argued that $m_c \simeq 1.5 \text{ GeV}/c^2$ was the better conclusion. This prediction would agree quite well with the measured mass from the ψ particle discovery two months later[17,18].

The procedure utilized by Gaillard and Lee can be extended to the current six-quark model of Kobayashi and Maskawa (KM)[19], to place bounds on the mass of the, as yet, undiscovered top quark(m_t). As before, one starts with a general expression for the K_L - K_S mass difference[20]:

$$m_{K_L} - m_{K_S} = 2\Re C \langle \bar{K}^0 | [\bar{s}\gamma_\mu(1 - \gamma_5)d]^2 | K^0 \rangle + L.D. \quad (8)$$

where L.D. represents the long-distance contributions, and the first term involves the short-distance function C and the kaon matrix element $M \equiv \langle \bar{K}^0 | \dots | K^0 \rangle$. Buras[20] calculated the value for M using the MIT Bag Model. C is evaluated in the free-quark model, incorporating QCD corrections. For $K_L \rightarrow \mu\bar{\mu}$, the evaluation of C is accomplished *via* the box diagrams illustrated in Figure 4a and 4b, where u_i can be the up, charm or top quarks. The "blob" in Figure 4b consists of several one-loop diagrams, two examples of which appear in Figure 4c. (For a complete list of the diagrams represented by Figure 4b, see Inami and Lim[21].) The result is:

$$|\Re A_t| G(x_t) \eta \leq |s_1 s_3| 0.85 \times 10^{-2} \quad (9)$$

where

$$\begin{aligned}\Re A_t &= -s_1 s_2 (c_1 s_2 c_3 + c_2 s_3 \cos \delta) \\ G(x_t) &= \frac{3}{4} \left(\frac{x_t}{x_t - 1} \right)^2 \ln x_t + \frac{x_t}{4} + \frac{3}{4} \frac{x_t}{1 - x_t}\end{aligned}$$

and $c_i = \cos \theta_i$, $s_i = \sin \theta_i$ and δ are the KM parameters.

From Equation 9, one can proceed along either of two paths. Buras utilized experimental values for c_1 and s_3 , and varied the remaining KM parameters for fixed values of M and m_c to obtain upper bounds on m_t . Figure 5, taken from Buras[20], shows that m_t should lie within a mass region of 30–40 GeV/ c^2 .

The second path is to fix m_t at a given value (provided $m_t > 20$ GeV/ c^2) and determine the bounds on the KM parameters, which Inami and Lee[21] calculated under the assumption $m_t \gtrsim m_W$, and Shrock and Treiman[22] under the assumption $m_t \ll m_W$.

2.4 Beyond the Standard Model

Numerous extensions to the Standard Model have been proposed, in an attempt to explain some of the arbitrary parameters which occur there. Kaon physics, both in the K_L - K_S mass difference and the rare decay rates, often provides a means to test the validity of such extensions. In the next sections, two such theories shall be briefly examined. The first is an extension to the Standard Model, involving minimal changes, the second is a more radical overhaul of the Standard Model.

Extended Higgs

A simple extension of the Standard Model is to incorporate a second Higgs doublet[23]:

$$\begin{pmatrix} \phi_1^+ \\ \phi_1^0 \end{pmatrix} \quad \begin{pmatrix} \phi_2^+ \\ \phi_2^0 \end{pmatrix}$$

resulting in eight Higgs particles. As with the Standard Model, three of the Higgs particles are pseudo-Goldstone bosons, and are taken by the W^\pm and Z^0 bosons, leaving two charged and three neutral physical Higgs particles. Under this model, the fermion mass eigenstates are linear combinations of the gauge eigenstates, based on the fact that they arise from the vacuum expectation values of the Higgs particles. The Higgs particles are capable of mediating flavor-changing currents, including neutral currents. (Recall that for

the Standard Model, only the W^\pm bosons could do so, and that its single neutral Higgs particle is flavor-conserving.)

A lower bound on the Higgs mass(m_H) can be obtained from any of the $K_L \rightarrow \mu\bar{\mu}$ decay modes (as well as for the other dileptonic kaon modes). Figure 6 shows the two flavor-violating processes which contribute to $K_L \rightarrow \mu\bar{\mu}$ from which the following amplitude is obtained by Shanker[23]:

$$\frac{G_F m_b m_\tau}{m_H^2} \bar{\mu}(1 + \gamma_5)\mu(\bar{s}\gamma_5 d + \bar{d}\gamma_5 s). \quad (10)$$

From this, Shanker derives the following equation:

$$\frac{\Gamma(K_L \rightarrow \mu\bar{\mu})}{\Gamma(K_L \rightarrow \text{all})} = 4.6 \times 10^4 \left(\frac{m_b m_\tau}{m_H^2} \right)^2 \quad (11)$$

Incorporating the branching fraction measured in this paper (see Section 6.6), and assuming the Higgs contribution does not exceed the non-absorptive portion of $K_L \rightarrow \mu\bar{\mu}$ results in a bound of $m_H > 4.9 \text{ TeV}/c^2$. However, Shanker assumes a large coupling in Equation 10, using a more reasonable value for the couplings results in a much lower bound on m_H .

A more stringent bound of $m_H > 150 \text{ TeV}/c^2$ arises from the K_L - K_S mass difference. However, this bound assumes no suppression of the Higgs contribution to $m_{K_L} - m_{K_S}$, which is not the case in all models.

Technicolor

One serious problem with the Standard Model is the use of scalar fields to generate particle mass. While these fields accomplish that task, they include quadratic mass divergences which require an unnaturally high degree of precision in the basic parameters of the theory. Technicolor is an attempt to avoid this problem by theorizing the existence of more fundamental particles, called *technifermions*, which constitute both fermions and the gauge bosons[24,25,26,27].

The gauge interactions and technifermions are similar to $SU(3)_c$ color interactions. The model consists of a single doublet of massless technifermions with a new strong interaction (*technicolor*), and which becomes strong at $\sim 1 \text{ TeV}/c^2$. When the technicolor chiral symmetry ($SU(2)_{TC}$) is broken, the result is bound technifermion-antitechnifermion pairs which are pseudo-Goldstone bosons. Some of these replace the Higgs bosons of the Standard Model in providing the masses of the W^\pm and Z^0 bosons. The remaining pairs, hereafter

referred to as *pseudoscalar bosons* are of interest in flavor-violating currents, as discussed below.

Unlike the scalar fields of the Standard Model, this gauge interaction cannot also account for the fermion (quark/lepton) masses. This is accomplished *via* a second gauge group, the *extended gauge group (ETC)*[27], which becomes strong at $\sim 10 \text{ TeV}/c^2$. ETC combines ordinary fermions and technifermions into multiplets in an $SU(3)_{ETC}$ gauge theory. The ordinary fermion masses arise when $SU(3)_{ETC}$ symmetry is broken down to $SU(2)_{TC}$.

The principal interest of technicolor for this paper is a large prediction for flavor-violating currents. Technicolor can produce flavor-violating currents through pseudoscalar bosons and leptoquarks (colored particles which govern quark/lepton conversion). Bounds can be placed on the pseudoscalar boson couplings in a manner similar to that used for the neutral Higgs particles in the preceding section[23]. However, these bounds disagree with experiment. This disagreement may be avoided by postulating that the masses of all like-charge fermions come from the same technifermion-antitechnifermion pair (*monophagy*)[28]. In this case, the pseudoscalars become flavor conserving. Leptoquarks can contribute to $\Gamma(K_L \rightarrow \mu\bar{\mu})$ *via* the diagram illustrated in Figure 7. One can obtain the following relationship for this diagram from the general Hamiltonian[23]:

$$\frac{\Gamma(K_L \rightarrow \mu\bar{\mu})}{\Gamma(K_L \rightarrow \text{all})} = 1.1 \times 10^4 \left(\frac{f^2}{G_F m_P^2} \right)^2. \quad (12)$$

Taking $f \simeq \frac{1}{250}$ produces a bound of $m_P > 1.2 \text{ TeV}/c^2$. Note that the K_L - K_S mass difference does not place limits on leptoquarks, as they mediate flavor-changing processes only.

Chapter 3

Experimental Apparatus

3.1 Overview

The overall purpose of the experiment, the study of rare and forbidden kaon decay modes, dictated the design specifications for E791. A high flux of neutral kaons was required due to the low rate of such decays, but with a low flux of other particles, to prevent overloading the detector. Very good mass resolution was needed primarily to distinguish the two-body decays of interest from the similar, but far more numerous, three-body decays. Finally, a highly reliable particle identification system was required to insure that we were in fact measuring the decay rates of interest.

Kaons were provided by a carefully constructed beamline. The kaon decay products were detected, and their tracks measured by a two-arm, two-magnet spectrometer. Tracking information was provided by 10 precision drift chambers. Uncertainties in track reconstruction arose from four primary sources. The first was the intrinsic spatial resolution of the chambers. The second was the measurement error of the drift chamber positions. Next were errors in the magnetic field map. This had been obtained *via* Hall probes, prior to running, in a 2 inch cubed grid covering both magnets and their fringe fields. Finally, there were uncertainties resulting from multiple scattering within the magnets, which were minimized by filling the magnets and the space between the drift chambers with helium.

In addition to tracking information, it was also necessary to determine the time of arrival of particles within the apparatus, and whether they were consistent with a kaon decay upstream. This lower level trigger information was provided by the upstream drift chamber modules and by two banks of scintillator counters farther downstream.

The particle identification components of the apparatus were placed downstream of the magnetic spectrometer. These detectors were designed to identify decay products of primary interest—electrons and muons. To reduce backgrounds caused by particle misidentification, there were two systems of identification for both particle types. In addition, one each of these systems provided the higher level trigger for muons and electrons.

Electron identification was performed by Čerenkov counters and lead glass calorimetry. The Čerenkov counter provided detailed information for offline analysis, and a fast response for the electron trigger. The lead glass array discriminated particle types by the amount and distribution of energy deposited within it.

Muon identification was performed by a scintillator hodoscope and a rangefinder. Both were located behind 91 cm of iron, referred to as the muon filter since most electrons and hadrons cannot penetrate it. The hodoscope provided time information for offline analysis and a fast signal for the muon trigger. The rangefinder measured muon momentum for comparison with the spectrometer momentum determination.

In the sections which follow, references will be made to the E791 coordinate system. In that system, the origin is defined as the focal point of the beam collimator system. The z -axis lies along the neutral beam, which runs down the center of the experiment, with positive z running in the direction of travel for particles within the beam, that is downstream. The x -axis is parallel to the ground, with positive x defined to be to the left of the beam center, looking downstream. The y -axis is perpendicular to the ground, with positive y defined to be above the beam center.

3.2 BNL B-5 Beamline

This experiment was performed at the Brookhaven National Laboratory Alternating Gradient Synchrotron (AGS) facility, B-5 beamline (see Figure 8). The AGS provided a 24 GeV/ c proton beam with a 3.2 second cycle time (later reduce to 2.8 seconds) and an effective spill length of 1.4 seconds (later reduced to 1.0 seconds and then increased to 1.2 seconds). The protons were directed onto a 0.318 cm by 0.318 cm by 20.3 cm copper target. The target was mounted such that the production angle—the incident angle of the proton beam—could be varied between 0 and 4.5°. As the production angle is increased, both the neutron and kaon fluxes drop off. However, the neutron flux falls off more rapidly. Tests prior to the beginning of the data taking showed that a production angle of 2.75° gave

the maximum ratio of K_L to neutrons. The target was also adjustable in z relative to the focal point of the beam collimators (see below). Proper positioning of the target reduced background caused by particles striking the face of the collimators, but at the cost of reduced acceptance. Tests prior to the run obtained the greatest acceptance with acceptable background levels at -11.9 cm in z relative to the focal point.

Downstream of the target two sweeping magnets guided charged particles into a beam dump beneath the B-5 line. A series of lead foils within the first magnet converted high energy photons into positron-electron pairs which were then swept out of the beam. Also, starting within the first magnet, there were placed a series of four collimators, which limited the neutral beam to a solid angle of 4 mrad by 15 mrad in x and y , relative to the target. Beginning with the second collimator, the neutral beam traveled in vacuum.

Downstream of the collimators, the beam entered an 8.0 m vacuum box, maintained at ~ 15 Torr. All events detected downstream were required to decay within this region. The downstream end of the decay box contained three Mylar windows, a central window for the neutral beam, and one window to either side for the left and right side decay products. The entire assembly, from the sweeping magnets to the end of the decay region, was surrounded by iron and lead plates, to eliminate charged particles and neutral hadrons, and encased in blocks of hydrogen-rich concrete and cans of Borax, to moderate and capture neutrons. This reduced the level of background.

3.3 E791 Spectrometer

Downstream of the vacuum decay region was the actual detector apparatus (see Figure 9). Since the primary interest of E791 has been two-body K_L decays, the experiment was laid out in two identical arms located symmetrically opposite each other relative to the central neutral beam. To reduce background from the neutral beam, the beam region was filled with helium, from the end of the decay volume to the end of the Čerenkov counters.

The two-magnet spectrometer and high resolution drift chambers served to determine the momentum of decay products. A two-magnet system allowed one to measure the momentum of a particle twice. This served to reduce momentum uncertainties, and to reduce muon background from π decays within the spectrometer. Such decays would have different momenta measured by the first and second magnets. The magnet dimensions were 1.22 m by 0.94 m by 1.22 m and 2.44 m by 1.12 m by 1.02 m in x , y and z for the upstream and

downstream magnets respectively, covering both arms of the spectrometer. Each magnet had a field strength of 0.7 Tesla, giving each charged particle an equal but opposite impulse of $300 \text{ MeV}/c$ in transverse momentum. This restored a particle track to a path parallel to its original direction following the second magnet, simplifying both triggering and pattern recognition. Mounted in the center of each magnet was a Hall probe, which monitored the field strength continuously during the run.

3.4 Drift Chambers

Accurate tracking information was, perhaps, the most critical detail in this experiment. From precise tracking, it is possible to determine the momentum of an event's particles, and hence calculate the invariant mass and collinearity of the event. Collinearity is defined as the angle between the parent kaon momentum vector, and the reconstructed total momentum vector of the daughter particles. "Missing" mass, implied by a large collinearity angle, would indicate the presence of undetected neutral daughters. An incorrectly reconstructed kaon mass can also result from particle misidentification. These details can distinguish true dileptonic events from the multitude of three-body semileptonic events occurring within the detector. At the same time, however, care must be taken not to destroy the position resolution by introducing relatively massive detectors in the particles' paths. Drift chambers offer an excellent mechanism to satisfy both of these criteria.

E791 used a series of five drift chamber modules (referred to as DC#) in each arm of the spectrometer. Each module had both an x and a y measuring component. Figure 10 is a layout of the wire structure of each component. Positional information was determined via $0.001''$ gold plated tungsten sense wires, which were connected capacitively to a preamplifier card mounted on the drift chamber frame. Surrounding the grounded sense wires were the field wires, which maintained and shaped the electric field. These $0.0043''$ copper-beryllium wires were held between -2400 and -2500 volts. Guard wires also were added assistance in shaping the electric field. The entire module was encased in a grounded aluminized Mylar skin $0.005''$ thick. This served both to electromagnetically shield the wires and to contain the gas mixture. A mix of 49% argon and 49% ethane with 2% ethanol vapor was used.

As can be seen in Figure 10, two planes of sense wires were used in each component to measure position. Using only one plane of wires leads to positional inaccuracies due to the left-right ambiguity concerning which side of the wire the particle passed. Rather

than increasing the number of wires to decrease this inaccuracy, two staggered planes were used, solving the left-right ambiguity while keeping the number of wires to a minimum (NB. as discussed in Section 5.3, this does not solve all left-right ambiguities). This two plane system gave a spatial resolution of $120 \mu\text{m}$ rms.

3.5 Trigger Scintillator Counters

While tracking information is crucial to a successful experiment, one must also know when to look for a track. A fast electronic trigger (see Section 4.2) was used to determine when a potentially interesting event was occurring within the spectrometer. The key elements of this trigger were two banks of scintillator counters, one located immediately downstream of DC5, the other located just downstream of the Čerenkov counters (see Figure 11). These banks were referred to as the trigger scintillator counters (TSCs). The TSCs had a secondary use in helping to decipher ambiguities in data from DC4 and DC5 during pattern recognition.

Each bank contained 64 x and 64 y measuring slats of doped polystyrene scintillant produced by Kyowa Glass Corporation. Some of the outermost slats were not read out. This caused no problems in the experiment, as the TSCs were not a limiting aperture. The x measuring slats were 1.80 m by 0.02014 m, the y slats were 1.28 m by 0.02814 m. The slats in the downstream bank were 1.0 cm thick in z , while those in the upstream bank were 0.5 cm thick, to reduce the amount of material in the particle path upstream. Each y slat was connected to a single 1" Hamamatsu R1398 photomultiplier tube. The x slats were connected to tubes at both ends, with two slats connected to each tube at both ends, and the top tubes staggered by one slat relative to the bottom tubes. This reduced the number of photomultiplier tubes and the number of channels for readout.

The signals from the tubes were sent over RG8 cable to the counting house. There, the signals were split, with all signals going into the fast TDCs. The x signals were also sent to meantimers before passing on to the Level 0 trigger. The y signals from each bank were logically OR'd and then passed on to Level 0.

3.6 Čerenkov Counters

The first of the particle identification systems was the Čerenkov counters (CER). Its purpose was to provide both a fast online electron identification (ID) for use in the Level 1 trigger,

and detailed information for offline analysis. To accomplish this, a high electron ID efficiency coupled with a low muon and pion efficiency was required. In addition, the mass of material in the particle path was kept low to minimize knock-out electrons and photon conversion.

Čerenkov counters generate a signal based on the collection of photons generated by particles moving faster than the group velocity of light within the counter medium. By the proper choice of the index of refraction n for the medium, one can maximize the velocity discrimination between electrons and the more massive muons and pions. In this case, a 60%–40% mixture of nitrogen and helium was used, with an index of refraction of 1.00014. With this mixture, all electrons with a momentum within the region of interest produced Čerenkov light, but only pions with a momentum greater than 8.34 GeV/ c and muons with greater than 6.31 GeV/ c produced a signal. The gas was frequently sampled using interferometry to maintain the proper n .

The Čerenkov counters consisted of 3 m by 1.4 m by 1.7 m aluminum boxes (see Figure 12). The four sides of each box, along with their external supports, were located outside the region through which particles of interest passed. The ends of each box were covered with 1/32" aluminum windows, to minimize the material within particle trajectories. Inside the downstream end of each box was a 4 × 2 array, in x and y , of spherical mirrors. Each mirror focused the Čerenkov light onto one of eight 5" RCA 8854 Quantacon phototubes. The tube faces were coated with a thin film of p-terphenyl waveshifter to increase sensitivity to shorter wavelengths. To protect the tubes from helium, dry nitrogen was fed through the housing of each tube. The tubes were also shielded from the fringe fields of the magnets.

The phototube signals were passed on to the counting house *via* RG8 coaxial cable. The signals were then split, with part going to the ADCs. The remainder was discriminated and then split again between the TDCs and the Level 1 trigger.

For most of the data collection period, the efficiency of the CER for electron ID, as determined by semileptonic studies, was 94.9% [29]. However, one CER counter was accidentally moved at some unknown time. This was not discovered and corrected until an inspection during a maintenance period. This resulted in 705 runs for which the overall electron efficiency dropped to 87.6% owing to the misalignment of the optics. The weighted efficiency for the entire running period was 93.8%. The efficiencies for detecting pions and muons below their momentum thresholds for Čerenkov light were 1.5% and 1.9% respectively. The CER was designed to detect electrons for the decay mode $K_L \rightarrow \mu^\pm e^\mp$ but it also proved useful for electron particle samples for various studies related to the $K_L \rightarrow \mu\bar{\mu}$

analysis.

3.7 Lead Glass Array

The next particle ID counter was the lead glass array (PBG). As with the CER, its primary purpose was to distinguish electrons from muons and pions. This was accomplished by measuring the total energy lost by particles as they passed through the array. Most electrons would electromagnetically shower within the array, depositing all their energy there. Muons, however, would lose only a fraction of their energy to Čerenkov radiation. Pions would either lose energy to Čerenkov radiation or produce a hadronic shower, which produces a different energy distribution from an electromagnetic shower.

The PBG was divided into three components (see Figure 13). The first consisted of 52 lead glass blocks, 0.109 m by 0.9 m by 0.10 m. The blocks were arranged in a 2×13 array in x and y , in each arm of the detector. These upstream arrays represented 3.3 radiation lengths, and were referred to as the converter blocks, since they convert most electrons into electromagnetic showers. Due to the high flux of particles near the neutral beam, fast Amperex 3462 phototubes were attached to those blocks nearest the beam. Slower EMI 9531R tubes were used in the outer blocks where the flux was lower.

Immediately downstream of the converter blocks was a 36×27 array in x and y of scintillator counters, 1.5 cm deep, 5.1 cm wide, and 1.861 m long in x or 1.394 m long in y . These served to give a fast signal to the Level 1 trigger when a shower was occurring within the PBG. This trigger was used in the 1988 run to analysis $K_L \rightarrow \pi^0 l^+ l^-$ events. These triggers were disabled in 1989, and information from these counters was not used.

The second array of lead glass consisted of 216 blocks, 15.3 cm square by 32.2 cm deep. These back blocks were arranged in a 9×12 array in each arm. The back blocks represented 10.5 radiation lengths. As with the converter blocks, the back blocks nearest the beam were connected to fast EMI 9618R, and those farther away were connected to either Amperex 58AVP or 58DVP tubes.

The entire PBG assembly was enclosed in a wooden, light-tight hut. Signals for the tubes were passed to a patch panel on the hut *via* RG58 cable and then *via* RG8 cable to the counting house.

3.8 Muon Hodoscope

Following the lead glass was a 0.91 m wall of iron corresponding to 8.7 nuclear interaction lengths. Most electrons and hadrons interacted within the iron, allowing only muons to penetrate downstream. Immediately behind the muon filter was the muon hodoscope—a bank of scintillator counters. Its purpose was twofold, to provide a fast signal to the Level 1 trigger for online muon ID, and to provide detailed offline timing information.

The muon hodoscope (MHO) consisted of 11 x and 14 y slats of Bicron BC408 plastic scintillators (see Figure 14). Both the x and y slats were 2.54 cm thick and 18.8 cm wide. The x slats were 2.69 m long, while the y slats were 2.29 m long. AMPEREX XP2230 2" phototubes were attached to each end of the x slats and to the outer end of the y slats. In both cases, the ends of the slats were tapered down to 5.3 cm by 2.54 cm and optically coupled directly to the phototubes. The phototube signals were passed to the counting house *via* RG8 cable, where they were discriminated. The y signals were split, with part going to the TDCs, the remainder being OR'd together and sent to the Level 1 trigger. The x signals were also split, with part going to the TDCs, the remainder being meantimed for each channel and then OR'd and sent to Level 1.

During the course of the run, the muon ID efficiency for the MHO was measured to be 97.5% [30]. The "false" ID efficiency for pions was 8.7% and for electrons 0.4%.

3.9 Muon Rangefinder

The final particle detector was the muon rangefinder (MRG). The MRG used a series of proportional tube counters, interspersed within degrading material. The depth of penetration was used to determine particle momentum, based on the assumption that the particle was a muon. This MRG momentum could then be compared offline to the spectrometer momentum. Electrons and pions showed a momentum mis-match, since neither will penetrate the MRG as deeply as a muon of the same momentum.

The MRG consisted of 13 modules per arm of proportional tube counters, each module containing separate x and y planes (see Figure 15). The x -measuring planes were built from 12 aluminum extrusions 3.01 m long. The y -measuring planes were built from 16 extrusions 2.25 m long. Both extrusions types were 19 cm wide by 1.42 cm deep, and contained eight cells. Two gold plated tungsten wires ran down each cell, and were maintained at +2650 volts. A gas mixture of 49% argon, 49% ethane and 2% ethanol vapor flowed through the

cells. While designed for individual readout, in actual use the eight cells of each extrusion were discriminated, then OR'd together and sent to the counting house *via* Ansely cable.

The bulk of the MRG was in the degrader material. Each arm contained 75 marble slabs 3" thick spaced 2" apart. Twenty-five aluminum slabs were used in the final quarter of the MRG. This design gave a muon momentum range from 1.5 GeV/c (necessary to penetrate muon filter) to 5.5 GeV/c (necessary to exit back of MRG). By selecting irregular spacing of MRG modules within the degrader, a 10% momentum resolution was obtained.

For 1989, the MRG muon ID efficiency was measured to be 99.2% for semileptonic events. For a more detailed discussion of the design, construction and performance of the MRG, see Appendix A.

Chapter 4

Data Acquisition

4.1 Overview

Such is the perverse nature of HEP experiments that the primary problem is often one of too high a data rate rather than too little. The large number of channels in the E791 detector—more than 6000—combined with individual channel rates in the megahertz range, can easily exceed the recording ability of any mass data storage device. The excessive rates can also lead to deadtime problems due to the time required to digitize and record an event.

To overcome this liability, E791 used a two-prong attack. First, a 4-stage event trigger reduced the number of events to a manageable level. Each stage took progressively more time, and used more information to select events of interest. The first stage merely required the presence of at least one charged particle in each arm of the spectrometer. The second stage required that the identification of such particles be consistent with a K_L decay mode. The third stage, which was tested but not used, and the fourth stage examined the kinematics of an event to see if it was consistent with the decay mode as determined by the second stage. Each stage examined only those events which passed the previous stage, and only events passing the final stage were written to tape. As an exception, a percentage of the first stage events was passed unconditionally for later study, and to provide for normalization.

The second approach was to use a custom designed digitization and readout system. The readout system incorporated four features to reduce the processing time for each event. First, times and pulse heights for each event were quickly digitized using custom modules. Second, a two layer event buffer with a fast transfer rate allowed an event to be stored while digitization proceeded on a previous event. Third, a sparse data scan which read

out only channels with hit information, reduced data transfer time. And finally, a highly parallel readout architecture permitted the analysis of several simultaneous events in the higher level trigger.

In the following sections, the trigger and readout architecture are described in more detail.

4.2 Level 0 and Level 1 Triggers

The initial stage of the trigger was Level 0 (L0). The purpose of L0 was to indicate the presence of at least one charged particle in each arm of the spectrometer. It used fast electronics to decipher signals from the TSCs. A schematic layout of L0 is in Figure 16.

Signals from the TSCs were discriminated using LeCROY LRS4416 modules. The x signals were then sent to a meantimer. For purposes of the L0 trigger, the TSCs were divided into four banks. Banks 1 and 2 consisted of the OR'd output from the x meantimers on the upstream TSC x modules on each beam side. The upstream y modules were not used in L0. Banks 3 and 4 used the downstream x and y modules in the following fashion. The meantimed signals from the x modules were again OR'd together, in groups of 16 adjacent counters. The signals for the y modules were OR'd together as one unit. The y output and the 4 x outputs were then OR'd to form bank 3 and bank 4. The 4 bank signals were then passed to a LeCROY 4508 programmable logic unit (PLU). A L0 trigger was defined as an in-time hit (resolution ~ 7 ns) in all four banks, which sets the L0 strobe.

The L0 strobe enabled another PLU which formed the second stage of the trigger—Level 1 (L1). Level 1 does a fast, rough particle ID on each side of the beam, and classifies the event as to possible K_L decay modes. The CER and MHO provide the electron and muon particles IDs respectively. A schematic layout of L1 is in Figure 17.

Level 1 required that, for each arm, at least three of the first four drift chamber planes (x and y) have at least one hit in time with L0, and that at least one of the two planes in DC3 has a hit. This was defined as the L1 minimum bias trigger (L1 MB).

Next, L1 does a fast particle ID. The eight discriminated outputs of the CER were OR'd to form the electron ID for each side. The x signals from the MHO were meantimed, then the x and y signals were OR'd together to form the muon ID. Level 1 then set bits in a trigger word based on the results of the particle ID, and sent the trigger word on to the Readout Supervisor. A L1 pulse started the TDCs and sent a gate on to the ADCs and

strobed the latch modules. There were six non-exclusive ID bits. The first and second bits were the μe and $e\mu$ bits formed by a L1 MB plus a left CER and a right MHO or a L1 MB plus a right CER and a left MHO. The third bit was the $\mu\mu$ trigger, and consisted of a L1 MB plus a left and right MHO. The fourth bit was the ee trigger, and consisted of a L1 MB and a left and a right CER. All μe , $e\mu$, ee and $\mu\mu$ events were passed on to L3. The fifth bit was the minimum bias trigger described above. Minimum bias events were prescaled by 2000 and passed to L3. The sixth bit consisted of a L1 MB plus a veto on the CER and MHO for both arms of the detector; this was the L1 $\pi\pi$ trigger, which was used in resolution studies. The seventh bit was the L1 $\pi\pi$ bit prescaled by 500. Two higher bit triggers were defined for three-body events, but these triggers were not used in the 1989 analysis. Several calibration and pedestal triggers bits were also defined.

4.3 Level 2 Trigger

Level 2 (L2) was a hardware trigger which used the TSC information and a memory lookup table to cut events based on the correlation between the upstream and downstream TSC hits [31]. If one plots the upstream x slat hit versus the downstream x slat hit, and the same for the y slat hits, one finds that for good tracks from physics events, the points fall within a narrow band. If the hits are not correlated, the points tend to be uniformly distributed throughout the plot. Level 2 used Monte Carlo events to produce look up tables based on this correlation. These tables were then stored in hardware, accessed by the TSC hits. In addition, L2 could use the TSC hits to make a rough calculation of, and loose cut on, the invariant mass and collinearity of an event. Tests of L2 showed a significant improvement in trigger rates for higher intensities. However, other limitations prevented E791 from running at rates sufficiently high to warrant its use.

4.4 Level 3 Trigger

Level 3 (L3) applied a fast three stage tracking algorithm to all events which pass L1, using the 3081E cluster (see Section 4.6). It utilized hit information from the first three drift chambers in each arm and a simplified field map for the magnets to determine the event kinematics and to perform loose cuts on those kinematics. Note that while L3 was calculated for all L1 events, prescaled L1 MB events were passed by L3 regardless of the L3

decision.

Stage 1 of the L3 trigger examined the first three x and the first two y DC planes in each arm, looking for good hits which may be associated with a particle track. Level 3 searched for pairs of adjacent wires with good time-summed hits. A maximum of four such hits was allowed in each plane. If L3 could not find a good time-summed pair in a plane, it accepted one bad time-sum for the plane. If one of the ten planes contained no good or bad time-sum pairs (i.e. less than two hit wires in the plane), then L3 rejected the event.

Stage 2 of L3 then determined whether or not the hits found by stage 1 formed a possible track in each arm, and if the possible tracks from each arm could be related. First, stage 2 compared the positions of the hits in the first two planes in descending order of time-sum, looking for correlated hits via a look up table formed from actual data. The x and y views were examined separately at this point.

The x tracks formed by correlated hits were then compared to insure that they were divergent. The y tracks were projected to DC5 to insure that the tracks passed through it. Next, an x and a y decay vertex were formed by projecting the x and y tracks from each arm upstream into the decay region. The two vertices were required to fall within 5 cm of each other in z . Finally, the x tracks were projected in a straight line to the center of the first magnet, where a 300 MeV/ c transverse momentum kick was applied (a simple approximation to the first magnet's effect on a charged particle), and then projected in a straight line to DC3. The region immediately around this projected hit in the third drift chamber was then examined for a good time-sum hit.

Stage 3 of L3 then performed the rough kinematic calculation for the event. A simple track was formed in x by again projecting a straight line from the first two chamber hits to the center of the first magnet, and then forming a straight line with the hit in DC3. The transverse momentum kick was calculated by integrating the magnetic field, taken from a reduced map of the y B-field component, over this track. By comparing the track deflection to the momentum kick, stage 3 obtained the track momentum. The track momenta for each were then summed and the collinearity angle was determined. A large collinearity angle indicated missing momentum, such as might be carried off by an undetected neutral particle in a three body decay. Initially, L3 cut collinearity angles greater than 20 mrad, but roughly a third of the way through the run, this was decreased to a 10 mrad cut.

Finally, stage 3 calculated the invariant mass of the event, based on the event classification provided by L1. The invariant mass was required to fall within the range 0.460 GeV/ c^2

to $0.5300 \text{ GeV}/c^2$.

4.5 Readout Electronics

4.5.1 Time-to-Digital Converters

Various detectors in the experiment required that timing information be recorded for the hits registered. To measure these times, two types of custom designed time-to-digital converters (TDCs) were employed, each with specifications dictated by the detectors to be read out.

For the drift chambers, the drift velocity of $50 \mu\text{m}/\text{ns}$ necessitated a dynamic range of at least 100 ns, and the drift chamber resolution of $120 \mu\text{m}$ required a rms time resolution of less than 1 ns. In addition, the large number of channels further required a low per channel cost with good reliability. To satisfy these requirements, the UCLA group designed and built a 32-channel 6-bit TDC with a 2.5 ns least count, a dynamic range of 160 ns and an average rms time resolution of 0.76 ns [32].

The Level 1 trigger provided a start for a 100 MHz clock, which was split into two signals, one delayed by $1/4$ cycle. By using the leading and falling edges of both signals, the TDC obtained the necessary 400 MHz clock frequency for a least count of 2.5 ns, without actually using such a high frequency signal. To cover the entire 160 ns range in 2.5 ns increments, the TDC used a 6-bit *gray code* with one bit changing with each edge of the clock. The gray code was generated using ECL 100K integrated circuits. Once the event was digitized, the TDC transferred information to a stage 1 latch and sets a flip-flop to indicate which channels contained hits. To decrease data transfer deadtime, there is a stage 2 latch and flip-flop immediately following the stage 1 latch, allowing the TDC to digitize one event while waiting for a second event to be read out.

The CER, MHO and x TSCs had much more stringent timing requirements than the drift chambers, over a smaller time range. To satisfy them, the Stanford group designed an 8-bit fine binned TDC (FTDC) with a least count of 210 ps and a dynamic range of 55 ns [33]. As with the UCLA TDCs, L1 provided a start signal to the FTDC, which began charging a capacitor. A hit stopped the charging, and the FTDC recorded the resultant voltage of the capacitor.

Late and early hits caused some problems for both types of TDCs, albeit in different ways. For the UCLA TDCs, an early hit which was still present at the L1 starts would result in a zero time hit, while a clock overflow would result in no hit being recorded for

a late hit. For the Stanford FTDCs, an early hit present at the L1 start and overlapping a later hit would result in no hit being recorded, while a late hit would have the highest count possible.

4.5.2 Amplitude-to-Digital Converters

Signals from the CER and PBG photomultiplier tubes were digitized using amplitude-to-digital converters (ADC). The ADCs required a dynamic range of 100 pC, but also required fine resolution for small pulses. To accomplish this, Stanford designed an 8-bit bilinear ADC [34]. For small signals (0–63 channels), the sensitivity of the ADC was 150 fC/count, while for larger signals (64–255 channels) the sensitivity was 470 fC/count, giving the full 100 pC range. Level 1 provided the start for a 20 to 150 ns gate. As with the TDCs, a two stage buffer allowed the ADC to hold 2 events, and flip-flops at each stage indicated which channels contained hits for the sparse data readout.

4.5.3 Latch Modules

Signals for the MRG, as well as trigger information for the Readout Supervisor, were digitized by a 96-channel latch module, designed at LANL. In the case of the MRG, a Level 1 signal opened a 160 ns gate during which all hits in the MRG were recorded in stage 1 flip-flops. As with the other readout modules, each latch had a second stage. However, unlike the TDCs and ADCs, every channel of the latches were read out; there was no sparse data readout. For the trigger latches, trigger bits were recorded without a latching clock.

4.6 Readout Architecture

A parallel readout system was used to increase data transfer rates [35]. The readout architecture had the following layout, starting from the detectors. First were the front end crates which contained the digitization modules described previously. The control of crate readout was handled by the Readout Supervisor. Data was passed to a cluster of 3081Es, which performed the L3 decision for events. Finally, a host computer transferred the data to storage, monitored the readout system, and allowed the user to interact with the experiment. A schematic layout of the readout system is in Figure 18.

The front end crates were custom built units similar to FASTBUS crates. Each crate contained 16 *data modules*—the ADCs, TDCs, and latch modules—and one *crate scanner*,

plus a spare station. The data modules were capable of digitizing an event in under 200 ns. A two stage buffer allowed them to digitize one event while a second awaited readout. The crate scanner served a dual purpose. It collected and controlled the flow of data from the data modules to the 3081Es. The scanner also served as a fanout module, allowing each crate to be connected to each 3081E. To minimize the number of memory ports required by the 3081Es, it was possible to read out two crates *via* a single crate scanner. The crate scanner for the second, or *slave*, crate was connected to the scanner for the first, or *master*, crate. The slave crate signaled the master crate when it had data requiring transfer. The master crate then passed on the data from both crates to the 3081Es. The E791 system consisted of 21 front end crates (12 masters) with a maximum transfer rate of 0.64 Gbytes/s and an average readout time of 10 μ s.

Data from the front end was transferred to the 3081Es for the L3 decision. The 3081Es were modified versions of the standard SLAC 3081E design [36]. Our 3081Es used a standard processor board and three turbo memory boards, with a custom designed interface. The *turbo* memory boards were standard memory boards with 11 Mbytes of static memory, but with the addition of four external ports, each connected to one master crate *via* a 17-pair ECL cable. Data was read into memory, under control of the readout Supervisor, from all crates, during which period, the processor was offline. After transfer was complete, the Readout Supervisor started the 3081E processor, which executed the L3 algorithm. Should an event pass L3, the 3081E signaled the host computer and transferred the event through the processor interface *via* a DR11W interface to the host computer.

Data transfer was under the immediate control of the Readout Supervisor [35]. The Supervisor's purpose was to keep the stage 1 buffer of the front end electronics clear, since the experiment was dead while an event was in stage 1. This was accomplished by transferring an event from stage 2 to a 3081E as soon as one was available, then shifting a stage 1 event to stage 2 and clearing stage 1. The Readout Supervisor was designed with a third feature, which aborted and cleared an event in stage 1 or stage 2 if the event failed the L2 trigger. However, since the L2 trigger was not implemented, a pass L2 signal was always present, negating this feature. The Supervisor was also responsible for starting each 3081E once its memory was full.

The Readout Supervisor was constructed from 12 CAMAC modules, each of which was responsible for keeping track of the state of a portion of the system. Signals from various elements of the readout system, such as L1, available 3081Es etc., were combined with the

event type	fraction	total
μe	20.74%	49,111,200
$e\mu$	22.17%	52,510,900
$\mu\mu$	41.89%	99,198,800
ee	13.72%	32,481,100
min bias	23.23%	55,010,200
$\pi\pi$	9.88%	23,397,800
$\pi\pi$ prescale	2.83%	6,700,900

Table 2: Physics events classified by L1 trigger.

current state of the system to form a 14-bit address within the Readout Supervisor *state matrix*. The state matrix was a 16K address, 16 data bit static RAM, which contained the 16384 possible states for the readout system. The RAM data word at a given address gave the new state for the system, as well as the proper action to be taken by the Supervisor for the current state.

Overall control of the readout system was provided by the host computer, a DEC μ VAX II. The VAX stored events from the 3081Es, and wrote the data to a storage buffer. Periodically, the buffer was emptied to one of two 6250 BPI magnetic tape drives. Once the data from a 3081E was read out, the VAX informed the Readout Supervisor that the 3081E was available for a new event. Communication between the VAX and the Readout Supervisor was conducted via the CAMAC dataway. The VAX also provided all user interaction with the readout system. The acquisition system compiled various histograms, monitoring the functioning of the readout system and the individual detectors. Diagnostic tests for the system were also run from the VAX.

4.7 Acquisition Rates

In 1989, E791 began physics data collection on January 29, and finished collection on May 27. A total of 2939 physics tapes were written during that period, with an average of 90000 events per tape. Of these events, 89% were physics events, the remainder were calibration and pedestal events. Table 2 gives the fraction of events for each of the physics triggers.

The average beam intensity on the B5 target was 3.8 Tp per spill. This resulted in drift chamber rates in the range of 1.5×10^7 to 2.0×10^7 per spill, with the higher rates in the upstream chambers. Level 0 reduced the data rates to 1.2×10^6 per spill. The rate dropped to 7.4×10^3 per spill in L1. Finally, L3 produced 1.4×10^2 raw events per spill, which were

written to tape [37,38].

The decision to run at 3.8 Tp/spill, which was lower than the rate anticipated in the original proposal, was imposed by four conditions. First, the drift chambers were on the verge of continuous firing. Second, the 3081Es were running at maximum level, resulting in deadtime due to the overload. Third, the pattern recognition efficiency, monitored offline, was inversely proportional to the spill rate. Finally, the AGS was not able to deliver a substantially higher proton flux to B5, due to the requirements of other users.

Point three could probably have been overcome with a better pattern recognition algorithm. Indeed, as shall be detailed in Section 5.2.1, the 1989 version of pattern recognition had a significantly improved efficiency over the 1988 version. Point two could have been overcome at higher rates by activating Level 2. However, point one proved to be the main limiting factor. Even if the AGS had been able to provide higher rates, the drift chambers could not have handled it, and E791 was rate limited.

Chapter 5

Data Reduction

5.1 Overview

During the four months of running in 1989, 2939 physics data tapes were written. Four tapes had internal inconsistencies which precluded their use in the subsequent analysis. This left 2935 tapes with a total of 236,802,103 physics events to be analyzed. E791 used a three stage process to reduce the number of events to a manageable size. The process involved first finding the decay product tracks inferred by the online triggers. Next, an accurate fit was performed on those events for which tracks were found. Finally, events were sorted according to the kaon decay mode, based on offline particle identification of the tracks.

5.2 Track Finding

The first offline stage in cutting the raw data was pattern recognition. Online, L0 through L3 checked for the possibility of tracks which may have been from a kaon decay, and passed likely events to tape. Pattern recognition then attempted to find those tracks and to reconstruct a kaon decay vertex from them. The application of pattern recognition to the physics data tapes was referred to as PASS1.

5.2.1 Pattern Recognition

In previous data runs, pattern recognition utilized only information from the drift chambers. Good hits in DC1 and DC2 were checked for upstream track candidates and projected into the center of the first magnet. DC4 and DC5 were then checked for downstream

track candidates and projected upstream to the center of the second magnet. A given pair of upstream and downstream track candidates was then connected by a straight line running through DC3, which was then checked for a good hit within a narrow window around the potential track. The x and y views were initially treated separately but were later combined into 3-dimensional tracks. Beam left and beam right 3-D tracks were then projected upstream into the decay volume to determine the decay vertex.

The major flaw with this algorithm was that track candidates quickly multiplied with each additional drift chamber hit. Eventually, the number of track candidates could exceed the program's array storage, causing an event to fail. A brute force method of solving this problem would be simply to increase the array sizes. However, tests showed that even with a tenfold increase in array size, pattern recognition only reconstructed 5% more good events, while it increased CPU time by 300% [38]. Instead, a new track finding algorithm was created, inspired by the L2 algorithm, which utilized additional information from the TSCs.

The new pattern recognition started from the same base as the old—finding good hits in the drift chambers. Pattern recognition first examined each chamber, checking for three adjacent hit wires with a good drift time-sum. The routine next searched for adjacent pairs of wires not already associated with a three hit group, again with a good time-sum. If the routine could not find either of the above in a given drift chamber plane, it created two adjacent hit pairs from a single hit wire. If any of the 20 x or y planes contained no hits, the event failed pattern recognition. Also, if fewer than three planes contained a good pair or triple, the event was rejected.

Next, pattern recognition examined the TSCs. The algorithm required a good hit time in two phototubes from an x counter, with a good meantime. A y counter required a good hit time from the phototube. Owing to the design of the Stanford TDCs, it was possible for x counters to register no hit if an accidental signal existed prior to the TDC start and overlapped a good hit. For the y counters, which used the UCLA TDCs, such an event would register a zero time. In either case, an event could be lost with either no x hit or a bad y time. To avoid this, pattern recognition also examined the latch signals for the x and y counters. These signals, which bypassed the TDCs, had excellent timing information because of their use in the L2 trigger. Pattern recognition would take timing information from the latches in the case of a missing or zero time event. Only if neither the TDCs nor the latches indicated a good hit would pattern recognition fail the event.

Having found the TSC and DC hits, pattern recognition attempted to reconstruct 2-dimensional particle tracks, treating x and y , and beam left and beam right separately. Studies for the L2 trigger showed that for kaon decay products, a plot of the upstream counter hit versus the downstream counter hit fell within a narrow band. Thus, given a downstream hit, one could assign a narrow window in the upstream TSC within which to search for a good time upstream hit.

For the x -view, the two TSC hits formed a track which was then projected upstream into DC5. Again, the routine searched for a good time hit within a narrow window. The resultant track was then projected into DC4, and the process was repeated. At this point, the algorithm was ready to project through the downstream magnet to DC3. However, pattern recognition had no momentum information for the particle. Therefore, it projected a straight line back to DC3 (i.e. no deflection due to the magnetic field), and searched a very wide window (within 68 cm but not within 0.3 cm) for a good hit. The 68 cm window limited the acceptable track deflections, imposing an implied 0.6 GeV/ c minimum momentum cut. The original track from the downstream TSC to DC4 was then projected to the center of the second magnet. This point, combined with the DC3 hit, formed a line which was projected to the center of the first magnet. Since the E791 magnets imparted equal but opposite transverse momentum impulses, the original opening angle was preserved. Thus, the slope of the downstream track after the second magnet could be used to form a projection from the center of the upstream magnet to DC2. Pattern recognition then repeated the process used in DC4 and DC5 to find track related hits in DC1 and DC2. The process was then repeated in the y -view, with the simplification that except for the fringe areas of the magnets, the particles would not be deflected as they passed through the magnetic fields. It should be noted that pattern recognition did take into account this focusing effect in the critical magnet regions.

The advantage of this process was that multiple 2-D track candidates in a particular view and arm would appear only if more than one good time hit fell within the windows searched or from multiple hits in the TSCs, avoiding overflows in the track candidate storage areas. No events were lost due to too many x or y 2-D track candidates for the new pattern recognition, as opposed to 4.4% losses under old pattern recognition.

Once a 2-dimensional track had been found, pattern recognition resolved some of the left/right ambiguities in the track hits. Ambiguities arose from the fact that for a single hit wire, the track may have passed on either side of the wire. For two and three adjacent

hit wires, the track may have passed on either side of the wire with the smallest distance of closest approach (DOCA). Single wire left/right ambiguities could not be resolved at this point, and had to wait for the 3-D track. For two and three wire hits, pattern recognition calculated the track slope at the ambiguous chamber using both possibilities, then compared the slopes to other chambers, choosing the best match.

The algorithm next constructed two χ^2 for each 2-D track. The first was based on the time-sums of the track hits. The second was the χ^2 for a straight line fit for DC1, DC2, DC4 and DC5 combined with the DC3 position match. For the x -view track, a track momentum was determined from the magnet bends (upstream and downstream), and the χ^2 had an additional term for the front/back momentum match. The x and y tracks were then combined to form a 3-D track, and the χ^2 were recalculated for each track.

Pattern recognition compared all combinations of beam left and right tracks to form a decay vertex. The tracks were projected upstream into the decay region, and the tracks with the smallest DOCA were chosen to form a vertex. The vertex was chosen to be the midpoint of the line segment connecting the two tracks at the point of the DOCA. Using the vertex, and the track momenta, pattern recognition determined the collinearity of the event, and using the L1 particle IDs for each side, the invariant mass of the event.

Finally, pattern recognition resolved the left/right ambiguities for single wire hits. The algorithm took both possible track solutions and calculated the χ^2 , and then chose the best χ^2 as the final track. The routine then recalculated the vertex, mass and collinearity if necessary.

5.2.2 PASS 1

The initial data reduction was performed by the PASS1 code. The code cut events based on the results of pattern recognition, and on three crucial quantities. The first two quantities were collinearity and invariant mass, discussed previously, and were used in the online trigger. The third quantity, transverse momentum, was first added to the analysis in PASS1. The collinearity angle θ_c can be adversely affected by multiple scattering θ_{MS} in the vacuum window described by the formula [13]:

$$\theta_{MS} = \frac{14.1\text{MeV}}{p\beta} \sqrt{L/L_R} \left[1 + \frac{1}{9} \log(L/L_R) \right], \quad (13)$$

where L is the distance travelled, and L_R is the radiation length within the medium passed. Thus, we see that the error in collinearity introduced by multiple scattering $\Delta\theta$ is inversely

proportional to the momentum— $\Delta\theta \propto 1/p$. Transverse momentum, however, is defined as $p_t = p \sin \theta_c$ or $p_t = p\theta_c$ in the small angle approximation. Thus, the error in p_t is independent of the momentum— $\Delta p_t = p\Delta\theta \propto \text{constant}$. Both the collinearity and transverse momentum were carried through the entire analysis. In the end, however, transverse momentum was dropped in favor of collinearity in order to maintain backward compatibility with the 1988 analysis.

As can be seen in Figure 19, the PASS1 code contains three data streams. The first, the raw data prescale stream, sent every 5000th event to pattern recognition and on to the output tape, regardless of the event type and the outcome of pattern recognition, and without testing collinearity, transverse momentum or invariant mass. This produced a sample of raw events, weighted over the entire run, for later testing.

The second stream handled the L1 minimum bias events, and split them into two substreams. One substream was prescaled by 60 and sent to pattern recognition. Those events which passed pattern recognition were then sent to the output tape without testing on the event quantities. This became the minimum bias sample weighted over the run and was used to obtain the semileptonic samples used in various offline studies. The second substream was prescaled by three and sent to pattern recognition. Those events which passed were then cut if $p_t^2 > 800 \text{ MeV}^2$ and if $\theta_c > 10 \text{ mrad}$. Note that an event had to fail both the transverse momentum cut and the collinearity cut to fail here. Finally, the invariant mass, based on a $\pi\pi$ event type, was required to fall within the range of 470–530 MeV/c^2 exclusive. This was the $\pi\pi$ normalization sample.

The third stream handled the two-body physics events: μe , $e\mu$, ee , $\mu\mu$, and $\pi\pi$. As stated before, the L3 collinearity cut was reduced from $\theta^2 < 20 \text{ mrad}^2$ to $\theta^2 < 10 \text{ mrad}^2$ partially into the data run. PASS1 imposed a uniform L3 collinearity cut by eliminating all events with a L3 collinearity of greater than 10 mrad^2 immediately. All two-body events were then required to pass pattern recognition. The pattern recognition results were then used to cut on collinearity and transverse momentum using the same limits as the $\pi\pi$ normalization sample above. Finally, the invariant mass was calculated, based on the event type from the L3 decision, and required to fall in the range 470–530 MeV/c^2 .

PASS1 was run at the BNL Computer Center on 1935 6250 bpi raw data tapes. An additional set of 1000 tapes was processed at the Cornell Computer Center. The PASS1 results were output to 101.38,000 bpi IBM 3480 cartridges. A total of 5,325,220 physics events were written out with the event distribution given in Table 3 [38].

event type	fraction	total
raw prescale 5000	0.9%	45,846
min bias prescale 60	8.6%	458,743
min bias prescale 3 pass $\pi\pi$	5.1%	269,789
physics pass μe	10.5%	560,781
physics pass $e\mu$	11.7%	620,566
physics pass $\mu\mu$	37.2%	1,981,659
physics pass ee	1.8%	97,876
physics pass ee	27.0%	1,437,974

Table 3: PASS1 events written to tape.

5.3 Track Fitting

The second offline stage in processing the data was track fitting. The track fit performed by pattern recognition was insufficient for detailed analysis of the events. To obtain more accurate track information, two different tracking algorithms were used—referred to as FT and QT fitting. The application of track fitting to the physics data tapes was called PASS2.

5.3.1 QT Fitting

The QT fitting package [39] did not incorporate a track fit *per se*, but rather an iterative calculation of the track parameters which best satisfied the observed hit positions in the drift chambers. The track parameters calculated by QT were the track direction (x and y) and the track momenta at DC1 and DC5. QT determined these quantities separately for the front and back halves of the spectrometer. The quality of the fit was judged by the track χ^2 .

QT took the pattern recognition parameters as a starting point for the process. Using Rutta-Kruege, QT swam the particle from DC1 to DC2 and then on to DC3. The theoretical hits in DC2 and DC3 were then compared to the data hits. If the DC2 x or y positions deviated by more than a set amount, the track direction at DC1 was modified. If the DC3 x position was off, the track momentum was modified. Requiring the DC3 y position to match was not permitted by the degrees of freedom. QT then swam the particle using the new parameters and repeated the process until the theoretical and data points agreed. The program then repeated the swimming process, starting at DC5 and working upstream to DC3. The QT algorithm also repeated the entire process for all left/right ambiguity solutions.

Next, QT calculated a χ_x^2 and a χ_y^2 for the tracks based on the difference between the upstream and downstream track parameters at DC3 using the following formula:

$$\chi_x^2 = \left(\frac{\delta p}{\sigma_{\delta p}} \right)^2 + \left(\frac{\delta \theta_x}{\sigma_{\delta \theta_x}} \right)^2 \quad (14)$$

$$\chi_y^2 = \left(\frac{\delta y}{\sigma_{\delta y}} \right)^2 + \left(\frac{\delta \theta_y}{\sigma_{\delta \theta_y}} \right)^2 \quad (15)$$

where δp is the difference between the front and back momentum, δy is the difference in the y position at DC3 between the front and back parameters, and $\delta \theta_x$ and $\delta \theta_y$ are the differences in track angle at DC3 between front and back for x and y respectively. QT assumed no correlation between the contributions of the χ^2 . The σ are the expected rms deviations for the measurement at a given momentum. The $\sigma(p)$ were calculated from Monte Carlo simulations using multiple scattering and chamber positional resolution, each of which was treated separately and added in quadrature. The simulations used a standard $150 \mu\text{m}$ chamber resolution, and the results were then scaled by the actual chamber resolutions.

At this point, QT had sufficient information to resolve the remaining left/right ambiguities by selecting the track candidate with the best χ^2 . Finally, QT reconstructed a decay vertex just as was done in pattern recognition, except that the vertex was not chosen as the midpoint of the DOCA, but by the weighted uncertainties of each track.

5.3.2 FT Fitting

The FT algorithm [40] was a mathematically rigorous calculation and minimization of the track χ^2 , based on a comparison of the actual data points with *theoretical* hit points.

FT started with a 5-vector $\vec{a} \equiv (x, y, \frac{dx}{dy}, \frac{dy}{dx}, \frac{q}{p})$ defining the position and slope of the track at the vacuum window, as well as the charge over momentum (used rather than p , since the magnetic bend scales as $1/p$). These parameters were then projected downstream through the drift chambers to obtain the theoretical hit points, ignoring both multiple scattering and chamber resolution. This ideal track does not follow the actual path of the particle through the magnetic field, leading to potential problems. To avoid these problems, FT initially fitted the actual hits and recorded the actual field strength observed by the track. The actual field strength was then used in swimming the ideal track.

The FT program next tested the agreement between the data and theoretical hit points

utilizing the following χ^2 formula:

$$\chi^2(\vec{\alpha}) = \sum_i^{n=20} \sum_j^{n=20} (x_i^{data} - x_i^{theory}) W_{ij}^x (x_j^{data} - x_j^{theory}). \quad (16)$$

The indices i and j run over the twenty drift chamber measurements, i.e. the two x and two y planes within each chamber module are treated separately. The weight matrix W_{ij}^x is the inverse of the covariance or error matrix E_{ij}^x .

The error matrix is the sum of two matrices:

$$E_{ij}^x(p) = E_{ij}^{DC} + \frac{E_{ij}^{MS}}{p^2} \quad (17)$$

where E_{ij}^{DC} is the uncorrelated error matrix resulting from the drift chamber resolution of $\sim 150 \mu\text{m}$, and E_{ij}^{MS} is the correlated error matrix resulting from multiple scattering. For E_{ij}^{DC} , FT used a diagonal matrix whose elements were simply the individual drift chamber resolutions. The matrix E_{ij}^{MS} was calculated from Monte Carlo events which were swum through the detectors both with and without multiple scattering.

Having created a track χ^2 , FT determined the track parameters which minimized it. The FT routine varied the elements of $\vec{\alpha}$ utilizing a *Newton Step* procedure to minimize $\chi^2(\vec{\alpha})$.

After FT determined the track parameters for each side of the spectrometer, it then found the parameters for the 9-vector which defined the decay vertex:

$$\vec{\beta} \equiv \left(x, y, z, \frac{dx_1}{dz}, \frac{dy_1}{dz}, \frac{q_1}{p_1}, \frac{dx_2}{dz}, \frac{dy_2}{dz}, \frac{q_2}{p_2} \right). \quad (18)$$

Again, FT constructed a χ^2 , this time based on the track parameters for $\vec{\alpha}_1$ and $\vec{\alpha}_2$ determined earlier, and defined as follows:

$$\chi^2(\vec{\beta}) = \sum_i^{n=10} \sum_j^{n=10} (\alpha_i^{data} - \alpha_i^{theory}) W_{ij}^\alpha (\alpha_j^{data} - \alpha_j^{theory}). \quad (19)$$

Here, the weight matrix W_{ij}^α is the inverse of the covariance matrix found by the combination of the individual track matrices, modified to account for multiple scattering within the vacuum window. Owing to the judicious choice for the parameters in $\vec{\beta}$, the minimization of the χ^2 was accomplished by a single matrix inversion, using a reasonable estimate of $\vec{\beta}$ (although any initial $\vec{\beta}$ would do).

With the event now defined by the parameters in $\vec{\beta}$, FT proceeded to calculate various quantities, such as the invariant mass and collinearity.

5.3.3 PASS 2

The second stage of data reduction was performed by the PASS2 code. The primary purpose of the PASS2 code was not to reduce the total amount of data, although it did eliminate some events, but rather to obtain accurate tracking information for studies which would then be used to determine the next series of data selection cuts.

The PASS2 code divided events into the same data streams used in PASS1 (see Section 5.2.2). As can be seen in Figure 20, pattern recognition was rerun on all events. This was necessary in order to obtain the wire hit information which PASS1 did not record so as to save space on the PASS1 output cartridges. (It was easier to rerun pattern recognition on a smaller number of PASS1 cartridges than to run PASS2 on a much larger number of PASS1 cartridges containing the wire hit information). The PASS2 code then performed both QT and FT fitting on all events.

As with PASS1, the prescaled raw data events were written out regardless of the results of the PASS2 code. For the other data streams, events were required to pass either QT or FT fitting. Those events which failed either QT or FT were flagged and written out for later study. Events failing both QT and FT were also written out for later study, but were dropped from the analysis stream. A calculation of the invariant mass was done for the five two-body event types and for the minimum bias $\pi\pi$ sample. PASS2 used the same mass cut as PASS1, 470 MeV–530 MeV exclusive. However, the better mass resolution of the fitting routines caused approximately 20% of the PASS1 events to fail the 470 MeV cut. PASS2 also recalculated the collinearity and transverse momentum based on QT and FT, but no cuts were made on these quantities. In addition, no cuts were made on the FT or QT track and vertex chi-squares. As a final task, PASS2 ran the track counter association code (see Section 5.4.1) on the two-body events. This information was not used to make event identifications but rather to test for any particle identification detector problems.

PASS2 was run on 78 PASS1 output cartridges at the Cornell facility. An additional 22 cartridges were run at BNL. The final PASS1 cartridge was dropped from the analysis since the data was taken in the final week of the run, after the drift chambers had been moved for tests for the 1990 run. No drift chamber survey existed for this data and therefore it was unuseable. Table 4 gives a breakdown of the 4,360,168 physics events written out by PASS2 [41].

event type	fraction	total
raw prescale 5000	1.0%	45,445
min bias prescale 60	10.4%	453,333
FT μe	8.0%	347,457
FT $e\mu$	8.4%	365,051
FT $\mu\mu$	31.7%	1,383,451
FT ee	1.7%	72,122
FT $\pi\pi$	32.2%	1,403,911
FT min bias $\pi\pi$	5.9%	256,922
QT μe	8.0%	347,454
QT $e\mu$	8.5%	368,531
QT $\mu\mu$	31.8%	1,386,864
QT ee	1.6%	71,261
QT $\pi\pi$	32.0%	1,393,708
QT min bias $\pi\pi$	5.8%	253,968

Table 4: PASS2 events written to tape.

5.4 Event Identification

Up to this point in the analysis, all event identification had been based on the L1 trigger, which used very broad criteria for classification. This did not present any problems for pattern recognition or track fitting, since these programs were designed to find any tracks in the spectrometer, and their mass cuts based on L1 particle identification were very loose. However, the L1 ID was not sufficient for the tighter cuts which needed to be imposed in the final analysis.

The detailed particle identification was performed by the track counter association code. Results from track counter association were then used in the event stripping job to separate the physics events into the various decay modes of interest.

5.4.1 Track Counter Association

Following fitting, there were two sets of possibly correlated data for each event: first, the fitted track information from the spectrometer, and second, the hit information from the downstream particle identification detectors. It was necessary to determine which, if any, of the detector hits were actually associated with the upstream tracks, and the efficiency of the cuts used to determine that information.

Track counter association (TKC) for all detectors used the same basic principle to correlate the spectrometer and detector information. A given hit in each detector produced certain parameters, for instance x position. The upstream track information could be projected back to produce a simulated hit in that detector with its parameters. If one takes a sample of particles which are known to be associated with an upstream track, one can compare the simulated and actual hits and form a probability distribution for each parameter. One can then reverse the process and determine the probability that any hit from an unknown source in the detector is associated with a given upstream track.

Čerenkov and Lead Glass

The primary purpose of the Čerenkov and lead glass detectors was to identify electrons from the $K_L \rightarrow \mu^\pm e^\mp$ and $K_L \rightarrow e\bar{e}$ decay modes. Their use in the $K_L \rightarrow \mu\bar{\mu}$ analysis was limited to identifying electrons from the $K_L \rightarrow \pi^\pm e^\mp \nu$ mode to test for electron misidentification in the muon hodoscope and rangefinder, as a veto in pion selection for similar studies for pions, and as a veto in muon selection for the $K_L \rightarrow \pi^\pm \mu^\mp \nu$ events used in establishing the muon track counter association codes for the MHO and MRG. No veto was used in either the CER or the PBG in the identification of $K_L \rightarrow \pi\bar{\pi}$ events for normalization, nor in the identification of $K_L \rightarrow \mu\bar{\mu}$ events. Only a brief discussion of track counter association is given here for the Čerenkov and lead glass because of their limited use in the $K_L \rightarrow \mu\bar{\mu}$ analysis.

For the Čerenkov counter, the detector identification parameters were the phototubes hit and the timing for those hits. The raw times from the ADCs were first corrected using phototube-dependent constants which were determined from offline analysis of minimum bias electrons, such that each tube had a corrected time distribution centered on zero and of minimum width. The CER track counter code took the track information from the fitting routines and projected the DC5 parameters to the upstream window of the Čerenkov counter using linear transport. The routine then projected a Čerenkov cone of light with an opening angle of 16.7 mrad, corresponding to $\beta = 1$ in the N_2 -He gas mixture, downstream to the mirror locations. Track counter association produced simulated phototube hits based on the mirrors hit by this cone. It then looped over the actual and simulated hits, choosing the actual hit with the best corrected time corresponding to a simulated hit. A good electron signal was required to have a corrected time within ± 4 ns of zero.

The electron ID efficiency of the Čerenkov was measured to be 90.1% for electrons

from the decay mode $K_L \rightarrow \pi^\pm e^\mp \nu$. This efficiency was momentum dependent and had to be corrected for the different momentum spectra for electrons from the $K_L \rightarrow \mu^\pm e^\mp$ and $K_L \rightarrow e\bar{e}$ modes. The corrected efficiencies for the latter modes were 89.2% and 89.5% respectively. For muons and pions, the probability of a good electron signal in the CER was 1% [29].

For the lead glass, the detector parameter was the energy deposited within the PBG array. The code first determined the amount of energy deposited in each block of the array. This was calculated from the raw ADC signal *via* a calibration constant for each block (determined from dedicated calibration tapes taken at intervals throughout the run) given in GeV/pC. Next the track counter code projected the fitted information at DC5 to the back blocks using linear transport. The code then determined three energy sums. The first, E_{conv} , was the sum of the energy deposited in the converter block through which the projected track passed, plus the energy in the blocks to either side in x . The second, E_{back} , was the sum of the energy in the back block hit by the projected track, plus the energy in all eight adjacent back blocks in x , y , and diagonally. The final sum, E_{pbg} , was simply the sum of E_{conv} and E_{back} .

For electrons, two energy ratios were of interest, E_{conv}/E_{back} and E_{pbg}/p . Electrons tended to deposit all their energy in the PBG array, giving $E_{pbg}/p \simeq 1$. Muons and pions generally gave $E_{pbg}/p \ll 1$ since they deposited very little energy in the PBG *via* Čerenkov radiation. Pions which interacted hadronically in the PBG could simulate an electron E_{pbg}/p . However, the interaction probability for pions was three times higher in the back blocks than in the converters, causing most pion hadronic showers to occur in the back blocks. This produces a small E_{conv}/E_{back} ratio. Electrons, on the other hand, generally began their showers in the converter blocks, depositing roughly 1/4 of their energy there. A scatter plot of these two ratios showed electrons grouped in the center of the plot around $E_{pbg}/p = 1$ and $E_{conv}/E_{back} = 0.3$, while pions and muons clustered along the axes. The PBG electron ID cuts were formed by taking the region of the scatter plot above $E_{pbg}/p = 0.75$ and $E_{conv}/E_{back} = 0.045$, with a small portion cut out near the origin.

The PBG electron ID efficiency for electrons from the decay $K_L \rightarrow \pi^\pm e^\mp \nu$ was 95.7%. As with the CER, this efficiency was momentum dependent and had to be corrected for other decay modes. The efficiency for electrons from $K_L \rightarrow \mu^\pm e^\mp$ was 95.3% and for $K_L \rightarrow e\bar{e}$ it was 95.5%. The probability for a muon to give a good electron signal was 2% and for pions it was 4% [42].

Muon Hodoscope

The muon hodoscope produced five items of data per hit; three hit times $t_{x\text{top}}$, $t_{x\text{bot}}$, and t_y corresponding to the two x phototubes and the y phototube respectively; and the x and y hit position. For the simulated hit, the upstream track was projected from DC5 to the MHO by linear transport to produce an x_{sim} and y_{sim} position, and the event time was taken from the TSC time t_{tsc} . From these quantities one can define four parameters on which to base the track counter association.

The first two quantities are:

$$x_{\text{dif}} = x - x_{\text{sim}} \quad (20)$$

$$y_{\text{dif}} = y - y_{\text{sim}} \quad (21)$$

which were used as the basis for the space match probabilities in x and y . Distributions for x_{dif} and y_{dif} were obtained using muons from the $K_L \rightarrow \pi^\pm \mu^\mp \nu$ decay mode, and fitted to a convolution of a standard Gaussian distribution and a rectangle (for a MHO counter) to obtain the following probability distribution [30]:

$$P(x) = \frac{1}{2w} \left(\text{ERFC} \left(\frac{-w/2 + \mu - x}{\sigma\sqrt{2}} \right) - \text{ERFC} \left(\frac{-w/2 + \mu - x}{\sigma\sqrt{2}} \right) \right) \quad (22)$$

where w is the width of a MHO counter, x is either x_{dif} or y_{dif} , μ and σ are the Gaussian fit parameters, and

$$\text{ERFC}(x) = \frac{2}{\sqrt{\pi}} \int_x^\infty e^{-t^2} dt. \quad (23)$$

The second two quantities are the time match probabilities:

$$T_1 = t_y - \hat{t}_x \quad (24)$$

$$T_2 = \frac{t_y + \hat{t}_x}{2} - t_{\text{tsc}} \quad (25)$$

where

$$\hat{t}_x = \begin{cases} t_{x\text{bot}} & \text{if } |t_{x\text{bot}} - t_y| \leq |t_{x\text{top}} - t_y| \\ t_{x\text{top}} & \text{otherwise.} \end{cases} \quad (26)$$

Ideally, a good MHO hit should give an intime hit for both $t_{x\text{top}}$ and $t_{x\text{bot}}$ and one could use the mean of the two. However, the code allowed for the possibility that one or the other was missing or out of time due to phototube inefficiency, by defining \hat{t}_x as in Equation 26.

The time distributions were fitted using the $K_L \rightarrow \pi^\pm \mu^\mp \nu$ muon sample. For T_1 , the resulting probability distribution function was a simple Gaussian:

$$P(x) = \frac{1}{\sqrt{2\pi\sigma^2}} e^{-(x-\mu)^2/2\sigma^2}. \quad (27)$$

T_2 required a more complicated probability function resulting from the three Gaussian functions from the individual phototube times:

$$P(x) = \frac{1}{(2\pi)^{3/2} \sigma^3 \alpha_1 \alpha_2} e^{-\alpha_2^2 x^2 + \beta_2^2 / 4\alpha_2^2} \times \left(2 - \text{ERFC} \left(-x\alpha_2 + \frac{\beta_2}{2\alpha_2} \right) + \text{ERFC} \left(x\alpha_2 + \frac{\beta_2}{2\alpha_2} \right) \right) \quad (28)$$

$$\begin{aligned} \alpha_1^2 &= \frac{3}{2\sigma^2} \\ \alpha_2^2 &= \frac{1}{2\sigma^2} - \frac{1}{4\alpha_1^2\sigma^4} \\ \beta_2 &= \frac{z}{2\alpha_1^2\sigma^4}. \end{aligned}$$

For a rigorous derivation of Equation 29, see Reference [43].

Since x_{sim} and y_{sim} did not take into account multiple scattering upstream of the MHO, the space distributions were momentum dependent (see Equation 13). Less obvious is the fact that the time distributions were also momentum dependent. This arose from the correction in the photomultiplier tube times based on the distance of propagation from the hit to the phototube. This distance was calculated using the simulated hit information. For that reason, the space and time distributions were fit for several momentum bins, and the σ were obtained as a function of momentum.

Next, the time and space distributions and the probability functions were used to obtain the four muon confidence levels for the MHO: $CL(x_{dif})$, $CL(y_{dif})$, $CL(T_1)$, and $CL(T_2)$. Thus, given the position and time of a hit in the MHO and the momentum of the upstream track to which the hit was to be associated, one obtained a total confidence level CL_{MHO} combining the preceding individual confidence levels. Particles for which $CL_{MHO} > 0.0005$ were considered to be muons. The MHO muon efficiency for the $K_L \rightarrow \pi^\pm \mu^\mp \nu$ mode was 97.5%. As shall be discussed in Section 6.4.5, this efficiency had to be corrected for the different momentum spectra for muons from $K_L \rightarrow \pi^\pm \mu^\mp \nu$ and $K_L \rightarrow \mu \bar{\mu}$. The probability for a pion to be misidentified as a muon was 5.6%. This arose primarily from muons from pion decays upstream, and from pion punchthrough of the muon filter. The probability for

a electron to be misidentified as a muon was 0.1%, owing to accidental hits in the MHO [30].

Muon Rangefinder

For the muon rangefinder, particle identification was based on the momentum measured by the rangefinder. As a muon passed through the MRG, it lost energy at a known rate. By determining the depth to which the muon penetrated the rangefinder, one could reconstruct the original momentum. Other particle types were susceptible to interactions in the degrader material to which muons were immune (for instance, hadronic interactions for pions), preventing them from penetrating the MRG to the same depth as a muon of the same momentum. Also, particles which resulted from the interaction of the original kaon decay products upstream generally would not carry the full momentum of the original particle. Thus, by comparing the momentum measured in the MRG to that measured by the spectrometer, one could discriminate muons from other particle types.

Determining the rangefinder momentum for a particle was a three-step procedure. The first step was similar to the track counter association procedure in other particle detectors, specifically to the MHO space match probabilities. Within each gap, the actual x and y hits were compared to simulated hits produced by projecting the track information at DC5 downstream to the MRG *via* linear transport. Using muons from the $K_L \rightarrow \pi^\pm \mu^\mp \nu$ mode, the hit distributions

$$x_{dif} = |x - x_{sim}| \quad (29)$$

$$y_{dif} = |y - y_{sim}| \quad (30)$$

were obtained. Here, the procedure differed from that of the MHO space match probabilities in two respects. First, x_{dif} and y_{dif} were defined as the absolute value of the difference between the actual and simulated hits (compare with Equation 20 and Equation 21). Second, the confidence levels produced for the MRG were not continuous functions but rather discrete look-up tables. The x_{dif} distribution was divided into 12 bins (16 bins for y_{dif}), representing the maximum x_{dif} (y_{dif}) for one x -plane (y -plane), where each bin is one extrusion in width. The confidence level for each bin was obtained from the following equation:

$$CL_i = \frac{\sum_{j=i}^n N_j}{\sum_{k=1}^n N_k} \quad (31)$$

where N is the number of events per bin and n is the number of bins. As with the MHO confidence levels, the MRG levels had to be calculated as a function of momentum, since the simulated hits did not take into account multiple scattering. This entire procedure had to be repeated for each of the thirteen gaps. Having obtained the MRG confidence level tables, the track counter code could now assign space match probabilities to hits from unknown tracks in the MRG.

The second step in MRG track counter association was to examine the hits determined by the confidence level tables to be potentially track-associated for actual tracks in the MRG. The code first made a loose cut on the space match confidence level to produce a path in the rangefinder for a potential track, centered on the simulated track. This path widened as it progressed deeper into the MRG, since a given confidence level cut covered more extrusions in the rear gaps than in the forward gaps. (This occurs because of multiple scattering in the $K_L \rightarrow \pi^\pm \mu^\mp \nu$ muon sample.) This expansion of the path prevented the loss of a track which multiple scattering forced to deviate widely from the simulated track. However, it also permitted the association of accidental hits with the track. To eliminate these accidental associations, the code made a tight cut on the difference between a hit found in a given gap and the hit found in the previous gap, since multiple scattering between individual gaps was not as great as for the MRG as a whole. A given track in the MRG was considered to end when no track associated hit could be found in two consecutive gaps. The track counter association code treated x and y separately while locating tracks. The code then used the longer of the x and y tracks as the depth of penetration into the MRG (defined as the *actual stop gap* or as just the *actual gap*).

The final step was to determine whether or not the track found above was consistent with a muon track upstream. This was accomplished by using the spectrometer momentum to determine an expected depth of penetration (defined as the *expected gap*). A particle was considered to be a muon when the actual gap minus the expected gap was greater than or equal to -3. For muons from the $K_L \rightarrow \pi^\pm \mu^\mp \nu$ decay mode, the MRG muon ID efficiency was 99.13%. As shall be discussed in Section 6.4.5, this efficiency had to be corrected for the different momentum spectra for muons from $K_L \rightarrow \pi^\pm \mu^\mp \nu$ and $K_L \rightarrow \mu \bar{\mu}$. The probability for a pion to produce a false muon signal was 17.1% and for an electron it was 42.5%.

At first glance, the misidentification probabilities for pions and especially for electrons seem extraordinarily high. After all, one would not expect any electrons or their shower products to penetrate the muon filter, much less give a track in the MRG. As for pions,

studies showed that only 1.4% penetrated the muon filter, or underwent a hadronic interaction producing a daughter which penetrated the muon filter. These would not be expected to produce a MRG track either. Muons from pion decay downstream of the spectrometer could produce tracks in the MRG and studies showed this to occur in 14.3% of the pion tracks, but this scarcely accounts for the high pion misidentification (since not all these tracks will pass the MRG cut because of the momentum carried off by the undetected neutrino). The answer lies in the definition of the MRG cut. If the actual stop gap is zero, i.e. no track in the MRG, and the expected gap is 3 or less, the actual gap minus the expected gap will be greater than or equal to -3. Thus all low momentum pions and electrons were guaranteed to pass the MRG cut. This had the potential to cause problems in both the $K_L \rightarrow \mu^\pm e^\mp$ and $K_L \rightarrow \mu\bar{\mu}$ measurements. Tighter cuts were devised and tested for the MRG (see Appendix A) which lowered the misidentification probabilities. For the $K_L \rightarrow \mu^\pm e^\mp$ measurement, these tighter cuts would have lowered the overall sensitivity. Since background from $K_L \rightarrow \pi^\pm e^\mp \nu$ (where the π is misidentified as a μ) and from $K_L \rightarrow \pi^\pm \mu^\mp \nu$ (where the π is misidentified a μ and the μ is misidentified as an e) was not a problem, the tighter cuts were not implemented so as to maintain the highest possible sensitivity. In the case of $K_L \rightarrow \mu\bar{\mu}$, background from $K_L \rightarrow \pi^\pm e^\mp \nu$ (where the both the π and e are misidentified as muons) and from $K_L \rightarrow \pi^\pm \mu^\mp \nu$ (where the π is misidentified as a μ) was significant. However, a background subtraction (see Section 6.2.4) was necessary even with the tighter cuts. Therefore, for consistency with the $K_L \rightarrow \mu^\pm e^\mp$ analysis, and to avoid the loss of good $K_L \rightarrow \mu\bar{\mu}$ events, the looser MRG cut was retained.

5.4.2 Event Stripping

The final stage in reducing the data was event stripping. In this stage, loose cuts were performed on the particle identification from track counter association, using both FT and QT tracks as input for TKC, and passing events which satisfied the particle identification requirements for either FT or QT tracks. For minimum bias events, no particle identification requirements were imposed. Electrons from $K_L \rightarrow \mu^\pm e^\mp$ were required to have a CER time less than 6 ns, an $E_{pbg}/p \geq 0.75$, and an $E_{conv}/E_{pbg} > 0$. Muons from $K_L \rightarrow \mu^\pm e^\mp$ were required to have a confidence level greater than 0.001 in the MHO and an actual minus expected gap greater than -4. Muons from $K_L \rightarrow \mu\bar{\mu}$ were only required to have a track counter associated hit in all four MHO modules, regardless of confidence level. There were 258,563 minimum bias events, 254,716 $K_L \rightarrow \mu\bar{\mu}$ candidates, and 169,396 $K_L \rightarrow \mu^\pm e^\mp$ or

$K_L \rightarrow e\bar{e}$ candidates.

Chapter 6

Data Analysis

6.1 Overview

A measurement of the branching fraction of $K_L \rightarrow \mu\bar{\mu}$, requires two items of information, the total number of $K_L \rightarrow \mu\bar{\mu}$ events ($N_{\mu\mu}$) observed, and the total number of K_L particles (N_{K_L}) produced. Since E791 did not detect K_L particles directly, the total number of $K_L \rightarrow \pi\bar{\pi}$ events observed was used to determine N_{K_L} from the measured branching fraction for $K_L \rightarrow \pi\bar{\pi}$. At the simplest level, this produces the following formula for the branching fraction:

$$B(K_L \rightarrow \mu\bar{\mu}) = \frac{N_{\mu\mu}}{N_{K_L}} = B(K_L \rightarrow \pi\bar{\pi}) \frac{N_{\mu\mu}}{N_{\pi\pi}} \quad (32)$$

where $B(y)$ are the branching fractions, and $N_{\pi\pi}$ is the observed number of $K_L \rightarrow \pi\bar{\pi}$ events, also referred to as the *normalization sample*.

Experimental realities force certain correction factors for Equation 32. The observed number of $K_L \rightarrow \mu\bar{\mu}$ events was dependent on the L1 muon identification. $N_{\pi\pi}$ was not, since the normalization sample was taken from minimum bias events for which L1 made no particle ID decision. Thus, a correction for the L1 muon ID efficiency (ϵ_{L1}) must be made. By contrast, L3 decisions were required for both $K_L \rightarrow \pi\bar{\pi}$ and $K_L \rightarrow \mu\bar{\mu}$ events. Thus both $N_{\pi\pi}$ and $N_{\mu\mu}$ must be corrected by the L3 efficiency for both $K_L \rightarrow \pi\bar{\pi}$ and $K_L \rightarrow \mu\bar{\mu}$ ($\epsilon_{L3\pi\pi}$ and $\epsilon_{L3\mu\mu}$ respectively), which are not necessarily the same. $N_{\mu\mu}$ must also be corrected for the particle ID efficiencies for the MHO and MRG ($\epsilon_{\mu\mu}$). An additional correction (ϵ_{INT}) arises from the susceptibility of pions to various interactions to which muons are immune, and which reduces the observed $K_L \rightarrow \pi\bar{\pi}$ events. $N_{\pi\pi}$ is also subject to inflation from $K_S \rightarrow \pi\bar{\pi}$ events, which is corrected by ϵ_{κ_s} . During the course of the experiment, not all

minimum bias events were written to tape. Therefore, $N_{\pi\pi}$ was corrected by the prescale factor for minimum bias events, combining both the online and offline prescale factors. The final correction factors arise from the geometry of the E791 detector. Only a small fraction of the $K_L \rightarrow \pi\bar{\pi}$ and $K_L \rightarrow \mu\bar{\mu}$ events actually traverse the E791 apparatus. However, this geometric acceptance differs for the two decay modes, and Equation 32 must be corrected by their ratio ($A_{\pi\pi}/A_{\mu\mu}$).

Applying all correction factors in Equation 32, one obtains the following equation for the $K_L \rightarrow \mu\bar{\mu}$ branching fraction:

$$B(K_L \rightarrow \mu\bar{\mu}) = B(K_L \rightarrow \pi\bar{\pi}) \frac{N_{\mu\mu} A_{\pi\pi} \epsilon_{\kappa_2} \epsilon_{\text{INT}} \epsilon_{L3\pi\pi}}{\text{PRESCALE} * N_{\pi\pi} A_{\mu\mu} \epsilon_{\mu\mu} \epsilon_{L1} \epsilon_{L3\mu\mu}} \quad (33)$$

In the sections which follow, the various factors in Equation 33 shall be discussed, and the branching fraction calculated. As discussed previously, FT and QT fitting were independently applied through the entire analysis. In the subsequent sections, only FT results will be discussed. In Section 6.6, the QT results will be referred to as a check on the branching fraction calculation.

6.2 $K_L \rightarrow \mu\bar{\mu}$ Sample

After event stripping, there were 244,716 $K_L \rightarrow \mu\bar{\mu}$ candidates. To determine which of these were indeed $K_L \rightarrow \mu\bar{\mu}$ events, three sets of cuts were imposed on the sample. The first set consisted of event quality cuts which determined whether or not the candidate event contained sufficient and consistent information to result from a K_L decay. The second set of cuts was based on tracking information, and determined whether the kinematics of the candidate event were consistent with the $K_L \rightarrow \mu\bar{\mu}$ hypothesis. The final set of cuts was based on the particle identification decisions of the MHO and MRG. Finally, the $K_L \rightarrow \mu\bar{\mu}$ sample contained background events from semileptonic decays which were subtracted to obtain $N_{\mu\mu}$.

6.2.1 Event Quality Cuts

The first event quality cut concerned the number of crates written to tape for the event. As discussed previously, there were 21 data crates to be read out. Even if the detectors contained within a given crate registered no hits, data words were passed from the crate.

event type	PASS2 fraction	missing crate fraction
μe	17.7%	18.5%
$e\mu$	18.3%	22.1%
$\mu\mu$	35.0%	38.2%
ee	7.3%	8.2%
min bias	16.3%	14.2%
$\pi\pi$	34.8%	28.3%
$\pi\pi$ prescale	31.8%	25.7%

Table 5: Comparison of the fraction of events, by Level 1 trigger type, which have missing crates to the fraction of events in the PASS2 input.

On occasion, however, hardware problems caused an event to fail to read in a crate, predominately in calibration events, but occasionally in physics events as well. During PASS2, a study was performed to determine if physics events with missing crates were biased toward any given event type [41]. Table 5 shows a comparison of the fraction of events read in by PASS2 by L1 trigger type and the fraction of the physics triggers with missing crates, again by L1 trigger type. Since there was no apparent correlation between trigger type and missing crates, all such events were cut from the analysis. For $K_L \rightarrow \mu\bar{\mu}$ this eliminated 106 events. A similar problem arose in the L1 trigger bits, in which certain physics events lacked pedestal information (the 50 Hertz flag). These events, 5 $K_L \rightarrow \mu\bar{\mu}$ candidates, were also cut.

The next event quality cut was the elimination of all events from RUN 5377. At some point during RUN 5377, the high voltage power supply to the MRG overloaded. After the loss of the supply, individual wires were not at the nominal +2650 volts but at variable voltages along the capacitive decay curve. The efficiency for particle detection quickly dropped to zero as the wire voltages decayed. However, for a brief period of time, the MRG would have continued to detect potential muon tracks, but the drastically differing wire efficiencies made reconstruction of those tracks extremely difficult if not impossible. In addition, some good muon tracks would exist in the time frame prior to the supply overload, and subsequent to its return. For $K_L \rightarrow \pi\bar{\pi}$ events, there would be no corresponding drop in detection efficiency, since the MRG was not used in their detection. As there was no way to determine the exact time period within RUN 5377 during which $K_L \rightarrow \mu\bar{\mu}$ detection was compromised, there was no way to correct the $K_L \rightarrow \pi\bar{\pi}$ sample. Hence, the entire run was deleted. This eliminated 75 $K_L \rightarrow \mu\bar{\mu}$ candidates.

The final event quality cut was based on the pattern recognition reconstructed event

time, *TIMEPZ*. Studies of the MHO [30] showed a correlation between the MHO times and *TIMEPZ*, resulting in a correction to the MHO times (see Section 5.4.1). For some events, the event time was quite large (10 ns) rather than falling near zero. This cannot be corrected for within the MHO muon ID efficiency, as that is calculated on a single muon basis and then applied to the dimuon event (see Section 6.4.5), resulting in double counting for an event in which *TIMEPZ* and hence both muon times are out of time. For that reason, all events for which $|\text{TIMEPZ}| > 4$ ns were cut. Figure 21 shows the distribution for $K_L \rightarrow \mu\bar{\mu}$ candidates. This cut eliminated 25 $K_L \rightarrow \mu\bar{\mu}$ candidates.

6.2.2 Track Quality Cuts

A series of track quality cuts was applied to the $K_L \rightarrow \mu\bar{\mu}$ sample. The first simply required that the events not fail the fitting routines. This was not a particularly relevant cut in FT since virtually all events passing pattern recognition could be fit by FT. The same could not be said for QT. This apparent discrepancy between the fitting packages was not alarming, since the additional FT events invariably had either a bad track χ^2 or a bad front/back momentum match (see below) resulting from the very factors which failed QT. Only one $K_L \rightarrow \mu\bar{\mu}$ candidate failed FT track fitting.

Next, the fitted decay vertices of the events were required to lie within the vacuum decay region. Three positional cuts were imposed to enforce this requirement, $|x/z| < 0.0027$, $|y/z| < 0.0100$, and $z > 9.75$ m. The first two cuts were determined by the geometry of the decay volume. The z cut was further constrained to exclude the region of the decay volume immediately downstream of the last sweeping magnet. This was necessary to eliminate events whose kinematics were distorted by the fringe field of the magnet, and to eliminate semileptonic decays with a high reconstructed kaon mass (based on the $K_L \rightarrow \mu\bar{\mu}$ hypothesis), which were prime background events, and dominated this portion of the decay region. The number of $K_L \rightarrow \mu\bar{\mu}$ candidates failing these cuts were 9500, 1409, and 19,962 respectively.

The events were then tested for the quality of the track fit. A cut on the vertex χ^2 served to eliminate non-correlated tracks from near simultaneous but distinct kaon decays. A cut on the track χ^2 served to eliminate events with tracks caused by accidentals, and more importantly, $K_L \rightarrow \pi\bar{\pi}$ or semileptonic events in which the pion decayed within the spectrometer. Such decays would have “kinks” in their tracks caused by the decay as neutrinos carry off momentum, adversely affecting the quality of the track fit. These decays

were a potential background for $K_L \rightarrow \mu\bar{\mu}$. Figure 22 and Figure 23 show the vertex and track χ^2 distributions, respectively, for both data and Monte Carlo events. As can be seen in the plot, the track χ^2 for data events produced substantially larger tails in the χ^2 distribution than did Monte Carlo events. This probably arose from discrepancies in the magnetic field maps. Studies for the 1990 analysis showed significant problems with χ^2 for events in the fringe areas of the map (which were determined by extrapolation from the well-measured region in the magnet centers). The track χ^2 were significantly improved by adjusting the map in these regions [44]. Such improvements would probably have a similar effect on the 1989 data. For this analysis, a very loose cut on the track χ^2 was imposed due to the inadequacies described above. The vertex χ^2 was required to be less than or equal to 18, eliminating 9990 $K_L \rightarrow \mu\bar{\mu}$ candidates. The track χ^2 was only required to be less than or equal to 200, eliminating 80,216 $K_L \rightarrow \mu\bar{\mu}$ candidates.

Due to the looseness of the track χ^2 cut, greater emphasis was placed on the front/back momentum match cut to reject background from pion decays within the spectrometer. The two-magnet spectrometer allowed the momentum of a track to be measured twice. In the case of pions which decayed within the spectrometer, these two momenta would not agree, since the undetected neutrino must carry off some momentum. Tracks were required to have $2 \times (p_{back} - p_{front}) / (p_{back} + p_{front}) \leq 0.05$. Figure 24 shows this distribution of $K_L \rightarrow \mu\bar{\mu}$ candidates. This cut eliminated 5935 $K_L \rightarrow \mu\bar{\mu}$ candidates.

To further reduce accidental events caused by associating tracks from different but near simultaneous kaon decays, the charges for the tracks in each arm (determined by the direction of bend within the magnets), were required to be of opposite sign (two like-signed tracks could not possibly come from a single two-body kaon decay). This eliminated 18 $K_L \rightarrow \mu\bar{\mu}$ candidates. Additionally, all tracks were required to have a momentum greater than 1.5 GeV, the minimum momentum for a muon to penetrate the muon filter. This eliminated 650 $K_L \rightarrow \mu\bar{\mu}$ candidates.

The final track cuts were a series of aperture cuts designed to eliminate events which passed through significant amounts of material, and to insure that particles remained within the E791 apparatus' detection window. For example, in the original design for the experiment, an evacuated beam pipe was to be included to carry the neutral beam down the center of the experiment. This beam pipe was never constructed, but its flange connector was incorporated on the downstream end of the vacuum region, and overlapped part of the area of the Mylar decay windows. Additional cuts required that particles pass within the

magnets without intersecting the iron mirror plates. These cuts were of more importance in the Monte Carlo studies, as data events tended to be eliminated or never detected if they passed through “forbidden” regions. The Monte Carlo, however, did not model the multiple scattering or particle interactions which would occur within these areas, requiring that they be cut to force agreement between data and Monte Carlo. The aperture cuts eliminated 3468 $K_L \rightarrow \mu\bar{\mu}$ candidates.

6.2.3 Particle Identification

Finally, all $K_L \rightarrow \mu\bar{\mu}$ candidates were checked for consistency with the $K_L \rightarrow \mu\bar{\mu}$ hypothesis based on the particle identification decisions of the MHO and MRG. As discussed in Section 5.4.1, the muon hodoscope returned a confidence level for the probability that a given track was produced by a muon. Figure 25 shows the confidence level plot for the $K_L \rightarrow \mu\bar{\mu}$ candidates. The plot shows a pronounced peak at zero (non-muons) with a flat distribution out to one. The final cut for the MHO was chosen to be $C_L(MHO) \geq 0.0005$, eliminating 103,159 $K_L \rightarrow \mu\bar{\mu}$ candidates. The muon rangefinder cut (see Section 5.4.1) was based on the momentum match between the spectrometer and the MRG. Figure 26 shows the distribution of the actual minus expected gaps for the $K_L \rightarrow \mu\bar{\mu}$ candidates. The MRG cut was chosen to be $gap_{actual} - gap_{expected} > -3.5$, eliminating 4546 $K_L \rightarrow \mu\bar{\mu}$ candidates. The dependency of the final number for the branching fraction of $K_L \rightarrow \mu\bar{\mu}$ on these two cuts will be discussed in Section 6.6.

6.2.4 Number of $K_L \rightarrow \mu\bar{\mu}$

Figure 27 shows a scatter plot of the $K_L \rightarrow \mu\bar{\mu}$ candidates which survived all cuts imposed in the previous sections. Figures 28 and 29 show the projections along the mass and collinearity-squared axes, respectively. The mass plot in Figure 28 shows two distinct features. First, there is a large peak at $0.483 \text{ GeV}/c^2$ with a significant tail extending up into the K_L mass region. Second is a small peak centered at the K_L mass at $0.498 \text{ GeV}/c^2$. The collinearity plot in Figure 29 also shows two distinct features. First, there is a peak at 0.0 mrad^2 . Second is a non-uniform background extending to high collinearity-squared.

The peak in mass at $0.498 \text{ GeV}/c^2$ is the signal from actual $K_L \rightarrow \mu\bar{\mu}$ events, as one expects the reconstructed mass of a $K_L \rightarrow \mu\bar{\mu}$ event to be equal to the kaon mass. Similarly, the peak in θ_c^2 is also the expected signal from $K_L \rightarrow \mu\bar{\mu}$ events, as the vector addition of the two muon tracks should be equal to the initial kaon momentum (giving θ_c^2 of zero).

Of course, the finite mass resolution and the tracking uncertainties of the experimental apparatus smear the $K_L \rightarrow \mu\bar{\mu}$ signal, resulting in the distributions seen in the figures. The signal region for $K_L \rightarrow \mu\bar{\mu}$ events in Figure 27 was defined as the portion of the plot for which the reconstructed mass lies within the span of 492.67–502.67 MeV/ c^2 and θ_c^2 is less than or equal to 2 mrad². Three hundred (300) events lie within the signal region.

The two additional features in the mass and collinearity plots were indicative of background from misidentified semileptonic events, as discussed below. The number of events within the signal region must be corrected for any background events potentially present there to obtain a final $N_{\mu\mu}$.

$K_L \rightarrow \pi^\pm e^\mp \nu$ Background

The background events populating the high collinearity-squared region of the $K_L \rightarrow \mu\bar{\mu}$ scatter plot resulted from $K_L \rightarrow \pi^\pm e^\mp \nu$ events in which the pion either decays or was misidentified as a muon, and the electron was also misidentified as a muon. As can be seen in Figure 27, this background is almost uniformly distributed throughout the scatter plot. If a region of equal size to the signal region is defined, but located directly above the signal region (*i. e.* for $492.67 < M_I < 502.67$ MeV/ c^2 and $2.0 < \theta_c^2 < 7.0$ mrad²), one finds 14 background events from $K_L \rightarrow \pi^\pm e^\mp \nu$.

Since the background is not quite uniformly distributed, this figure cannot be used to estimate the background within the signal region by taking the number of background events in region of the scatter plot away from the signal box and of equal size. Instead, a straight line fit was attempted for all high collinearity events in Figure 29. However, there were insufficient events to provide a statistically meaningful fit. Figure 30 shows a collinearity-squared plot for all $K_L \rightarrow \mu\bar{\mu}$ candidates passing the $K_L \rightarrow \mu\bar{\mu}$ quality and track cuts, and lying within the mass window, but excluding particle identification. This provided sufficient high collinearity events for the fit. A straight line fit was made to those events with $2. \times 10^{-6} < \theta_c^2 < 4. \times 10^{-6}$ mrad². This fit was projected back into the signal region. The number of background events was then calculated by taking the area under the projected fit, resulting in 809.18 events. The number of events in a region identical in size to the signal region, but displaced in θ_c^2 by $+2.0 \times 10^{-6}$ mrad², was then determined in both Figure 29 and Figure 30 (14 and 610.28 respectively). The background fit was then scaled by the ratio of the events in the displaced region to obtain 19 background events in the signal region. Subtracting these events from the signal results in $N_{\mu\mu} = 281$.

$K_L \rightarrow \pi^\pm \mu^\mp \nu$ Background

The peak in the mass plot below $0.489 \text{ GeV}/c^2$ resulted from the $K_L \rightarrow \pi^\pm \mu^\mp \nu$ decay mode in which the pion is misidentified as a muon. The mass spectrum which results from calculating the invariant mass of these events assuming a muon mass for the pion, ends at $0.4893 \text{ GeV}/c^2$, or $8.4 \text{ MeV}/c^2$ below the kaon mass, and well outside the mass resolution of the experiment. However, errors in the measurement of the individual track momenta can result in an invariant mass above the Dalitz endpoint.

Furthermore, the pion was subject to decay within the detector apparatus. Such decays which occurred upstream of the spectrometer would either have failed the vertex χ^2 (since the pion decay track would not point back to the original kaon decay vertex), or had high collinearity (since the undetected neutrino would have carried off some momentum resulting in a mismatch between the kaon momentum and the vector sum of the two detected particle momenta). Similarly, such decays within the spectrometer would have failed the track χ^2 cuts (since the track would have a kink at the point of decay resulting in a bad fit to the expected track from the original kaon decay product). However, decays downstream of the spectrometer but upstream of the muon filter would be virtually indistinguishable from $K_L \rightarrow \mu\bar{\mu}$ events (since any deviations from the expected track would be lost in the multiple scattering which occurs in the PBG and muon filter, and the MHO and MRG ID cuts were too loose to reject any but the most eccentric events).

Three possible methods were available to determine the background in the signal region. The first was to use Monte Carlo $K_L \rightarrow \pi^\pm \mu^\mp \nu$ events to calculate the background. Unfortunately, the standard Monte Carlo does not adequately simulate the mass resolution of the experiment, thus preventing the calculation of the probability of a $K_L \rightarrow \pi^\pm \mu^\mp \nu$ event having an invariant mass above the Dalitz limit. The second method was to fit the data points in the mass plot below $0.489 \text{ GeV}/c^2$ and extrapolate into the signal region. Low statistics and a lack of knowledge as to the proper distribution to use can lead to high uncertainties for this method.

The final method was to use the approach applicable to the $K_L \rightarrow \mu^\pm e^\mp$ decay mode from $K_L \rightarrow \pi^\pm e^\mp \nu$. In this case, the pion was also misidentified as a muon which leads to a similar background for the $K_L \rightarrow \mu^\pm e^\mp$. The lack of background events for within an identical signal region, leads to the conclusion that background from single misidentification was not a problem[45].

Cut Identification	Events Cut
Missing Crates	181
RUN 5377	89
Fail FT Fitting	0
Vertex $z < 9.75$	7934
Vertex $ x/z > 0.0027$	865
Vertex $ y/z > 0.0100$	811
Track χ^2	18196
Vertex χ^2	3461
P_{front}/P_{back} match	1841
Track momentum $< 1.5 \text{ GeV}/c$	2115
Same charge events	0
No 50 Hertz Flag	2
Fail Aperture Cuts	2435

Table 6: Results of Quality and Track cuts on Minimum Bias Sample

6.3 $K_L \rightarrow \pi\bar{\pi}$ Normalization Sample

After event stripping, there were 258,553 minimum bias events from which to determine the number of $K_L \rightarrow \pi\bar{\pi}$ events. As with the $K_L \rightarrow \mu\bar{\mu}$ sample, this required a series of cuts based on track quantities. However, no particle identification cuts were performed on this sample. Finally, the $K_L \rightarrow \pi\bar{\pi}$ sample contained background events from semileptonic decays which were subtracted to obtain $N_{\pi\pi}$.

6.3.1 Event Selection Cuts

The normalization sample was taken from minimum bias events, weighted over the entire run. By definition, the minimum bias sample did not contain L3 decision cuts. Therefore, the first step in determining the number of $K_L \rightarrow \pi\bar{\pi}$ events was to calculate and impose the L3 mass and collinearity cuts. This eliminated 103,654 $K_L \rightarrow \pi\bar{\pi}$ candidates.

Next, the identical cuts described in Sections 6.2.1–6.2.2 were imposed on the minimum bias sample. Figure 31, Figure 32, Figure 33 show the distributions for $K_L \rightarrow \pi\bar{\pi}$ candidates for vertex χ^2 , track χ^2 and front-back momentum match, respectively. Again notice the discrepancy between Monte Carlo and data in the track χ^2 plots which lead to its looseness. Table 6 gives the results of these cuts.

One additional track cut was imposed on $K_L \rightarrow \pi\bar{\pi}$ events to eliminate contamination of the $K_L \rightarrow \pi\bar{\pi}$ sample by the decay $\Lambda^0 \rightarrow p^+\pi^-$, where the proton is misidentified as a pion.

This contamination was easily recognizable in the data sample [46], since the momentum asymmetry $(p_p - p_\pi)/(p_p + p_\pi)$ was greater than 0.66, all particles were outbends, and the vertex z was less than 11 m. It was equally likely to affect the $K_L \rightarrow \pi\bar{\pi}$ signal and the $K_L \rightarrow \pi\bar{\pi}$ background. Thus, cutting the Λ contamination was not strictly necessary, but was nevertheless imposed due to the ease of identification. Any event for which the momentum asymmetry was greater than 0.66 and for which the reconstructed mass (as $p\pi$) minus the Λ mass was less than $6 \text{ MeV}/c^2$ was cut. This eliminated 38 $K_L \rightarrow \pi\bar{\pi}$ candidates.

6.3.2 Number of $K_L \rightarrow \pi\bar{\pi}$

Figure 34 shows the mass distribution for all $K_L \rightarrow \pi\bar{\pi}$ events with $\theta_c^2 \leq 2.0 \text{ mrad}^2$. Using the same signal region defined for $N_{\mu\mu}$ produces 19,934 $K_L \rightarrow \pi\bar{\pi}$ normalization events. (Note: there is an additional correction included in this number, see Section 6.4.4.)

The figure shows a peak corresponding to the actual $K_L \rightarrow \pi\bar{\pi}$ events superimposed on background from $K_L \rightarrow \pi^\pm \mu^\mp \nu$ and $K_L \rightarrow \pi^\pm e^\mp \nu$ events. In order to determine $N_{\pi\pi}$, the background from the semileptonic decays underneath the $K_L \rightarrow \pi\bar{\pi}$ peak must be estimated. To accomplish this, the standard Monte Carlo routines were run forcing all kaons into the $K_L \rightarrow \pi^\pm \mu^\mp \nu$ and $K_L \rightarrow \pi^\pm e^\mp \nu$ decay modes. The resultant distribution was then scaled such that the number of Monte Carlo events outside the $K_L \rightarrow \pi\bar{\pi}$ region (*i. e.* with invariant mass as $K_L \rightarrow \pi\bar{\pi}$ in the range 475–488 and 508–525 MeV/c^2) was equal to the number of data events in the same region. This is shown in Figure 34 as the dashed line. The signal mass cut was then imposed on the Monte Carlo events to determine the background contamination of $K_L \rightarrow \pi\bar{\pi}$. The result was 4166 background events giving $N_{\pi\pi} = 15,768 \pm 155$, where the statistical uncertainty includes the contributions from both data and Monte Carlo.

6.4 Corrections Factors

A series of correction factors to Equation 32 arises from the variations between the decay modes $K_L \rightarrow \mu\bar{\mu}$ and $K_L \rightarrow \pi\bar{\pi}$. The corrections can be classified into two types. The first type was caused by fundamental differences in the interactions of pions and muons, such as the strong interaction of pions. The second type was caused by the different reactions of the experimental apparatus, in both hardware and software, to different particle types.

6.4.1 Level 1 Efficiency

The Level 1 trigger performed a fast and crude particle identification on events to obtain $K_L \rightarrow \mu\bar{\mu}$ candidate events (see Section 4.2). Inefficiencies in the MHO and MRG could have caused L1 to fail to identify an actual $K_L \rightarrow \mu\bar{\mu}$ event within the detectors. Additionally, inefficiency or mistiming within the L1 PLUs could cause two-muon events to fail the L1 decision as $K_L \rightarrow \mu\bar{\mu}$. ($K_L \rightarrow \pi\bar{\pi}$ events had no L1 particle ID, and hence were not affected.) The L1 efficiency ε_{L1} was calculated in the following manner. Track-counter association for both the MHO and MRG was applied to the minimum bias sample to obtain a sample of events for which two tracks were found, each of which satisfied the muon identification cuts in both detectors. The Level 1 trigger word was then examined to see if the $\mu\mu$ bit was set (recall that L1 was performed on minimum bias events, but no L1 decision was made). A total of 4716 events were found which satisfied the muon ID cuts, of which 4642 had the $\mu\mu$ bit set, for an efficiency of $98.4 \pm 0.2\%$.

6.4.2 Level 3 Efficiency

Both $K_L \rightarrow \mu\bar{\mu}$ and $K_L \rightarrow \pi\bar{\pi}$ events were cut based on the Level 3 decision. Therefore, both need to be corrected by the L3 efficiency. The ratio of these corrections (which is the quantity of importance for Equation 33) is not necessarily unity, since the L3 efficiency was dependent on kaon momentum and the decay opening angle, for which the distributions differ for each decay mode.

For $K_L \rightarrow \pi\bar{\pi}$ events, it was possible to determine the L3 efficiency with minimum bias events on which all cuts except L3 were performed to obtain a sample of $K_L \rightarrow \pi\bar{\pi}$ events. These events were then subjected to the L3 code to determine $\varepsilon_{L3\pi\pi}$. Unfortunately, this procedure could not be used for $K_L \rightarrow \mu\bar{\mu}$ events. Instead, $\varepsilon_{L3\pi\pi}$ was calculated as a function of kaon momentum and opening angle. $K_L \rightarrow \mu\bar{\mu}$ events were then generated using the Monte Carlo routines to give the distributions of $K_L \rightarrow \mu\bar{\mu}$ by opening angle and kaon momentum. By combining the $\varepsilon_{L3\pi\pi}$ functions with the $K_L \rightarrow \mu\bar{\mu}$ distributions, $\varepsilon_{L3\mu\mu}$ was obtained. For $K_L \rightarrow \pi\bar{\pi}$, $\varepsilon_{L3\pi\pi}$ was $0.641 \pm 0.0027 \pm 0.0047$ and for $K_L \rightarrow \mu\bar{\mu}$, $\varepsilon_{L3\mu\mu}$ was $0.640 \pm 0.0029 \pm 0.0045$, where the uncertainties are the systematic uncertainty from the minimum bias sample and the statistical uncertainty of the Monte Carlo routines respectively.

6.4.3 Hadronic Interactions

Since pions were susceptible to strong interactions within the spectrometer or the particle detectors, it was possible that some $K_L \rightarrow \pi\bar{\pi}$ events would not be detected. Such events could be missed in one of three ways. First, a pion may inelastically or elastically scatter in the spectrometer, and thus never reach the TSCs, resulting in no L1 trigger. Second, a pion may undergo such interactions within the upstream TSCs or the CER and fail to fire the downstream TSCs, also resulting in no L1 trigger. Finally, a pion may undergo such interactions within the TSCs or the CER, where the original pion, or daughter particles may still fire the TSC counters, resulting in a L1 trigger, yet fail offline in pattern recognition, since the TSC hits may not point back to the hits within the spectrometer.

The standard offline Monte Carlo did not take into account strong interactions for hadrons. To estimate the $K_L \rightarrow \pi\bar{\pi}$ losses required the use of a different Monte Carlo package. The E791 apparatus was modeled using the CERN GEANT Monte Carlo package. (NB: In this case, the full GEANT package was used. This should not be confused with the offline Monte Carlo extension discussed in Appendix B, which utilizes only part of the GEANT package.) The standard offline Monte Carlo was used to produce $K_L \rightarrow \pi\bar{\pi}$ events weighted by the proper kaon momentum distribution. These events were then used as input to the GEANT E791 model. Any event which GEANT determined underwent a hadronic interaction in either pion track prior to the downstream TSC bank was assumed to be lost. The results of this study showed that $3.7 \pm 0.4\%$ of the $K_L \rightarrow \pi\bar{\pi}$ events were lost, for a ϵ_{INT} of 0.963 ± 0.004 where the uncertainty results from the Monte Carlo statistics.

6.4.4 K_S Contamination

Possibly the worst potential source of contamination in the normalization sample arises from the $K_S \rightarrow \pi\bar{\pi}$ decay mode. Fifty percent of the K^0 produced at the target are K_S , and given that the mass difference between K_L and K_S is several orders of magnitude less than E791's mass resolution, the decays $K_L \rightarrow \pi\bar{\pi}$ and $K_S \rightarrow \pi\bar{\pi}$ are kinematically indistinguishable. However, the average time of flight from the target to the decay volume is several K_S lifetimes, with the result that most of the K_S contamination is eliminated by the decay vertex z cut. Unfortunately, the high probability of $K_S \rightarrow \pi\bar{\pi}$ (69% [13]) insures that most of the high momentum K_S which do reach the accepted region of the decay volume will contaminate the normalization sample. Additional contamination arises from

K_S and K_L interference (K_I).

To correct for K_S and K_I requires the relative fractions of K_S and K_I to K_L in the neutral kaon production, within the decay volume. This can be calculated from the square of the sum of the K_L and K_S amplitudes [47]:

$$|\langle \pi^+ \pi^- | H | K^0(t) \rangle|^2 \sim e^{-t/\tau_s} + |\eta_{+-}|^2 e^{-t/\tau_l} + 2|\eta_{+-}|^2 e^{-t/\tau_s + \tau_l} \cos((m_{K_L} - m_{K_S})/\hbar - \phi_{+-}) \quad (34)$$

using the following values [13]:

$$\begin{aligned} |\eta_{+-}| &= 2.266 \times 10^{-3} \\ \phi_{+-} &= 44.6^\circ \\ \tau_s &= 0.8992 \times 10^{-10} \text{ s} \\ \tau_l &= 5.18 \times 10^{-8} \text{ s} \\ (m_{K_L} - m_{K_S})/\hbar &= 0.5349 \times 10^{-10} \text{ s}^{-1}. \end{aligned}$$

Since the resulting relative fractions are dependent both on the kaon momentum and its z decay position, K_S and K_I had to be calculated over the kaon decay spectrum. Two methods were available to accomplish this. The first method [47] involved dividing p and z into bins and calculating the ratio $(K_S + K_I)/K_L$ from Equation 34 for each bin, integrating over z but using the average p in each case. The standard Monte Carlo was then used to determine the K_L population for each bin. These two distributions were then combined to obtain the overall reduction for the normalization sample from K_S and K_I . Studies using this method show that K_S and K_I account for 2% of the normalization sample [48].

An alternate method, which is used in this paper, is to weight each $K_L \rightarrow \pi\pi$ data event by the K_L probability. In this case, Equation 34 is evaluated for each individual event in the normalization sample, using the exact z and p for the event to determine $P(K_L)$, and defining the normalization sample as the sum of the weighted events. This avoids much of the systematic errors incurred in the first method by the integration of Equation 34 over z , and by the large shifts in the effects of K_I in certain z and p bins with low K_L populations. This method does not result in a direct calculation of $(K_S + K_I)/K_L$ which can be compared with the first method. However, it is possible to obtain $(K_S + K_I)/K_L$ by comparing the total number of $K_L \rightarrow \pi\pi$ events weighted by $P(K_L)$ to the number of $K_L \rightarrow \pi\pi$ without weighting. With $P(K_L)$, the total number of $K_L \rightarrow \pi\pi$ events is 19,934, without $P(K_L)$

it is 20,278. The difference corresponds to the K_S and K_I contributions, resulting in a $(K_S + K_I)/K_L$ ratio of 1.7%, in good agreement with the first method.

6.4.5 Particle ID Efficiencies

The final correction $\epsilon_{\mu\mu}$ was based on the particle identification requirements for $K_L \rightarrow \mu\bar{\mu}$. Muons from $K_L \rightarrow \mu\bar{\mu}$ were required to pass the particle identification cuts for the MHO and MRG (see Section 5.4.1). Since these detectors were not 100% efficient, good $K_L \rightarrow \mu\bar{\mu}$ events could be lost through failure to detect one or both muon tracks. No equivalent losses would occur in the $K_L \rightarrow \pi\bar{\pi}$ sample, as no particle identification was imposed on the pion tracks. The correction factor $\epsilon_{\mu\mu}$ was the product of the individual efficiencies for detecting $K_L \rightarrow \mu\bar{\mu}$ events for the MHO and the MRG, ϵ_{MHO} and ϵ_{MRG} respectively.

The first step in calculating $\epsilon_{\mu\mu}$ was to determine the efficiency for detecting an individual muon track within the detectors, treating the MHO and MRG separately. The efficiencies were measured using muons from the $K_L \rightarrow \pi^\pm \mu^\mp \nu$ decay mode. Events were vetoed if the CER, PBG, MHO or MRG had any track-associated hits in the pion track (exception: high momentum tracks were permitted to fire the CER if above the pion Čerenkov threshold). Events were also vetoed if either the CER or PBG had track associated hits in the muon track (again excepting tracks with momentum above the muon Čerenkov threshold). Finally, for the MHO efficiency, the muon track was required to pass the MRG ID cuts and vice versa for the MRG.

The resulting MHO and MRG efficiencies for detecting individual muon tracks from $K_L \rightarrow \pi^\pm \mu^\mp \nu$ could not be used directly in ϵ_{MHO} or ϵ_{MRG} . The efficiencies for both detectors were dependent on the momentum of the incident muon. And while muons are identical whether originating from a $K_L \rightarrow \pi^\pm \mu^\mp \nu$ or $K_L \rightarrow \mu\bar{\mu}$ event, the overall detector efficiency depended on the momentum spectrum of the incident muons, which differed significantly between $K_L \rightarrow \pi^\pm \mu^\mp \nu$ and $K_L \rightarrow \mu\bar{\mu}$. Additionally, the MHO efficiency was found to be dependent on the x position of the incident muon, and the x hit distribution also differed for muons from $K_L \rightarrow \pi^\pm \mu^\mp \nu$ and $K_L \rightarrow \mu\bar{\mu}$.

In order to determine ϵ_{MHO} , the efficiency for detecting an individual muon tracked was measured as a function of both momentum and x position. The Monte Carlo routines were then used to produce $K_L \rightarrow \mu\bar{\mu}$ events with the proper p and x distributions. ϵ_{MHO} was then the average of the individual muon track detection efficiencies (binned by x and p for both tracks in the $K_L \rightarrow \mu\bar{\mu}$ events), weighted by the number of $K_L \rightarrow \mu\bar{\mu}$ in a given bin.

Similarly, ϵ_{MRG} was determined, but in this case, binned only by p .

Using this method, ϵ_{MHO} was determined to be 0.951 ± 0.003 , and ϵ_{MRG} was determined to be $0.980 \pm .003$ resulting in $\epsilon_{\mu\mu}$ of 0.931 ± 0.004 . An alternate method of including the MHO and MRG particle ID efficiencies will be discussed in Section 6.5.2.

6.5 Geometric Acceptance

Only a small fraction of K_L decays could be detected by the E791 apparatus. The two main restrictions on the kinematics of accepted K_L events were the decay vertex position, which was required to be within the decay volume, and the opening angle of the decay, which had to be sufficiently small to send the decay products into the E791 spectrometer but not so small as to pass between the two arms of the spectrometer. This window of detection was referred to as the *geometric acceptance*. Additionally, the inefficiencies of the wires within the drift chambers were also taken into account within the geometric acceptance. If the distributions in opening angle, decay position, and drift chamber hit positions were the same for the various decay modes, the geometric acceptance of the experiment would be irrelevant as its effects would be identical for all decay modes and thus cancel out in Equation 33. However, the kinematics for the decay modes differ significantly. Thus the ratio of the geometric acceptances must be included in any calculation of the branching fraction for $K_L \rightarrow \mu\bar{\mu}$.

In the two sections which follow, two methods of calculating the geometric acceptance will be discussed.

6.5.1 Standard Monte Carlo

The first method of calculation dealt only with the upstream portion of the E791 apparatus, *i. e.* from the target through the spectrometer, in detail. For $K_L \rightarrow \mu\bar{\mu}$, particle identification in the MHO and MRG were not included in the acceptance but in a separate correction factor (see Section 6.4.5).

Neutral kaons within the momentum region of 3–20 GeV/ c were produced at the target using the parameterization of Skubic *et al.* [49]. This parameterization was modified to produce Monte Carlo kaon momentum and z decay position distributions which agreed with the data distributions derived from semileptonic events. Figure 35 and Figure 36 show the agreement between the reconstructed kaon momentum and the kaon decay vertex z ,

respectively, for Monte Carlo and data $K_L \rightarrow \pi\bar{\pi}$ events.

The kaon decays into daughter particles were simulated within the decay volume and the daughters were then tracked through the spectrometer. The tracking routines utilized a fourth order Runge-Kutta integration to simulate the effects of the magnetic fields. Multiple Coulomb scattering and electron bremsstrahlung were also simulated, along with the decays in flight by the daughter particles. Energy loss due to ionization was not modeled under the assumption that it was not significant in the low density media in the spectrometer. This assumption is invalid downstream of the last TSC bank; hence, the separation of muon particle identification into another correction factor. Additionally, the drift chamber hit simulations accounted for the effects of dead wires within the DC modules.

Monte Carlo $K_L \rightarrow \pi\bar{\pi}$ events were then generated and subjected to the identical analysis process used for the normalization sample. Monte Carlo $K_L \rightarrow \mu\bar{\mu}$ events were also subjected to the analysis used for $K_L \rightarrow \mu\bar{\mu}$ candidates in the data, excepting particle identification. The absolute acceptances were then calculated by comparing the final number of $K_L \rightarrow \pi\bar{\pi}$ and $K_L \rightarrow \mu\bar{\mu}$ events which survived all cuts to the total generated. The absolute acceptance for $K_L \rightarrow \mu\bar{\mu}$ ($A_{\mu\mu}$) calculated under this method is 0.02721 ± 0.00009 . The absolute acceptance for $K_L \rightarrow \pi\bar{\pi}$ ($A_{\pi\pi}$) is 0.03207 ± 0.00011 .

6.5.2 Extended Monte Carlo

The second method used the identical processes as in the first method up to the downstream TSC bank. From there, particles were tracked into the downstream detectors utilizing the GEANT extension described in Appendix B. For $K_L \rightarrow \pi\bar{\pi}$ events, this would have no effect as the particle ID detectors played no role in determining the normalization sample. (As a test, the extended code was run on the same Monte Carlo $K_L \rightarrow \pi\bar{\pi}$ events used above, and using the same random number seeds, giving identical results in the acceptance, as expected.) For $K_L \rightarrow \mu\bar{\mu}$ events, the extension allowed the incorporation of the MHO and MRG efficiencies directly into the acceptance, rather than as a separate correction factor. Particle tracking information from the standard Monte Carlo at the downstream TSC bank was passed to the modified GEANT extension. These particles were then stepped through a model of the PBG, iron filter, MHO and MRG, with all relevant physical processes enabled (the most important being multiple Coulomb scattering and ionization energy losses, utilizing the GEANT formulas which are valid in high density materials). This method checks certain inherent assumptions used in determining the muon identification efficiency

for the MHO, and employs an alternate method of incorporating MRG inefficiencies.

For muons, the MHO and MRG responses were then simulated. In the case of the MHO, this was simply a generalized simulation almost identical to that used in Section 6.4.5. The efficiency of the MHO was binned by the momentum measured upstream, and by the x counter hit (identical to the x binning in Section 6.4.5). For each muon passing through the MHO, a random number (0–1.) was generated and compared to the binned efficiency to determine whether or not the MHO successfully identified the muon. The only significant differences between this method and that employed in ϵ_{MHO} are that the x position used here incorporates multiple scattering and the possibility that a muon of momentum just slightly greater than 1.5 GeV/c might not actually penetrate the iron filter. (Remember that muons less than 1.5 GeV/c are cut from the analysis). By contrast, ϵ_{MHO} uses the x position obtained by straight line projection of the track information at the downstream TSC bank and assumes all muons with momentum greater than 1.5 GeV/c reach the MHO.

The simulation of the MRG used here is substantially different from that used in Section 6.4.5. Recall that in ϵ_{MRG} , the efficiency of the MRG as a whole was calculated and binned by momentum. Here, the efficiency of each module group (*i. e.* all four x and y modules in a given MRG gap) was measured individually, using muons from the semileptonic sample. Monte Carlo muons were then tracked through the MRG, and checked at each gap to see if that gap was triggered. The MRG track counter association code was then run on these simulated hits to find the muon tracks. Finally, the MRG actual minus expected gap cut was imposed, just as with the actual data events.

The absolute acceptance for $K_L \rightarrow \mu\bar{\mu}$ ($A'_{\mu\mu}$) calculated under this method is 0.02556 ± 0.00009 . As stated above, the absolute acceptance for $K_L \rightarrow \pi\bar{\pi}$ ($A'_{\pi\pi}$) is unchanged. A direct comparison of the acceptance ratios determined in this and the preceding section is not valid. Instead, one must compare the acceptance ratio calculated in the preceding section combined with the muon identification efficiency calculated in Section 6.4.5 to the acceptance ratio calculated in this section. The result of such a comparison is:

$$\begin{aligned} A_{\pi\pi}/A_{\mu\mu}\epsilon_{\mu\mu} &= 1.266 \pm 0.008 \\ A'_{\pi\pi}/A'_{\mu\mu} &= 1.255 \pm 0.006 \end{aligned}$$

in good agreement with each other.

Quantity	$K_L \rightarrow \pi\bar{\pi}$		$K_L \rightarrow \mu\bar{\mu}$	
	FT value	QT value	FT value	QT value
Total events	258553	258553	244716	244716
Missing Crates	181	181	106	106
R5377	89	89	75	75
L3 ($K_L \rightarrow \pi\bar{\pi}$ only)	103654	103654	0	0
$ \text{TIMEPZ} > 4$ ns	1210	1210	25	24
Track fitting	0	1765	1	11397
Vertex z	7934	7806	19962	18741
Vertex x/z	865	825	9500	8035
Vertex y/z	811	811	1409	1296
Track χ^2	18196	11344	80216	61657
QT Track χ^2	0	7172	0	14687
Vertex χ^2	3461	3340	9990	9285
$p_f p_b$ match	1841	644	5935	2506
Track $p < 1.5$ GeV/c	2115	2038	650	609
Like-sign events	0	0	18	22
Lambda event	38	34	0	0
Bad 50 Hz Flag	2	2	5	4
Aperture Cuts	2435	2552	3468	3549
MHO cut ($K_L \rightarrow \mu\bar{\mu}$ only)	0	0	103159	102699
MRG cut ($K_L \rightarrow \mu\bar{\mu}$ only)	0	0	4546	4460
Events remaining	115721	115086	5651	5564
Events in signal region	19934	19725	300	299
Background events	4166	4122	19	22.00

Table 7: Summary of Analysis results for FT and QT fitting packages.

6.6 $K_L \rightarrow \mu\bar{\mu}$ Branching Fraction

The results of the analysis are summarized in Table 7. For convenience Equation 33 is repeated here:

$$B(K_L \rightarrow \mu\bar{\mu}) = B(K_L \rightarrow \pi\bar{\pi}) \frac{N_{\mu\mu} A_{\pi\pi} \epsilon_{\text{INT}} \epsilon_{L3\pi\pi}}{\text{PRESCALE} * N_{\pi\pi} A_{\mu\mu} \epsilon_{\mu\mu} \epsilon_{L1} \epsilon_{L3\mu\mu}}$$

(Recall that the ϵ_{π_s} is folded into $N_{\pi\pi}$.) Incorporating the FT values from Table 7, one obtains the following result:

$$\begin{aligned} N_{\pi\pi} &= 15,768 \pm 155 \\ N_{\mu\mu} &= 281 \pm 19 \\ \text{PRESCALE} &= 6000 \end{aligned}$$

$$\begin{aligned}
A_{\pi\pi}/A_{\mu\mu} &= 1.179 \pm 0.006 \\
\epsilon_{\text{INT}} &= 0.963 \pm 0.004 \\
\epsilon_{L3\pi\pi} &= 0.641 \pm 0.0027 \\
\epsilon_{L3\mu\mu} &= 0.640 \pm 0.0029 \\
\epsilon_{L1} &= 0.984 \pm 0.002 \\
\epsilon_{\mu\mu} &= 0.931 \pm 0.004 \\
B(K_L \rightarrow \pi\bar{\pi}) &= (2.04 \pm 0.04) \times 10^{-3}
\end{aligned}$$

$$B(K_L \rightarrow \mu\bar{\mu}) = (7.6 \pm 0.5) \times 10^{-9}$$

where the uncertainty is statistical only. Using QT values from Table 7, one obtains $B(K_L \rightarrow \mu\bar{\mu}) = 7.5 \times 10^{-9}$. If the alternate geometric acceptance $A'_{\pi\pi}/A'_{\mu\mu}$ is substituted for $A_{\pi\pi}/A_{\mu\mu}\epsilon_{\mu\mu}$ in the FT calculation, the one again obtains 7.5×10^{-9} , still in excellent agreement with the standard FT results.

The final step was to estimate the systematic uncertainties in $B(K_L \rightarrow \mu\bar{\mu})$. The systematic uncertainties fell into two categories. The first were those associated with the statistical uncertainties of all factors in Equation 33, except $N_{\mu\mu}$, and are listed in the top section of Table 8. The second category comprised the uncertainties which arose from the cuts used to determine $N_{\mu\mu}$ and $N_{\pi\pi}$, and require more detailed examination.

One way to estimate the uncertainty in $B(K_L \rightarrow \mu\bar{\mu})$ from any given cut was to vary that cut, while maintaining all other cuts at their standard values. $B(K_L \rightarrow \mu\bar{\mu})$ was then recalculated as a function of the varied cut value. Since the only factors in Equation 33 which are related to event selection cuts are $N_{\pi\pi}$, $N_{\mu\mu}$ and $A_{\pi\pi}/A_{\mu\mu}$, the actual quantity plotted for these studies was $(N_{\mu\mu}/N_{\pi\pi}) \times (A_{\pi\pi}/A_{\mu\mu})$ (referred to as $R(\mu, \pi)$). For the standard cuts, $R(\mu, \pi)$ equals 0.0210 (referred to as the nominal value).

Figure 37 shows the plot $R(\mu, \pi)$ versus mass window cut. The standard mass cut required the reconstructed K_L mass for $\pi\pi$ and $\mu\mu$ events be within $0.006 \text{ GeV}/c^2$ of the actual K_L mass. For Figure 37, this mass window was varied from zero (no signal) to $0.010 \text{ GeV}/c^2$ (well into the background). $R(\mu, \pi)$ shows substantial variation from its nominal value only for the very tight window cuts (0.004 and less) and for very loose cuts (roughly 0.008 and above). These cuts clearly are not reasonable. In the first case, the tight cuts are eliminating significant numbers of $K_L \rightarrow \pi\bar{\pi}$ and $K_L \rightarrow \mu\bar{\mu}$ events, while in

Quantity	Uncertainty (%)
$N_{\pi\pi}$	0.98
$A_{\pi\pi}/A_{\mu\mu}$	0.5
ϵ_{INT}	0.4
$\epsilon_{L3\pi\pi}$	0.4
$\epsilon_{L3\mu\mu}$	0.5
ϵ_{L1}	0.2
$\epsilon_{\mu\mu}$	0.4
$B(K_L \rightarrow \pi\bar{\pi})$	2.0
Mass window	< 1.
θ_c^2	< 2.
Vertex z	< 1.
Track χ^2	< 1.
P_f/P_b	< 1.
Aperature cuts	< 1.
MHO ID	2.0
MRG ID	4.0

Table 8: Systematic uncertainties in $B(K_L \rightarrow \mu\bar{\mu})$.

the second case, the $K_L \rightarrow \pi\bar{\pi}$ and $K_L \rightarrow \mu\bar{\mu}$ signals are being swamped by background. In either case, the validity of the background subtractions must be questioned. However, for reasonable values for the mass window cut, $R(\mu, \pi)$ varies by less than one percent. Figure 38, Figure 39, Figure 40 and Figure 41 show the results for similar studies for the θ_c^2 , $p_{\text{front}}-p_{\text{back}}$ match, vertex χ^2 and track χ^2 cuts respectively. In these cases, $R(\mu, \pi)$ shows substantial variations only when these cuts are too tight. Figure 42 shows the results for the vertex z cut. Here, the variations in $R(\mu, \pi)$ at low z show the effects of $K_S \rightarrow \pi\bar{\pi}$ contamination in the normalization sample.

The two particle ID cuts only affect $N_{\mu\mu}$. Figure 43 shows $N_{\mu\mu}$ for various MHO confidence level cuts, ranging from 0.00005 to 1.0. $N_{\mu\mu}$ is nearly constant over a wide range of values. The MRG cut cannot be loosened by more than one gap (*i. e.* to -4.5), due to the pion misidentification problems discussed in Section 5.4.1. Varying the MRG cut from -1.5 to -4.5 results in approximately a 4% shift in $N_{\mu\mu}$.

The lower half of Table 8 summarizes the level of uncertainty for the event selection cut. Summing all uncertainties in Table 8 (in quadrature) results in a systematic uncertainty of 5.9% for $B(K_L \rightarrow \mu\bar{\mu})$.

A final test of the measurement of $B(K_L \rightarrow \mu\bar{\mu})$ is to calculate $R(\mu, \pi)$ for various

subsections of the data. This is more a qualitative than a quantitative test as the correction factors in Equation 33 are averaged over the data sets. Figure 44 shows the results for several such subsections. The first divides the $K_L \rightarrow \pi\bar{\pi}$ and $K_L \rightarrow \mu\bar{\mu}$ samples by the change in direction of the trajectory of the daughter particles in the first magnet, the second by run number, the third by reconstructed K_L momentum and the fourth by K_L decay vertex. Only the run number plot show any significant disagreement. For RUNS 5000–5499, the branching fraction is significantly lower than in the other run groups. Examination of these runs reveals a shortfall in the number of $K_L \rightarrow \mu\bar{\mu}$ events. Careful examination of both the MHO and MRG efficiencies within the given range of runs show no degradation in muon detection efficiency. This variation is probably statistical in nature.

6.7 Conclusions

The final measurement of the branching fraction of $K_L \rightarrow \mu\bar{\mu}$ obtained in this work is

$$B(K_L \rightarrow \mu\bar{\mu}) = (7.6 \pm 0.5 \pm 0.4) \times 10^{-9}$$

where the first uncertainty is statistical and the second is systematic. This value is within 10% of the value calculated from the unitarity limit (Equation 4). Given the uncertainties inherent in the unitarity limit calculation, this value is in very good agreement.

While the E791 apparatus was clearly well designed, and performed well, it was pushed to the limits of its sensitivity. This was more readily apparant in the $K_L \rightarrow \mu^\pm e^\mp$ search than in $K_L \rightarrow \mu\bar{\mu}$ measurement[45]. E791 was both rate and background-limited. The high particle flux in the detectors, particularly in the drift chambers, limited the experiment in two ways. First, there was a maximum beam intensity beyond which the drift chambers ceased to function (*i. e.* they began to draw such high currents that the high voltage supplies tripped off to protect the chamber wires). Second, backgrounds in the detectors from the high flux made event reconstruction, particularly in the higher level triggers and in pattern recognition, more difficult.

A modified version of E791 has been proposed and accepted at BNL which addresses these problems so as to obtain higher sensitivity[50]. Its primary modification is the inclusion of a neutral beam plug within the first magnet. It is hoped that by stopping the neutral beam upstream of the majority of particle detectors, the rates in those detectors will significantly lowered.

Appendix A

The Muon Rangefinder

A.1 Overview

As discussed briefly in Section 3.9, the muon rangefinder (MRG) was the second particle identification system for muons in E791. The basic principle behind its operation is that only muons are capable of penetrating the iron filter upstream of the MHO in significant numbers. All hadrons interact strongly in the iron, losing energy rapidly by elastic processes, or creating secondary particles which lose energy rapidly in turn. Neutrinos are notoriously difficult to detect. This leaves only the charged leptons; the electron, muon and tau. The latter is too short-lived to leave a track, and the former loses energy in the iron much more rapidly than a muon. In the sections which follow, the construction and performance of the MRG shall be discussed in detail. Responsibility for the construction and maintenance of the MRG was shared between teams from the College of William & Mary and Los Alamos National Laboratory.

A.2 Construction

The MRG was constructed from three primary components. The first was a degrader material in which muons gradually lost their energy. Actual detection of particles traversing the MRG was provided by planes of proportional tube counters spaced throughout the marble, hereafter referred to as instrumented planes. Information from the planes was recorded *via* a three-stage readout system.

A.2.1 Marble

The bulk of the MRG resided within the degrader. The choice of degrader, and the design of the layout was primarily driven by requirements necessary for a measurement of muon polarization (see Section A.5). The most important point was that the degrader not depolarize muons traversing it. Two materials which are non-depolarizing are marble and aluminum. Marble had two advantages over aluminum. The first is that aluminum has a 0.23 barn cross-section for thermal neutron capture, which results in a 7 MeV γ , followed by a nuclear decay into a β^- and a 1.7 MeV γ (with a lifetime of 144 seconds). This had the potential for causing high singles rates in the proportional tube counters. The second advantage of marble was that at the time of procurement, marble was significantly less costly than aluminum.

The layout of the degrader in x, y and z was driven by two factors. In x and y , the slabs of degrader had to be sufficiently large to cover the geometric acceptance of the drift chambers, projected from the decay volume back through the MRG, and with sufficient additional coverage to reduce the number of muons lost out the sides by multiple scattering. In z , the requirements for polarization were again critical. The slabs of degrader had to be of sufficient total thickness to optimize the number of muons stopped within the space available for the MRG. At the same time, the individual slabs had to be sufficiently thin enough to allow a positron from a $\mu^+ \rightarrow e^+ \nu \bar{\nu}$ decay to escape the slab in which muon decay occurred, and thus to be tracked. The final design was based on Monte Carlo simulations of these factors.

The MRG was constructed in two arms symmetrically opposite in x across the neutral beam (see Figure 15), and centered in y on the beam center. The design requirements of the previous paragraph resulted in slabs $2.25 \times 3.05 \times 0.0762$ m in dimension. Each arm contained 100 slabs with 5.08 cm gaps between each slab for two instrumented planes. One-hundred-fifty (150) of the 200 slabs necessary for the MRG were constructed from four smaller rectangular blocks of Carrara marble, bonded with 3M 2216 B/A adhesive. For additional strength, a steel band was fastened to the outer edge of each marble slab. The remaining spaces in the MRG were filled with somewhat larger (in x and y) plates of aluminum, provided by BNL. The aluminum slabs were confined to the rear of the MRG, where neutron capture posed less of a problem due to the distance between instrumented gaps. For the same reason, the slab immediately before and after each instrumented gap was always filled with marble.

The entire assembly was supported by an aluminum frame. The gap between each arm was filled with a Mylar bag containing helium, and running the entire length of the MRG. This significantly reduced singles rates resulting from scattering of the neutral beam into struts of the assembly frame, particularly in downstream planes.

A.2.2 Instrumented Planes

Particle detection in the MRG was performed by planes of proportional tubes. A proportional tube works by applying an electrical field to a gas. A charged particle passing through the gas will ionize gas molecules. The free electrons will drift toward the anode wire, further ionizing the gas and releasing additional electrons. The result is a pulse on the wire which can be read out.

The instrumented planes were produced in two varieties, the horizontal-measuring or x -planes, and the vertical-measuring or y -planes. The basic component of each plane was an eight-cell aluminum extrusion (x and y extrusions differed only in length). Figure 45 provides a cross-sectional view of a single extrusion. Each cell contains two wires, 1.06 cm apart, which provide the electric field within the cell. This reduces electron drift times, and allows the use of narrow time gates to reduce accidentals. The interior aluminum walls (*webbing*) are diagonal to decrease the possibility of particles traversing a plane through the webbing instead of the gas cells, and thus avoiding detection. (In the case of x -planes, this requires reverse orientations of the webbing in the beam left and beam right configurations, such that the webbing is vectored in the direction opposite to the typical muon vector in a given detector arm. Thus, looking downstream the webbing vectors in the left and right arms converge, while for a typical $K_L \rightarrow \mu\bar{\mu}$ event, the left and right muon vectors diverge.

The first stage of construction required testing and cleaning the extrusions. Any curvature within the extrusion could lead to serious problems in maintaining high voltage on the wires. For that reason, all extrusions were first tested for straightness against a standard extrusion which was itself tested against a precision level work table. Any extrusion which deviated from true by more than 0.005" was rejected. Since dirt, dust or complex hydrocarbons would have an adverse affect on the performance and lifetime of the proportional tube counters, each tube in an extrusion was cleaned using tightly fitting nylon blocks, wrapped in Kymwipes and soaked in methanol to remove dirt and oil left during the extrusion process. Dry nitrogen was then flushed through each cell to remove Kymwipe particles left behind, and the extrusions were sealed until ready to be wired.

In the second stage, each cell was strung with two 75 μm gold-plated tungsten wires. The wires were also cleaned with ethanol to remove oil and dirt. Simultaneously, they were inspected, both by eye and by touch for "kinks" which would distort the electric field, and also weaken the wires. The wires were held in place by stainless steel minitubes (inner diameter of 125 μm), which were in turn supported by plastic Noryl holders mounted in the Lexan endcaps. The Lexan endcaps also controlled the flow of gas through the extrusions. Each endcap connected two adjacent cells, with the endcaps at each end staggered by one cell to set up a serial flow through all eight cells. Input and output gas ports were located in the two outermost cells of the endcaps used for the electronics end of the extrusions. The endcaps were bonded to the extrusions with Bondmaster 666 epoxy, which also acted as a sealant. Next, the wires were held in place at the non-electronics end by crimping the stainless steel minitubes to half their original outer diameter. The wires were then placed under 500 grams tension and crimped at the electronics end. The depth of the crimp, the tension provided, and the technique used to apply the crimp, were all carefully tested prior to fullscale production. The tension of the wires was critical. Too high a tension could cause a wire to break, while too low a tension would allow the wire (at positive high voltage) to come too close to the grounded extrusion walls tripping the high voltage supply. Finally, the extrusions were sealed with Bondmaster at the junctions between each Noryl and the Lexan endcaps, and between the Noryl and the minitubes, and the non-electronics end minitubes were crimped shut and epoxyed to prevent gas leaks.

The third stage of the process was quality control. Each completed extrusion (or panel) was tested for crossed wires by measuring the resistance between the wires of a cell. Next, the tensions of the wires were measured using a magnetic induction technique[51]. The wire to be measured was driven into oscillation using an oscillating electric field. A 7 Kgauss magnetic field was applied to the center of the wire. The oscillations within the magnetic field induced a small voltage on the wire. If the wire is driven into resonance, this induced voltage becomes relatively large. By varying the drive frequency, and observing the out-of-phase voltage on an oscilloscope, it was possible to determine the fundamental frequency of the wire. (Actually, measuring the fundamental frequency with accuracy proved to be quite difficult. Instead, the drive frequency was varied until the wire reached a harmonic at which frequency could be measured accurately, and with ease.) The tension in the wire is related to its fundamental frequency by the following formula:

$$T = 4\mu L^2 \nu_0^2 \quad (35)$$

where μ is the linear mass density of the wire, L is its effective free length, and ν_0 is the fundamental frequency. All wires which did not have a tension within tolerances were restrung. Next, the panels were tested for particle detection efficiency, using cosmic rays. The panels to be tested were placed in a Faraday cage (necessary to reduce noise caused by a nearby radio station) between two scintillator planes which formed the particle trigger. Signals from the panels were readout using a standard amplifier card and a standard discriminator card (see Section A.2.3). A 50/50 argon-ethane gas mixture was flowed through the planes. The efficiency of the panels was then measured as a function of applied high voltage. The singles rate in each panel cell was measured using a Strontium-90 β source to reveal any defects on an individual cell basis. Finally, the high voltage was slowly increased until the power supply tripped. This served as a qualitative measure of the relative resistance of the panels to tripping under high particle fluxes.

After completion and testing, the panels were shipped from William & Mary to BNL. Upon arrival, the wire tensions were measured again, and compared to the previously measured values. No wires broke or lost a significant amount of tension during shipment.

Next, the panels were assembled into x and y planes. Each x (y) plane contained 12 (16) panels of the proper varieties (see Figure 46). The positions of individual panels within the planes were based on the results of the quality control analysis. Those panels with the best efficiency and highest trip voltages were assigned to the regions where the highest particle fluxes were expected, *i. e.* the x panels nearest the neutral beam, and the central y panels. The panels for a given plane were then bonded together using an anaerobic adhesive called Loctite Depend. Again, curvature in the planes could have caused serious high voltage problems. For that reason, the planes were constructed on a marble slab built for the MRG, but under the more stringent requirement that it be flat to within 250 μm . Next, PolyFlo polyethylene tubing (outer diameter 0.64 cm) was used to connect the input and exhaust gas ports of the extrusions in series. Since polyethylene did not readily bond to the Lexan endcaps, the ends of the PolyFlo tubes were threaded prior to being bonded to the endcaps (using Bondmaster 666). The panels within a plane were grouped in two independent sections for gas flow (see Figure 47). For y -planes, the panels were divided into an upper and lower group of eight panels, connected serially within each group, and with the group inputs located in the center of the planes. For x -planes, the panels were divided into one group of four panels (those which would be closest to the neutral beam) and one group of eight panels, again linked serially with the group input in the innermost panel.

The grouping scheme was dictated by concern for wire aging, which shall be discussed later in this section.

Next, 0.16 cm thick sheets of aluminum were attached to the planes, using Loctite for strength and a silver-based epoxy for electrical conductivity. All exterior joints between the sheets and the extrusions were then covered with copper tape (see Figure 47). These sheets served three purposes. The first was to provide latitudinal structural strength to the planes. The second was to insure that all panels within a plane were electrically connected to provide a common ground for all interior cell walls. And finally, they provided the ends of the panel wires with R/F shielding. To prevent arcing from the non-instrumented minitubes at the base of the planes, the interior walls of the sheets were insulated there with electrical tape. The final step in construction of the planes was to insure that all were gas tight, as the gas mixture contained ethane, a flammable gas. The finished planes were then positioned within the marble slabs of the MRG. Figure 15 shows the location of each x - y pair within the MRG. The spacing was chosen so as to provide a 10% momentum resolution.

A critical concern for the MRG was the concept of wire aging. The gas cells within the MRG planes were highly active chemically. This, combined with the presence of simple hydrocarbons, would have allowed the formation of large, complex molecules. These molecules could then have formed fibrous deposits on the wires. These deposits would in turn lower the electric field, reducing the performance of the cell, and eventually lead to electrical arcing between the fibers and the cell walls. Three methods were used to reduce aging. First, the gas mixture used in the MRG, 49.2% argon, 49.2% ethane and 1.6% ethanol, has been shown to provide long wire life. Second, high gas flow rates have been reported to slow aging by flushing the complex molecules out of the tube before they can be deposited on the wires. Third, since the gas will gradually be contaminated with complex molecules as it flows through the tubes, the gas supply flow through the planes was designed to minimize the time spent within the planes (within limits) by a given volume of gas, especially in the critical regions of high particle flux. This was the underlying principle for the gas distribution scheme described above for the panels. By dividing the y panels into two independent groups of eight panels, the time a given gas volume remained in the tubes was halved. And placing the group inputs in the central panels, insured a clean gas supply in the critical central region of the y -planes. A similar situation applied to the x -planes, but in this case, only four panels were linked together along the inner edge. This was primarily of concern in the 1988 run when no helium bag was present between the MRG arms, leading

to significantly higher particle fluxes in the innermost x -panels caused by the interaction of the neutral beam with the interior support struts of the MRG frame. With the addition of the helium bag, this problem was substantially reduced.

Figure 48 displays the MRG gas system. Argon and ethane were fed into a mixing volume through separate channels of a mass flow controller, which fixed each flow rate at four liters per minute, providing a 50/50 mixture. The mixture then passed through a gas washer bottle containing ethyl alcohol, maintained at a constant 1° C, to insure the proper ethanol concentration. This final mixture then flowed out to the MRG where it entered two 10 cm polyethylene pipes which ran the entire length of the MRG in either arm. These pipes then supplied the panels *via* PolyFlo tubing. The panel exhausts were connected by PolyFlo to two identical pipes which then directed the exhaust gas back to the third channel of the mass flow controller and then out into the atmosphere. This third channel monitored the exhaust rate as a check on major leaks within the MRG.

A small scale version of a MRG panel was used to separately sample both the input and exhaust gas supplies. This monitor panel differed in only two respects from a standard MRG panel. First, it was only 30 cm long. Second, a thin beryllium window was installed over one cell. On a regular basis, the gas gain of the monitor panel was measured using a ^{55}Fe x-ray source over the panel window, to insure gas quality.

A.2.3 Electronics

The quality control tests determined that the optimum running voltage for the MRG wires was +2,650 volts. At this voltage, all panels were operating on their efficiency plateaus, and well below their trip voltages. A multichannel Bertan high voltage supply unit was used to maintain MRG high voltages. The Bertan supply was controlled by a DEC GIGI computer. The GIGI was programmed to display all MRG plane voltages and currents on a continuous basis, and to sound an alarm if planes tripped or exceeded tolerances.

The Bertan distributed high voltage to the panel amplifier cards *via* SHV cable. Each amplifier card then fanned out the high voltage to each individual wire. Amplifier cards were distributed among the MRG panels on a one-to-two basis. Each card provided high voltage to 16 channels, with each channel consisting of the two wires of a single cell linked together. Pulses from the wires were capacitively coupled to a three-stage ECL 10116 line-receiver, which provided a gain of 128. The amplifier was isolated from the high voltage by a 2200 pF capacitor[52]. The amplifier cards were grounded to the MRG planes using

copper tape in order to suppress high-frequency noise.

The amplifier signals were passed through 18", 17-pair unshielded twist-n-flat cable (the 17th pair also provided the DC power for the amplifier cards) to a discriminator card. At the discriminator board, the amplifier signals were required to pass a preset threshold by a TL180 voltage comparator, which then triggered a 74LS123 monostable multivibrator. The threshold voltages were controlled on a plane-by-plane basis from the experimental counting house. The width of the multivibrator output pulses was set to 150 ns. The discriminator cards were designed for individual readout of the output pulses from each channel (for use in the polarimeter experiment). However, this feature was used only for testing during the initial MRG startup prior to each yearly run. Instead, the eight signals from a single panel were logically OR'd together.

The OR signal was then transmitted a maximum of three meters over twist-n-flat cable to an adapter card. At the adapter card, the 28 OR signals from the pair of x - y planes within a given gap were transferred to a 300 foot Ansley cable for the journey to the latch modules in the experimental counting house (see Section 4.5.3).

A.3 Particle Identification

As mentioned in Section 5.4.1, several tighter cuts were tested for the MRG muon identification, in addition to the standard cut described there. (*n. b.* Familiarity with the MRG subsection of Section 5.4.1 is assumed for the following discussion.) The results of these tighter cuts are presented in Table 9. The simplest modification to the MRG cut was to tighten it to $gap_{actual} - gap_{expected} > -2.5$, referred to as the tight standard cut. As can be seen, the tight standard cut provided only limited improvement in pion and electron rejection. This is to be expected, since it has the same problem as the standard cut. The next two cuts address the problem of the standard cut, *i. e.* particles with a low expected gap number which automatically pass the standard cut.

One method to stop misidentification arising from the low expected gaps was to require very tight agreement between the actual and expected gaps for the low momentum, while reverting to the loose standard cut for high momentum. The first such cut (referred to as GAP 1) basically required that any particle with an expected stop gap greater than one pass the standard cut. Any particle with a expected stop gap of one must have an actual stop gap of one or more to pass the MRG cut. The second cut (referred to as GAP 2)

Cut Name	Muon ID	Pion ID	Electron ID
Standard	99.13	17.08	42.51
Tight Standard	98.71	11.79	33.35
Standard GAP 1	98.19	15.22	37.11
Tight GAP 1	97.83	10.81	29.75
Standard GAP 2	95.47	8.87	19.93
Tight GAP 2	95.16	7.17	18.05

Table 9: Identification efficiencies for various tight MRG cuts.

extended this idea to the second gap. The tight version of GAP 1 (GAP 2) used the tight standard cut for expected gaps greater than one (two). As can be seen in Table 9, these cuts significantly reduce both pion and electron misidentification. The price of this reduction is apparent in the steady decrease in muon efficiency. These types of cut could be extended to include the third gap (perhaps slightly looser by allowing an actual stop gap of two to pass an expected stop gap of three), but the cost in muon ID efficiency was already too high with the GAP 2 cut. The conclusion to be drawn from this study is that the simple track counter association used in the MRG and the simple gap difference cut, while satisfactory in a low background environment, cannot handle high background rates without seriously lowering the $K_L \rightarrow \mu^\pm e^\mp$ sensitivity. This problem would be addressed in the 1990 analysis by introducing an entirely different algorithm for track counter association.

A.4 Performance

The MRG has performed extremely well during E791's three physics runs (1988-1990). Each year, the standard muon identification efficiency was over 99%. Of its 11,648 wires, only 28 developed problems (lack of signal, constant signal or breakage). This low failure rate permitted removal of the few failed wires from voltage without significantly degrading the MRG's tracking potential. While individual electronics cards (both amplifier and discriminator) occasionally malfunctioned, the MRG design allowed for quick removal and installation of spares. The MRG has shown no signs of deterioration. Furthermore, examination of the seven wires which broke (all during the startup period prior to the Spring 1990 run) revealed no signs of aging. This breakage itself was linked to excessive alcohol concentration in the gas mixture (as evidenced by the fact that all seven wires were located under the input port of gas input cells, all seven broke at the input end of the extrusion,

the broken ends showed burn marks, and alcohol was found pooled in several gas couplings and in the main gas input pipes) and not to a weakening of the wires or crimps.

A.5 Polarimeter

In the original proposal for E791, an attempt was to be made to measure the longitudinal polarization (P_L) of the μ^+ from the $K_L \rightarrow \mu\bar{\mu}$ decay. This measurement is of interest for two reasons. First, polarization can indicate the presence of CP violation. Various extensions to, and replacements for, the Standard Model which contain CP -violating mechanisms predict P_L which vary over a wide range. Thus, even a crude measurement can eliminate many models. Second, a measured polarization in excess of that expected by the Standard Model would be evidence of the existence of a contribution to $\Gamma(K_L \rightarrow \mu\bar{\mu})$ by a mechanism not accounted for by the Standard Model. Much of the design of the MRG was driven by this goal, as previously indicated.

There are two possible states for the $\mu\bar{\mu}$ pair from $K_L \rightarrow \mu\bar{\mu}$, 1S_0 and 3P_0 . The former is a CP -conserving state, the latter is a CP and P -violating state. If parity is conserved, the muon pair must be in the 1S_0 state, which will display no polarization. However, muons from the 3P_0 state will have spins predominately aligned to their momentum vectors. One can determine the degree of polarization by measuring the distribution of positrons emitted by the decay $\mu^+ \rightarrow e^+ \nu_e \bar{\nu}_\mu$, which will be parallel to the muon's spin vector[53]. Thus:

$$P_L = \frac{N_L - N_R}{N_L + N_R} \quad (36)$$

where N_L and N_R are the number of left and right-handed muons respectively.

The Standard Model does predict a nonzero value for P_L of 0.001[54]. This arises from the small CP -even K_1 component of the K_L state. Furthermore, the contribution of the K_2 component can be derived from the effective Hamiltonian:

$$M(K_L \rightarrow \mu\bar{\mu}) = a_2 \bar{u}(p_-) \gamma_5(p_+) + i b_2(p_-) \nu(p_+) \quad (37)$$

where a_2 and b_2 represent the CP -conserving and violating modes respectively. Herczeg finds the following relation[54]:

$$P_L = \frac{2r\Im(b_2 a_2^*)}{|a_2|^2 + r^2 |b_2|^2} \quad (38)$$

where

$$r = \left(\frac{1 - 4m_\mu^2}{m_k^2} \right)^{\frac{1}{2}}.$$

This reduces to $P_L \sim b_2/a_2$ if a_2 dominates.

The range of values for P_L varies greatly for CP -violating models. At the low end are the predictions from supersymmetry[55] of less than 10^{-3} and from superstring models which give negligible results[56]. At the high end, a four-generation extension of the Standard Model can produce a P_L of 0.96[57], and leptoquark-fermion interactions can produce $P_L \sim 1$ [54].

Appendix B

The GEANT Monte Carlo Extension

This appendix describes a Monte Carlo package used to extended the standard offline Monte Carlo (MCSTD). The package is referred to as the GEANT Extension (MCGTEX). This package utilized the initial stages of the MCSTD to produce decay products and to track them through the low-density portion of the apparatus (from the target to the downstream face of the second bank of the TSCs), but incorporates a more realistic tracking package for the downstream high-mass detectors using a modification of the CERN GEANT Monte Carlo package.

MCSTD produced K_L of a given momentum and lifetime at the E791 target, based on the parameterization of Skubic *et al.* [49]. The parameterization was modified such that the K_L z -decay position and momentum distributions produced by the Monte Carlo for semileptonic decays agreed with data within a limited mass range[45]. The modified parameterization was then checked by comparing the same distributions for semileptonic events outside that mass range. The K_L were forced to decay within the vacuum decay region. The program could be set to decay randomly among the K_L decay modes (weighted by the actual decay fractions), or forced to decay into a given mode. The K_L decay daughters were then tracked through the spectrometer, using a fourth order Runge-Kutta integration to simulate the effects of magnetic fields. Multiple scattering was modeled by the formula [13]:

$$\theta_{Ms} = \frac{14.1\text{MeV}}{p\beta} \sqrt{L/L_R} \left[1 + \frac{1}{9} \log(L/L_R) \right], \quad (39)$$

where L is the distance travelled, and L_R is the radiation length of the medium. This formula is only valid when a particle does not lose a significant amount of energy as it passes through the medium (which is true for the low density material forming the spectrometer, but is clearly false for downstream materials in the PBG, muon filter and MRG). With one exception, energy loss by particles was not accounted for as they traversed the E791 apparatus. The exception was electron bremsstrahlung which was modeled using the Tsai formulation[58].

The primary problems with the MCSTD were that the multiple scattering was not properly modeled for the high density material which appears in the downstream portion of E791, and ionization energy loss was not modeled at all. Instead, particle trajectories for the downstream detectors were formed by linear transport. One method for correcting this was to append a Monte Carlo package which can handle such tasks to MCSTD. One such package is GEANT. Unfortunately, direct incorporation of GEANT in MCSTD led to two major difficulties. First, the memory requirements of the resulting code exceeded that available for users of BNLVMA (the IBM 3090 computer of the BNL Computer Facility used by this analysis). Second, the time required to run a single Monte Carlo event through the analysis would be exorbitant. (The first problem would eventually disappear with the upgrade of BNLVMA with additional CPU and memory allocation; unfortunately this did not occur until after work on MCGTEX was well underway.) The task was to produce a stripped down version of GEANT which could be used by MCSTD. All information concerning GEANT in the following discussion is taken from the GEANT3 User's Guide[59]. For reference, Figure 49 and Figure 50 present the GEANT program structure and data structure respectively.

GEANT is a very versatile package capable of modeling experiments with highly complex geometries. However, it is this same versatility which results in high memory requirements, and in long running times per event. To handle complex geometries, GEANT uses a sophisticated, but time consuming, algorithm to search the JVOLUM (geometry setup) portion of dynamic storage to determine the next volume a particle must be tracked through upon leaving its current volume.

E791, while complex in most other ways, is geometrically simple. The experiment basically consisted of a series of rectangular boxes (the simplest geometry in GEANT) which were symmetrical in x and y . Furthermore, the primary direction in which particles moved was $+z$. The linear nature of E791 in the z direction meant that a particle exiting a given

volume of material (for example, the iron muon filter) in the z direction could only enter the volumes immediately prior to and following the current volume (following the above example, the air gap between the back of the PBG and the filter, or the air gap between the back of the filter and first MHO plane). Any motion in x or y was irrelevant for purposes of determining the next volume, unless the particle went out the sides. If this occurred, it had left the E791 apparatus entirely and was no longer of interest. This simplicity allowed the programmer to eliminate completely the JVOLUM storage (and its substorage arrays JSET(detector sets) and JDRAW (drawings)), the JROTM (rotations) storage and all routines associated with them. They were replaced with a small multidimensional array containing the x , y , and z dimensions for each volume (APEND), and one (NMEDIA) containing the tracking media number (used by JTMED (tracking media)).

Ordering APEND and NMEDIA such that all volumes were in the sequence observed by a particle travelling in the $+z$ direction allowed a further simplification in the GEANT program structure. The main GEANT tracking routine (GTRACK) no longer required the JVOLUM search routines (GMEDIA and GTVOL). Instead, it simply looped over APEND, either from the beginning for particles passed to MCGTEX by MCSTD, or from the volume of origin, for particles produced during MCGTEX tracking. If a particle exceeded an x or y boundary or exited the last volume in z , MCGTEX ceased tracking it. The direction of looping over APEND depended simply on whether a particle was moving in the $+z$ or $-z$ direction. This simplification resulted in a significant reduction in both memory and CPU time.

The next reduction in memory resulted from the elimination of the JVERTX (permanent vertex) storage. The only vertices of interest in the E791 analysis were the primary kaon decay vertices. Since these were handled by MCSTD, JVERTX was unnecessary. Similarly, since the storage of all detector hit information, digitization of detectors, and event identification were handled by the Standard Offline, dynamic storage and routines which handled these tasks (JSTAK, JKINE, JHITS, JDIGI, JXYZ, JRUNG and JHEAD) could also be discarded. This required the modification of the particle tracking routines (GTGAMA, GTELEC...), to remove all references to eliminated data structures. Furthermore, the routine which controlled looping over tracks (GTREVE) was completely rewritten to loop over a simplified stacking structure containing generated secondaries. However, the physics routines called by the particle tracking routines, which form the heart of GEANT,

required no modifications since the data structures on which they are based (JPART (particle data), JMATE (material data), and JT MED (tracking media)) were not modified. Several other major GEANT routines, for example GTRIG, were also eliminated since the Standard Offline performed their functions.

Obviously, the elimination of all of the above data structures also required the modification of several other GEANT routines, particularly the initialization routines. Figure 51 and Figure 52 show the modified data structure and program structure for MCGTEX. For comparison to standard GEANT, all routines which underwent modification have been renamed by replacing the initial 'G' with an 'M'.

Extensive tests were run on MCGTEX to insure valid results. As an example, one test was to run ten pions through a standard GEANT model of the downstream portion of E791, dumping every step. A stand-alone version of MCGTEX was then run on the same sample, using the same random number seeds as the standard GEANT job, and again dumping all steps. If MCGTEX is working properly, the two jobs should produce identical results on a step-by-step basis, as indeed was the case. MCGTEX resulted in a 90% reduction in dynamic storage over the standard GEANT job, with a roughly 50% reduction in initialization time.

Bibliography

- [1] M. Gell-Mann. *Phys. Lett.* **8**, 214 (1964).
- [2] R. Cahn and H. Harari. *Nucl. Phys.* **B176**, 135 (1980).
- [3] W. Carithers et al. *Phys. Rev. Lett.* **31**, 1025 (1989).
- [4] Y. Fukushima et al. *Phys. Rev. Lett.* **36**, 348 (1976).
- [5] M. Shochet et al. *Phys. Rev.* **D19**, 1965 (1979).
- [6] T. Inagaki et al. *Phys. Rev.* **D40**, 1712 (1989).
- [7] C. Mathiazhagen et al. *Phys. Rev. Lett.* **63**, 2185 (1989).
- [8] H. Foeth et al. *Phys. Lett.* **30B**, 282 (1969).
- [9] S. Glashow, J. Iliopoulos, and L. Maiani. *Phys. Rev.* **D2**, 1285 (1970).
- [10] D. Perkins. *Introduction to High Energy Physics*, pp.250–256 (Addison-Wesley, Reading, 1982).
- [11] F. Halzen and A. Martin. *Quarks and Leptons*, pp.279-283 (Wiley & Sons, New York, 1984).
- [12] B. Martin, E. de Rafael, and J. Smith. *Phys. Rev.* **D2**, 179 (1970).
- [13] Particle Data Group. *Phys. Lett.* **B239**, (1990).
- [14] A. Clark et al. *Phys. Rev. Lett.* **26**, 1667 (1971).
- [15] H. Stern and M. Gaillard. *Annals of Physics* **76**, 580 (1973).
- [16] M. Gaillard and B. Lee. *Phys. Rev.* **D10**, 897 (1974).

- [17] J. Aubert et al. *Phys. Rev. Lett.* **33**, 1404 (1974).
- [18] J. Augustine et al. *Phys. Rev. Lett.* **33**, 1406 (1974).
- [19] M. Kobayashi and T. Maskawa. *Prog. Theor. Phys.* **49**, 652 (1973).
- [20] A. Buras. *Phys. Rev. Lett.* **46**, 1354 (1981).
- [21] T. Inami and C. Lim. *Prog. Theor. Phys.* **65**, 297 (1981).
- [22] R. Shrock and S. Treiman. *Phys. Rev.* **D19**, 2148 (1979).
- [23] O. Shanker. *Nucl. Phys.* **B206**, 253 (1982).
- [24] L. Susskind. *Phys. Rev.* **D20**, 2619 (1979).
- [25] S. Dimopoulos and J. Ellis. *Nucl. Phys.* **B182**, 505 (1981).
- [26] S. Dimopoulos. *Nucl. Phys.* **B168**, 69 (1980).
- [27] S. Dimopoulos and L. Susskind. *Nucl. Phys.* **B155**, 237 (1979).
- [28] J. Ellis et al. *Nucl. Phys.* **B182**, 529 (1981).
- [29] D. L. Wagner. E791 Internal Memo KL-273. (1990).
- [30] K. A. Biery. E791 Internal Memo KL-302. (1990).
- [31] W. E. Slater. E791 Internal Memo KL-122. (1987).
- [32] R. D. Cousins, C. Friedman, and P. L. Mèlèse. *IEEE Trans. Nucl. Sci.* **36**, 646 (1989).
- [33] A. Schwartz and D. A. Ouimette. E791 Internal Memo KL-243. (1989).
- [34] K. A. Biery, D. A. Ouimette, and J. L. Ritchie. *IEEE Trans. Nucl. Sci.* **36**, 650 (1989).
- [35] R. D. Cousins et al. *Nucl. Instr. Methods* **A277**, 517 (1989).
- [36] P. F. Kunz. Technical Report, SLAC-PUB-3332, (1984).
- [37] T. Kaarsberg. E791 Internal Memo KL-232. (1989)
- [38] K. A. Biery and D. L. Wagner. E791 Internal Memo KL-270. (1989).

- [39] S. Imlay and W. Molzen. E791 Internal Memo KL-237. (1989).
- [40] R. Cousins and T. Kaarsberg. E791 Internal Memo KL-248. (1989).
- [41] T. Kaarsberg and D. L. Wagner. E791 Internal Memo KL-274. (1990).
- [42] D. L. Wagner. E791 Internal Memo KL-281. (1990).
- [43] R. Cousins. E791 Internal Memo KL-293. (1990).
- [44] M. Witkowski. private communication. (1992).
- [45] D. Wagner. Thesis. UCLA, Los Angeles, CA. (1990).
- [46] J. Margulies. Thesis. Stanford University, Palo Alto, CA. (1990).
- [47] J. Urheim and R. Cousins. E791 Internal Memo KL-229. (1989).
- [48] J. Urheim. Thesis. University of Pennsylvania, Philadelphia, PA. (1990).
- [49] P. Skubic et al. *Phys. Rev. D* **18**, 3115 (1978).
- [50] A. Heinson et al. AGS E871 proposal. (1990).
- [51] Y. Hoshi et al. *Nucl. Instr. Methods A* **236**, 82 (1985).
- [52] G. Hart. E791 Internal Memo KL-141. (1988).
- [53] S. DeBenedetti. *Nuclear Interactions*. pp. 573-597 (Robert E. Krieger, New York, 1964).
- [54] P. Herczeg. *Phys. Rev. D* **27**, 1512 (1983).
- [55] T. Kurimoto. *Phys. Lett. B* **172**, 357 (1986).
- [56] J. Liu. *Z. Phys. C - Particles and Fields* **37**, 139 (1987).
- [57] F. Botella and C. Lim. *Phys. Rev. Lett.* **56**, 1651 (1986).
- [58] Y. Tsai. *Reviews of Modern Physics* **46**, 4 (1974) and errata in **49**, 421 (1977).
- [59] R. Brun et al. *GEANT3 User's Guide*. Technical Report, CERN/DD/EE, (1986).

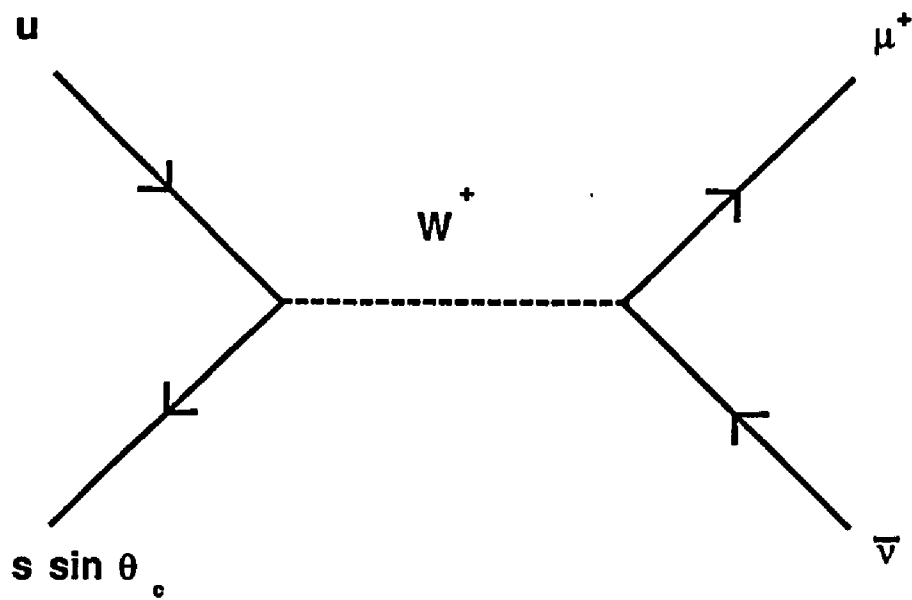


Figure 1

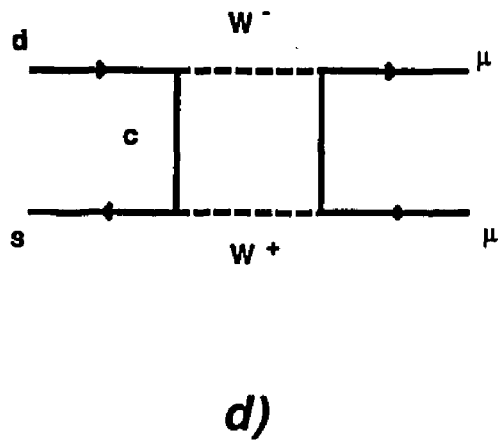
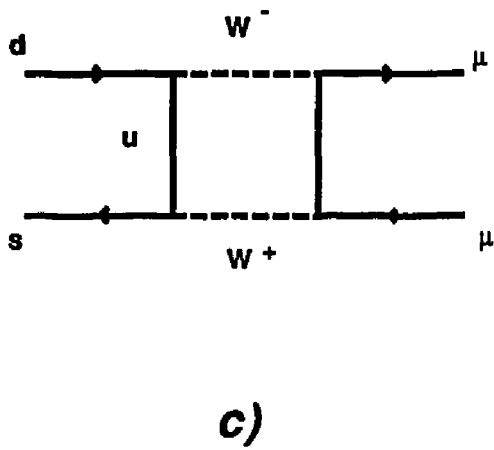
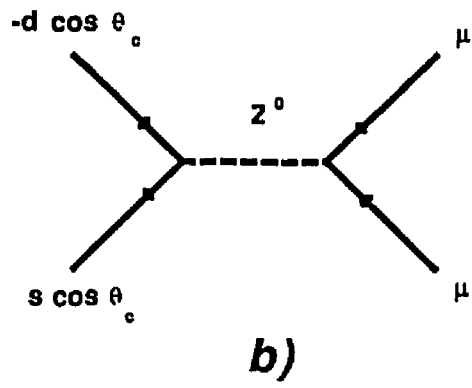
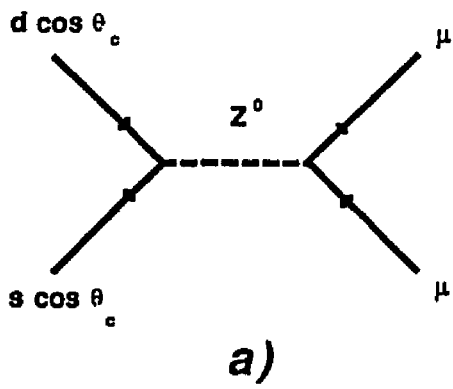


Figure 2

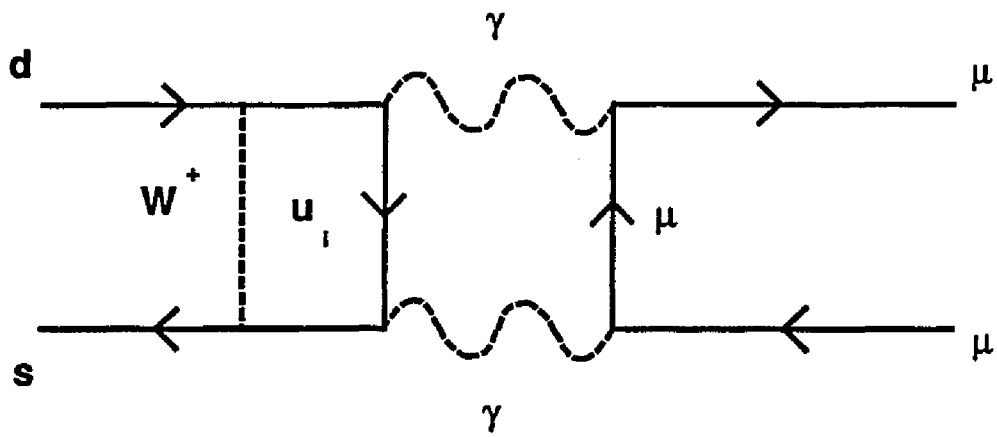
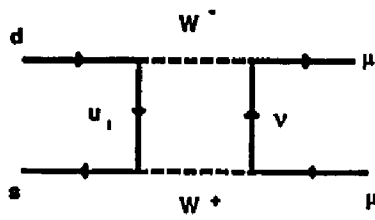
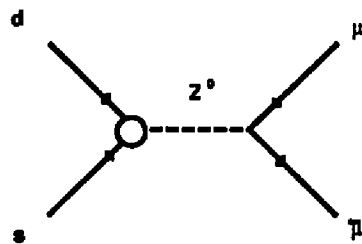


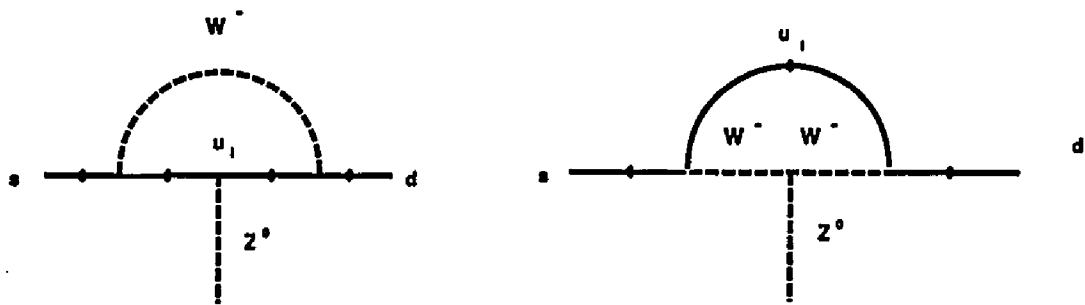
Figure 3



a)



b)



c)

Figure 4

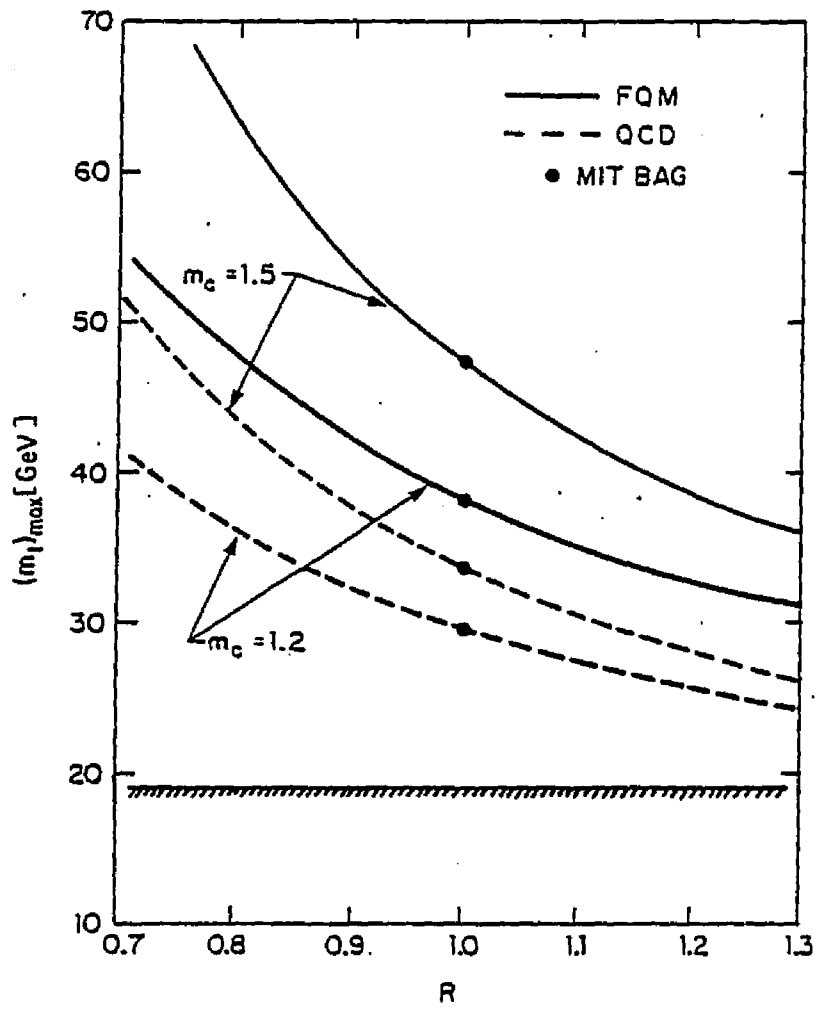


FIGURE 5

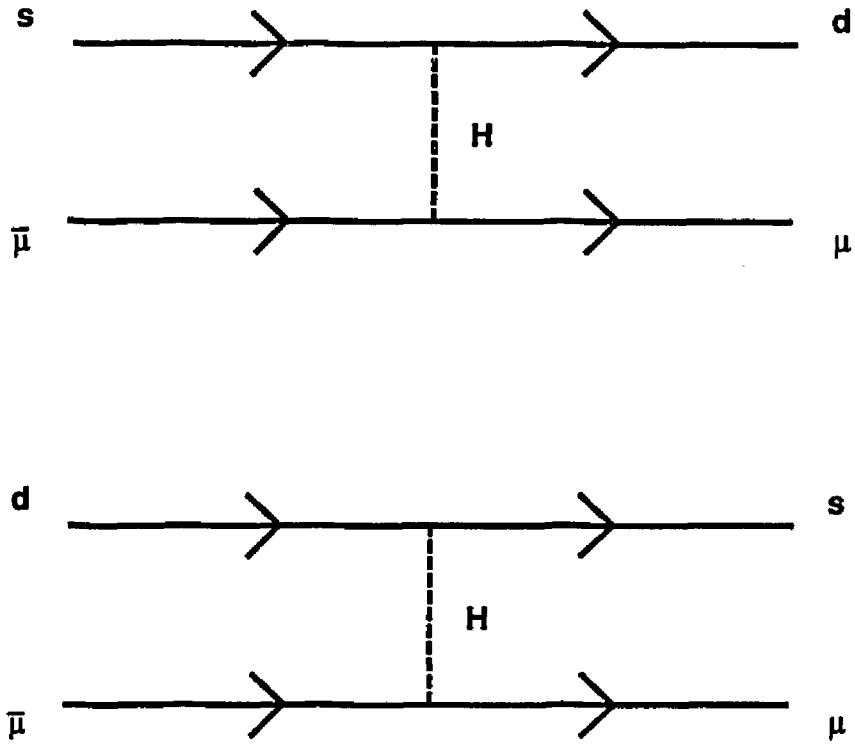


FIGURE 6

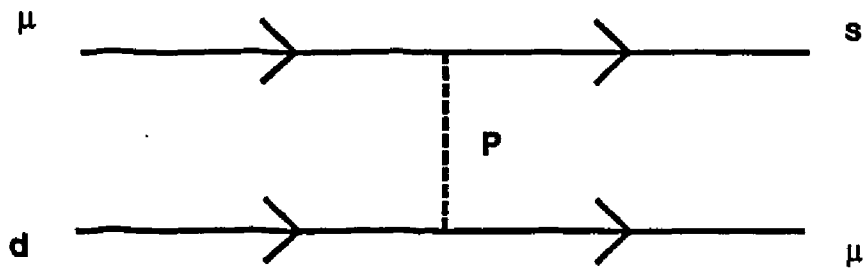
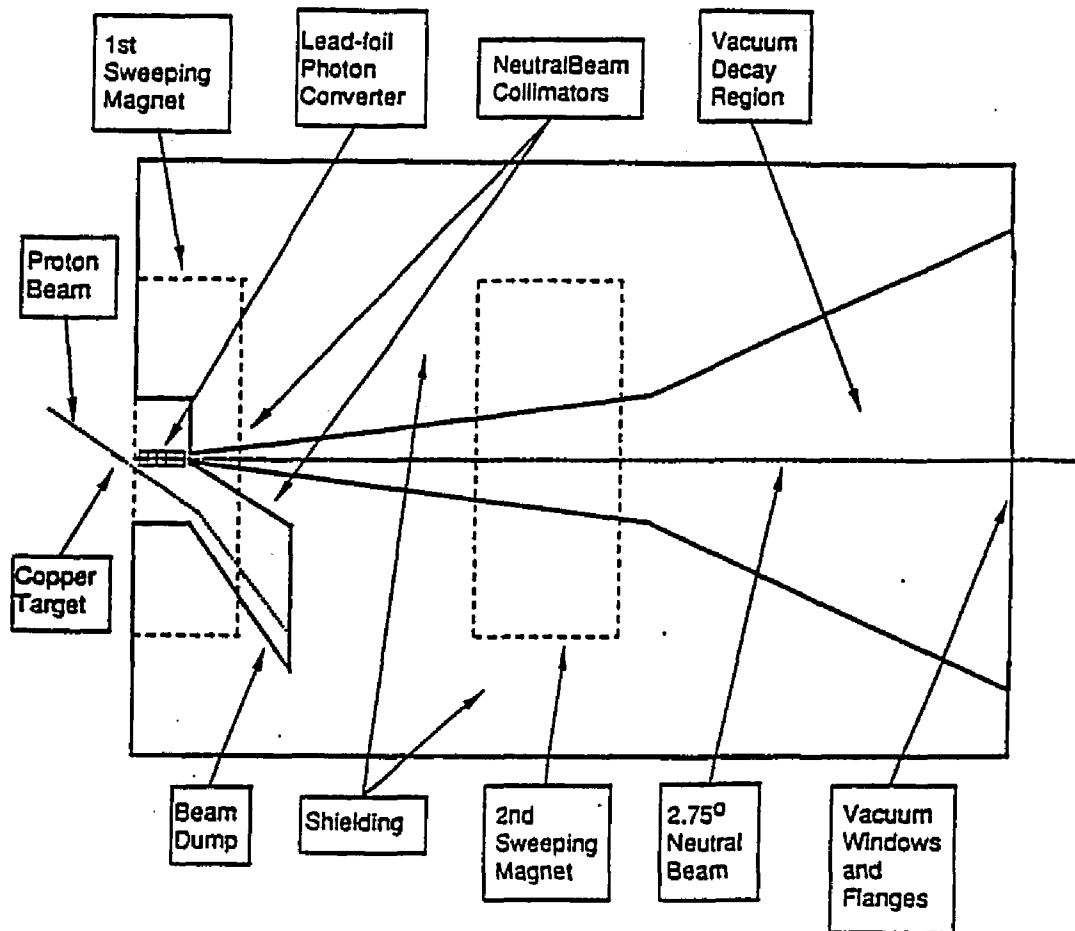


FIGURE 7



0.1 Meters
 1.0 Meters

FIGURE 8

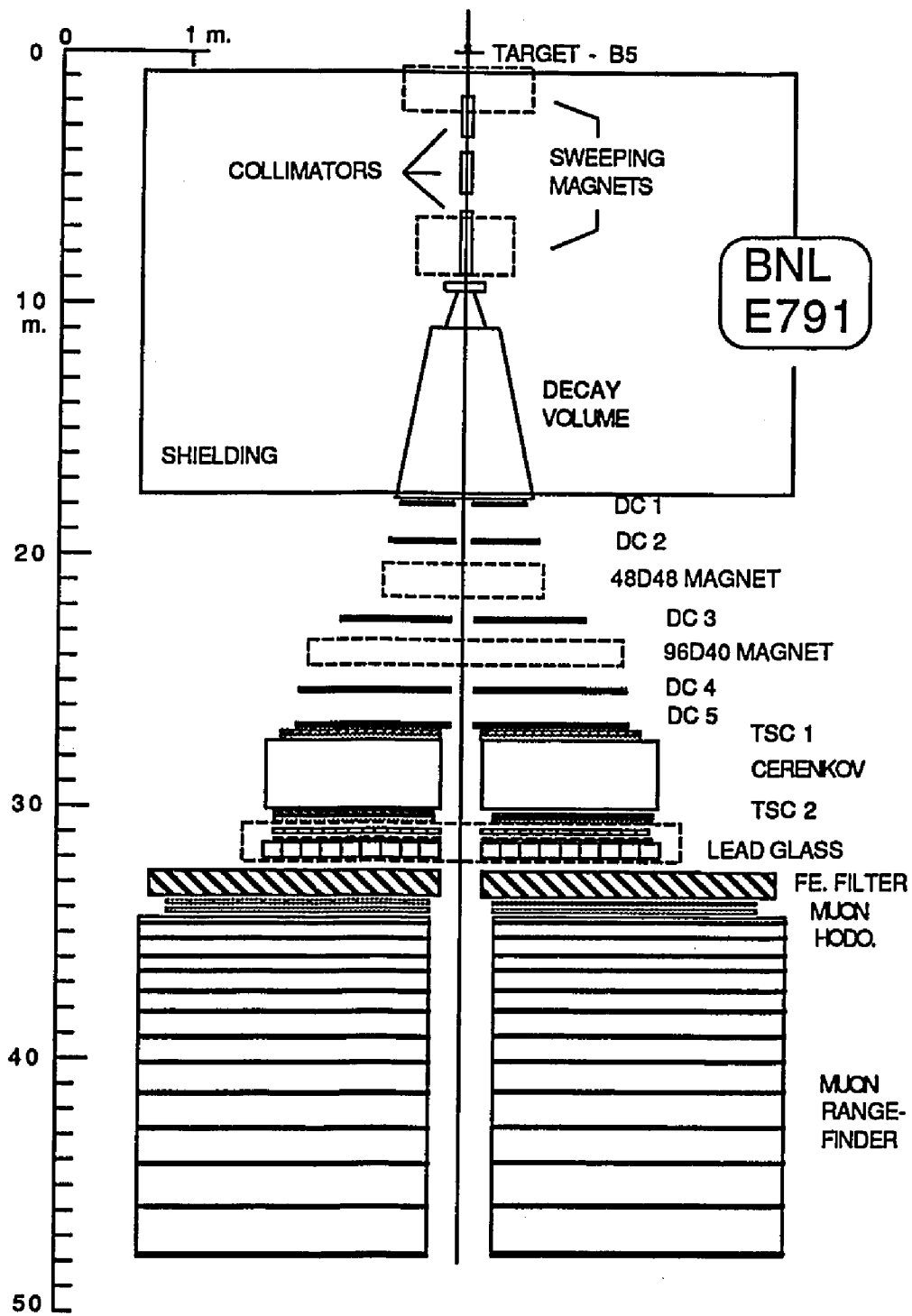
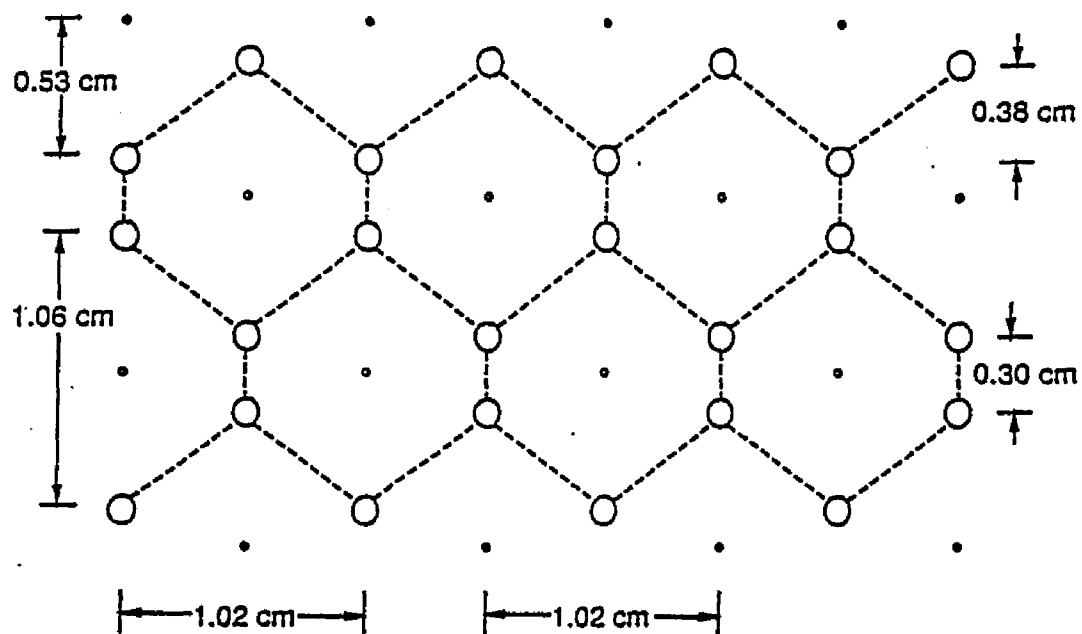


FIGURE 9



- — Field Wire - diameter=109 μm , potential=-2.500 V
- — Guard Wire - diameter=25 μm , potential=ground
- — Sense Wire - diameter=25 μm , potential=ground

FIGURE 10

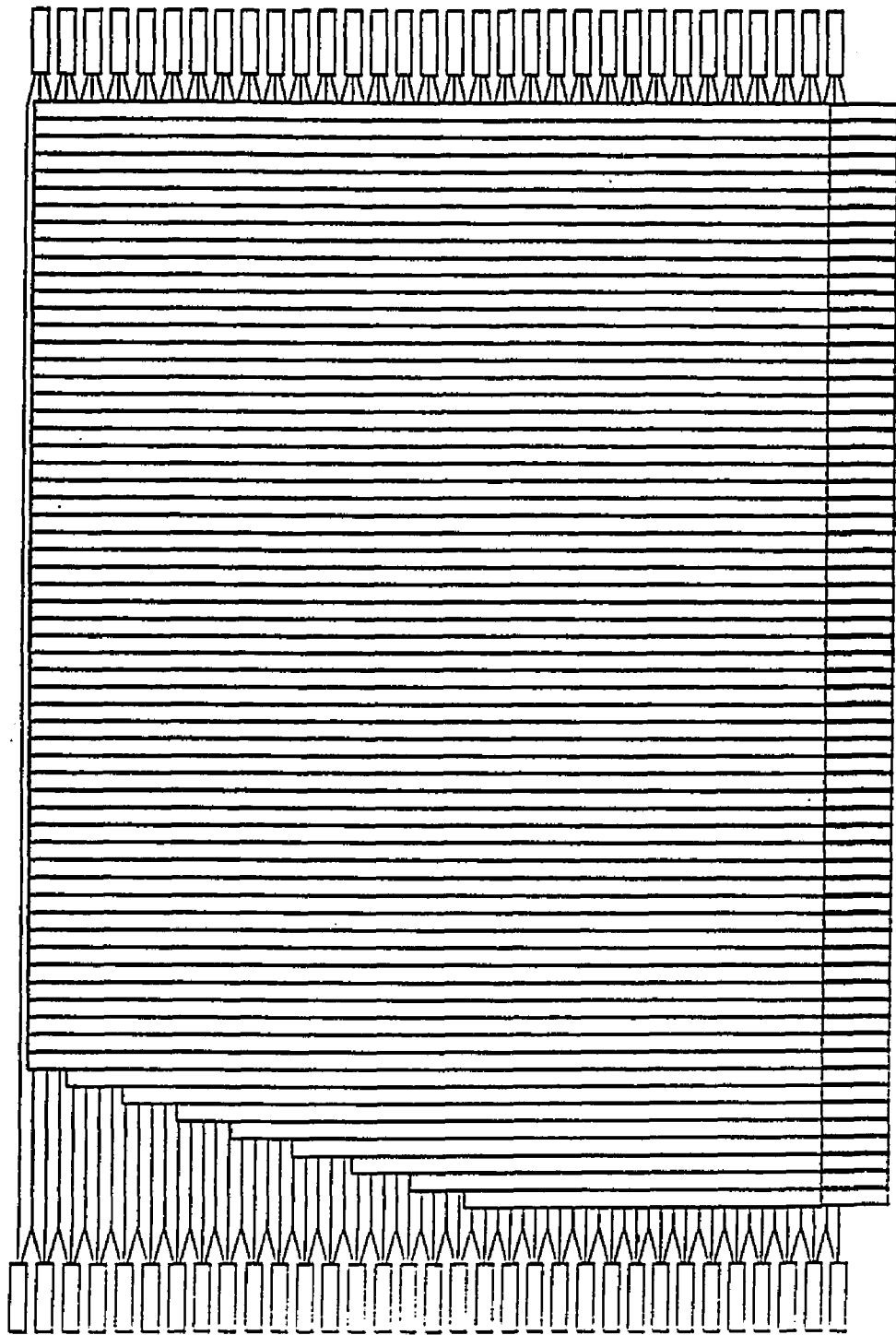


FIGURE 11

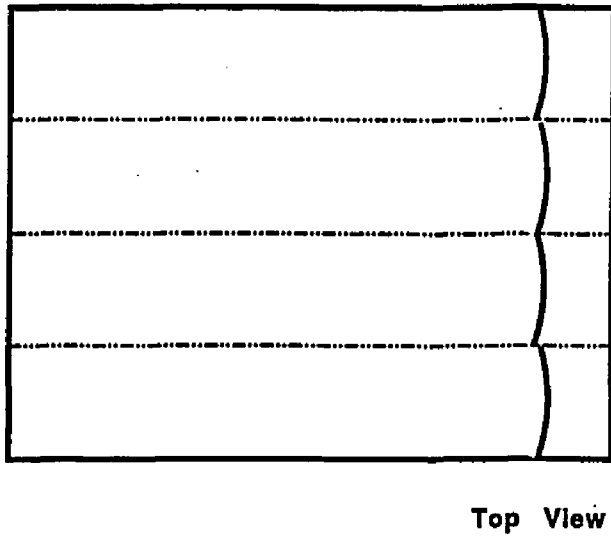
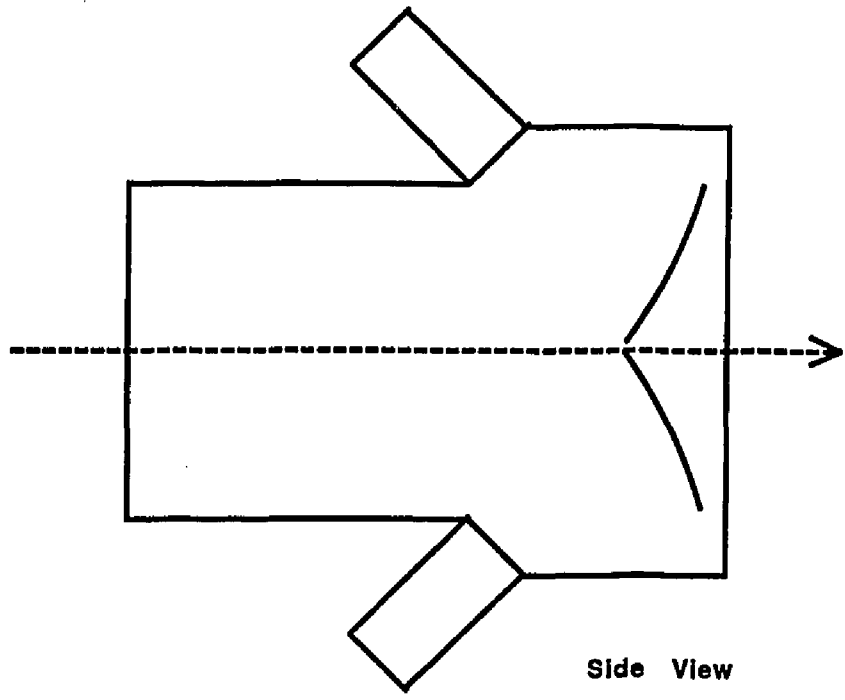


FIGURE 12

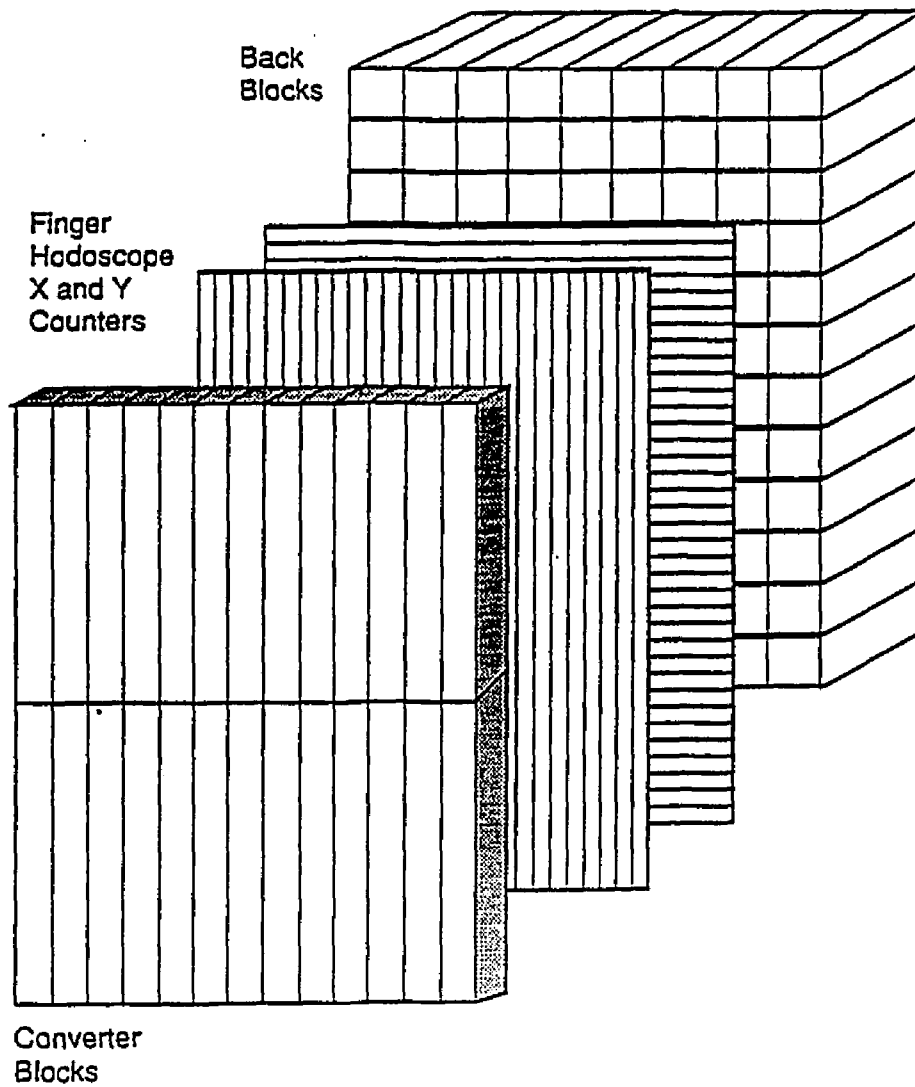


FIGURE 13

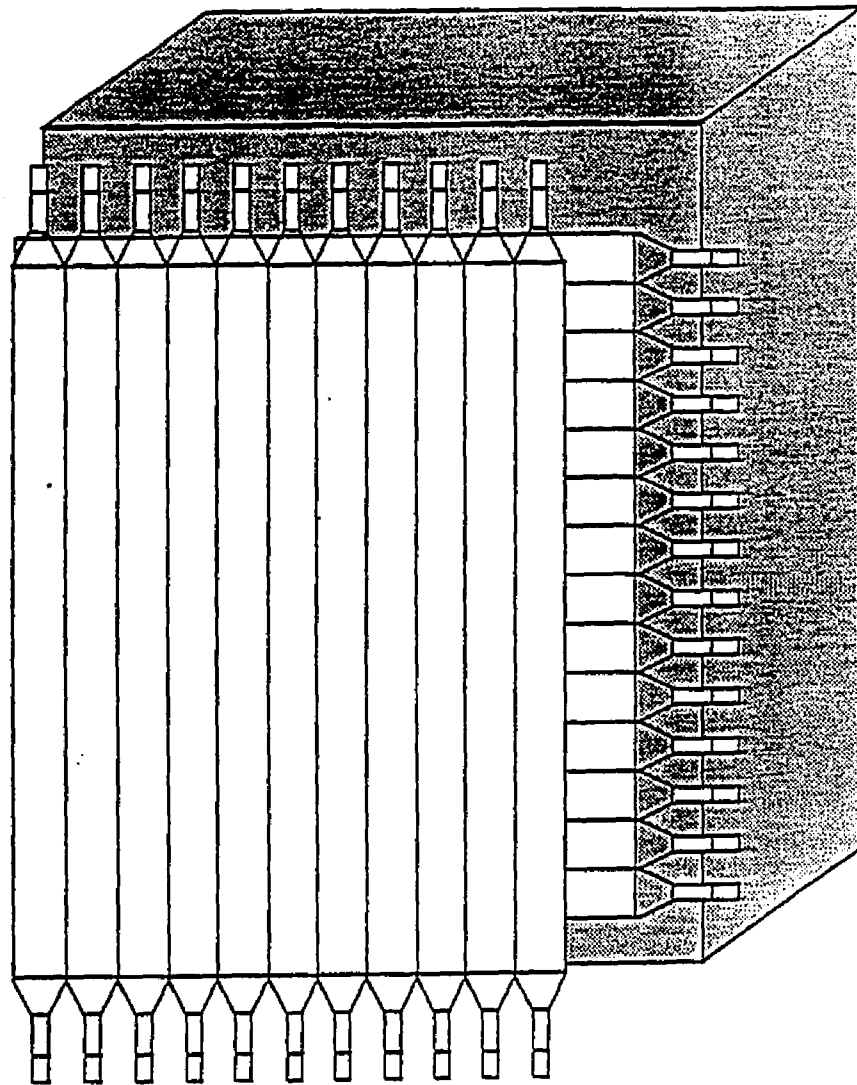


FIGURE 14

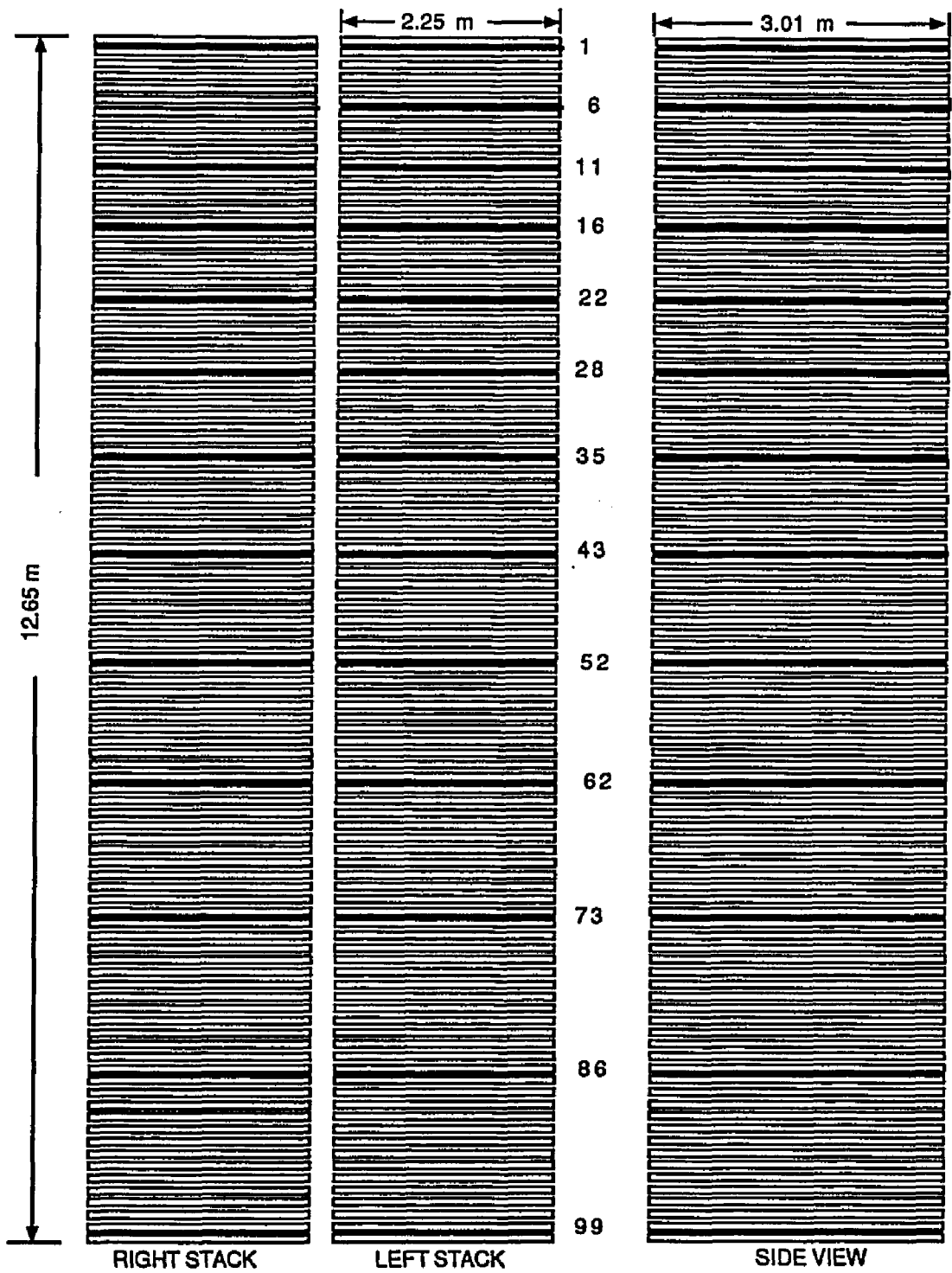


FIGURE 15

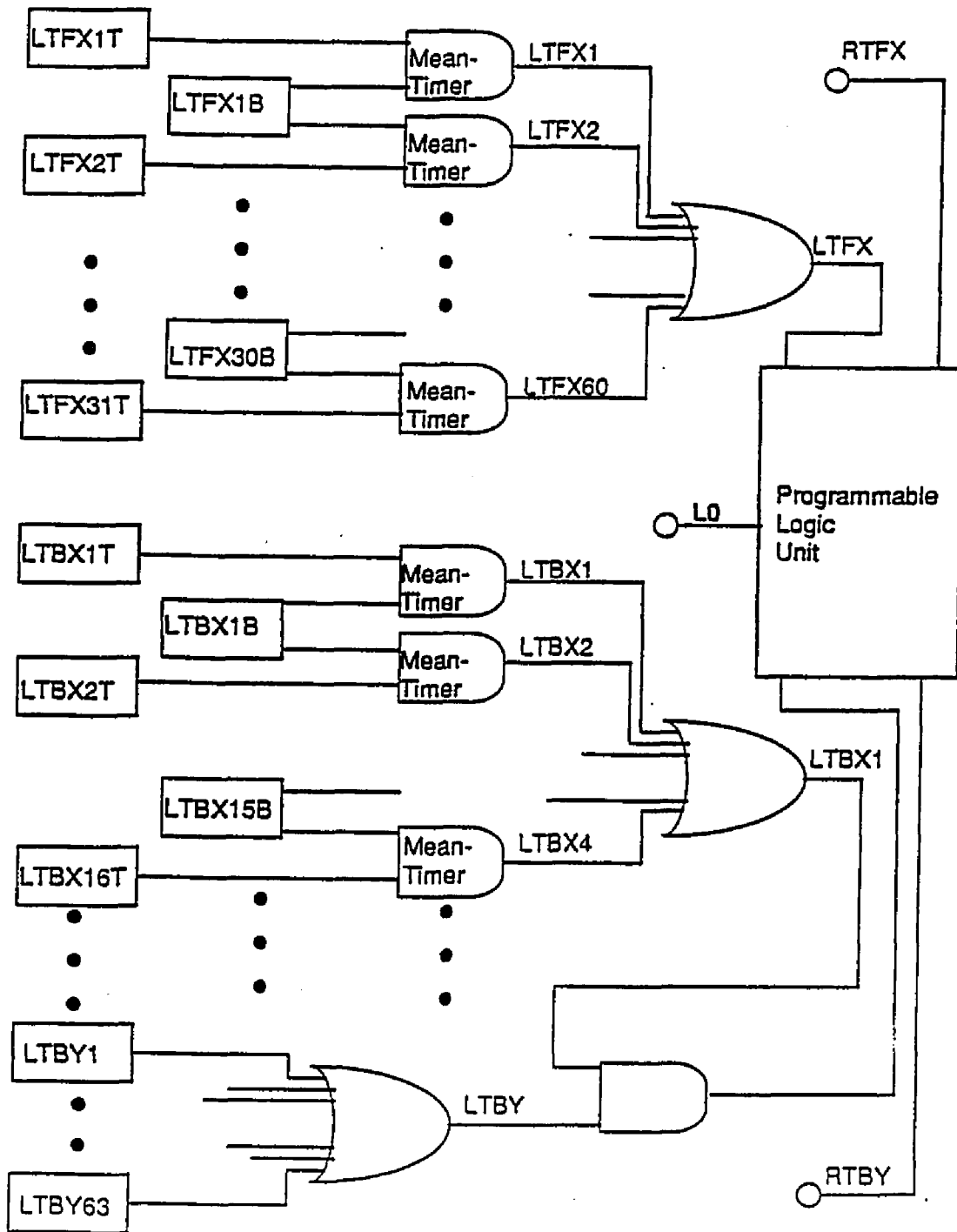


FIGURE 16

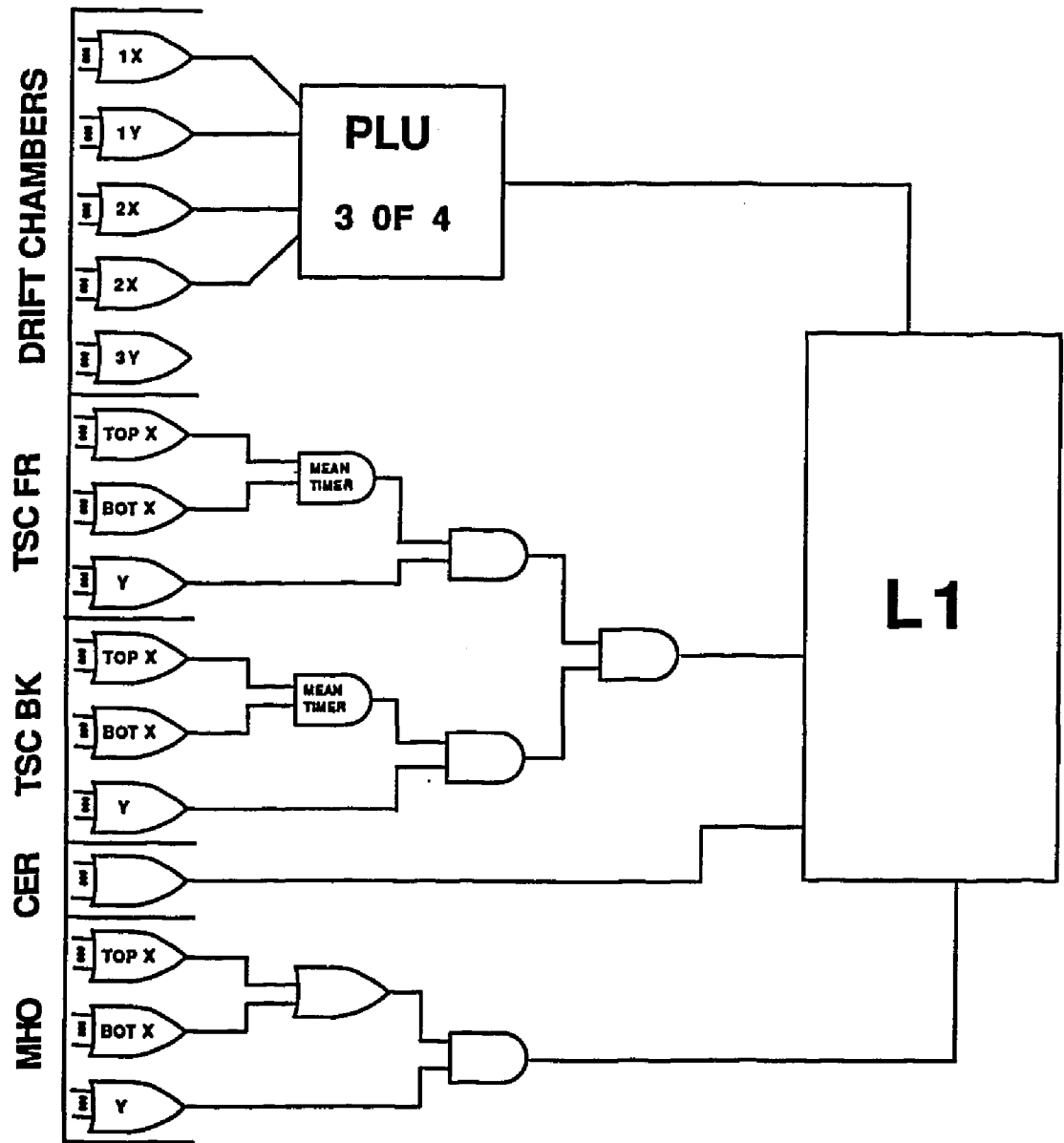


FIGURE 17

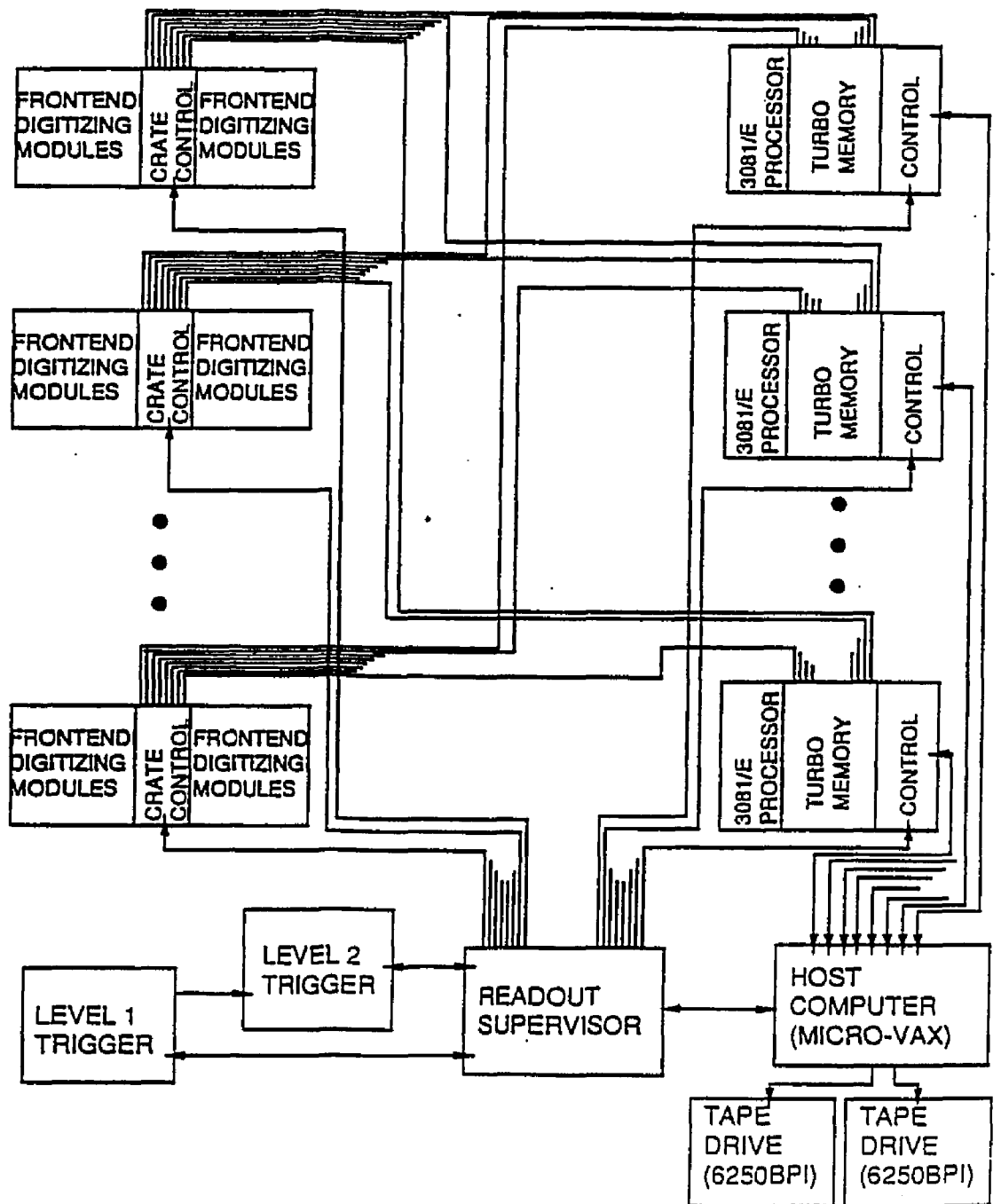


FIGURE 18

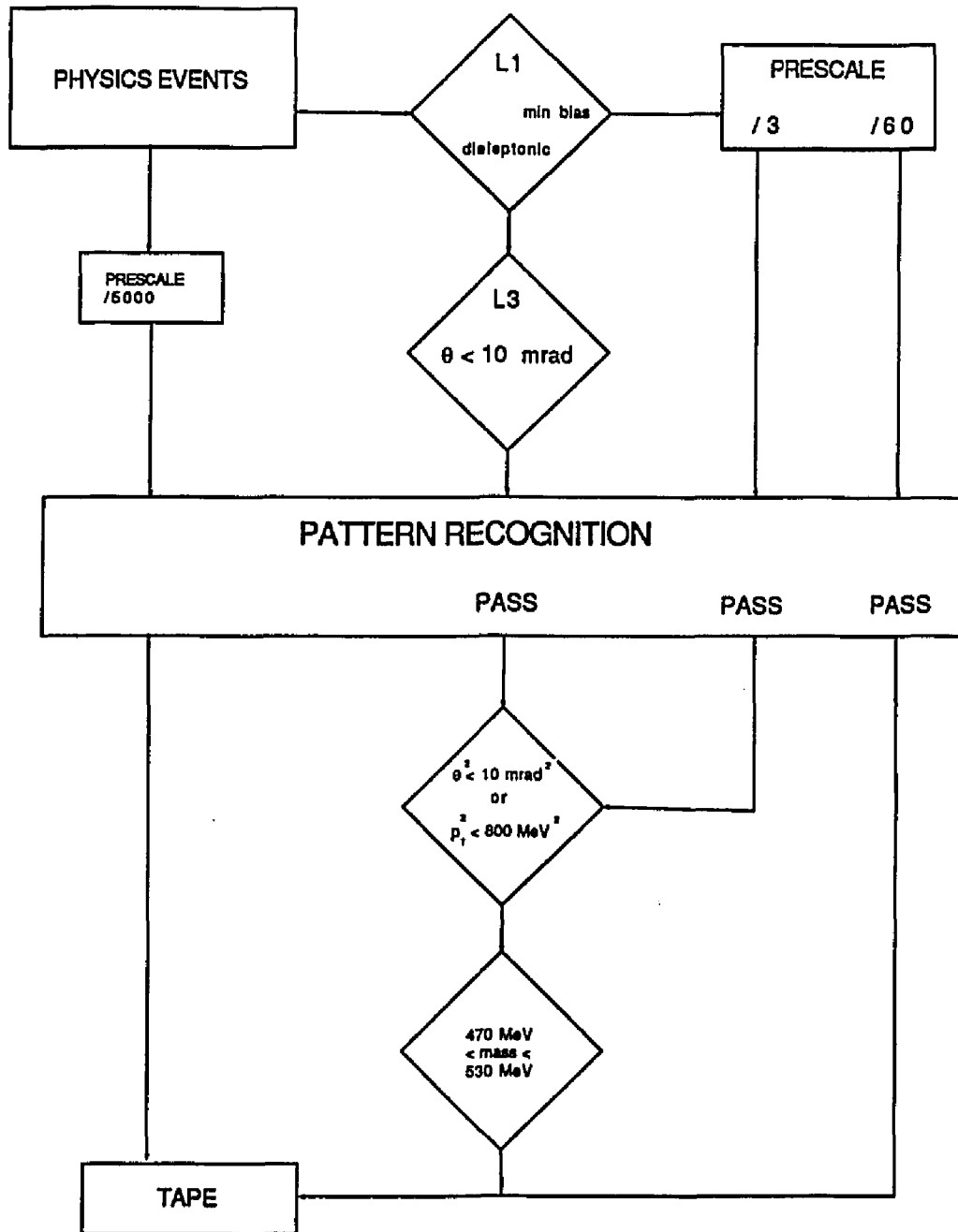


FIGURE 19

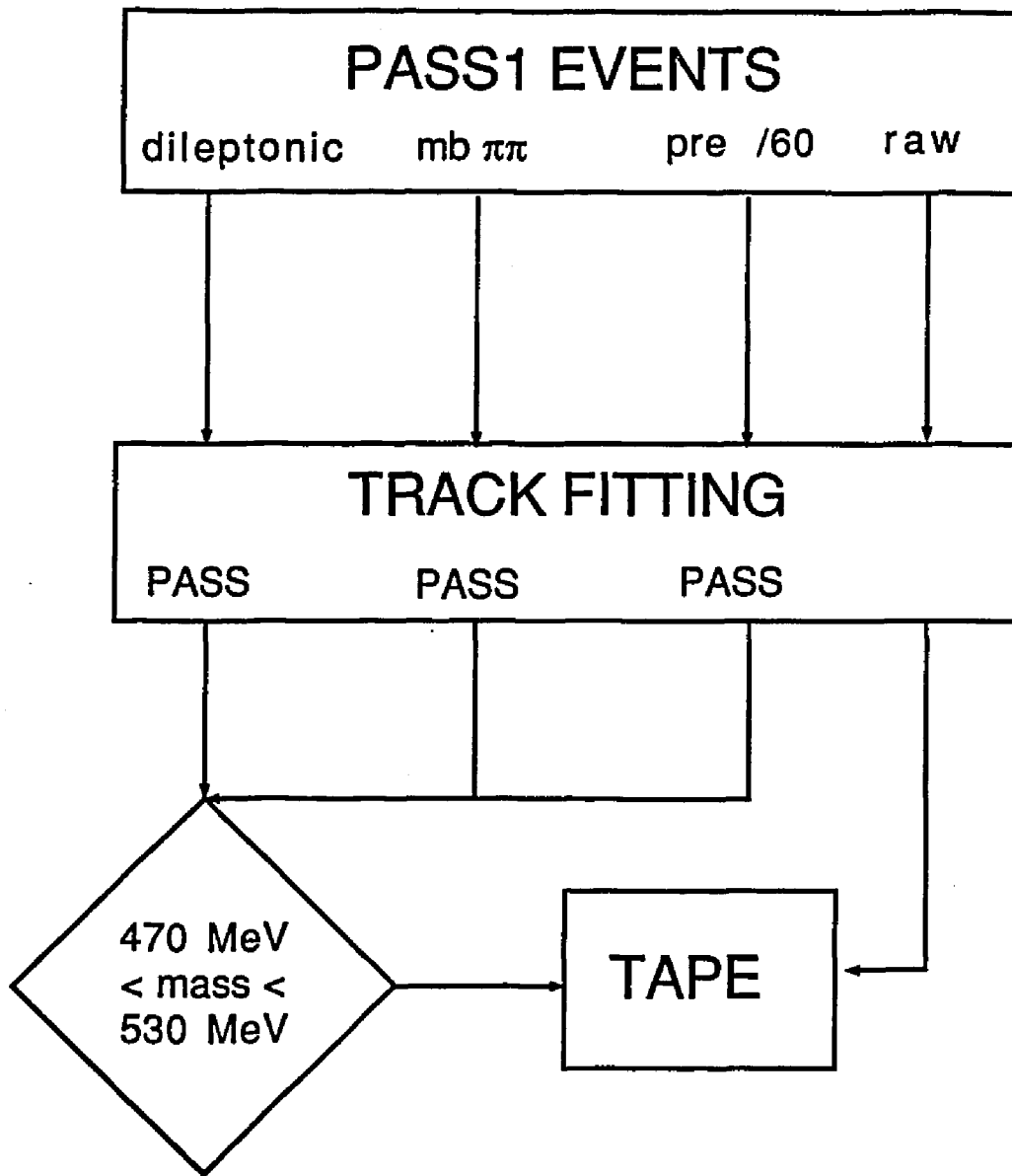


FIGURE 20

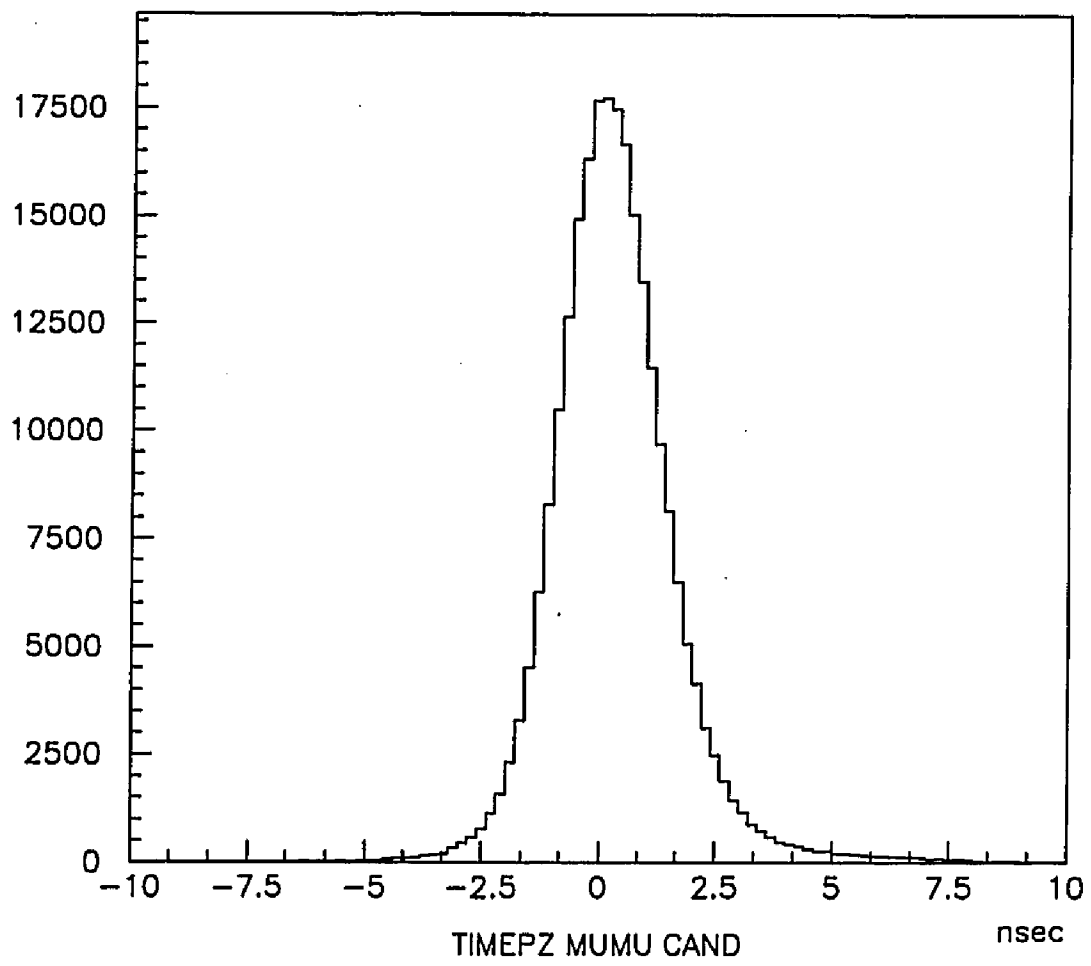


FIGURE 21

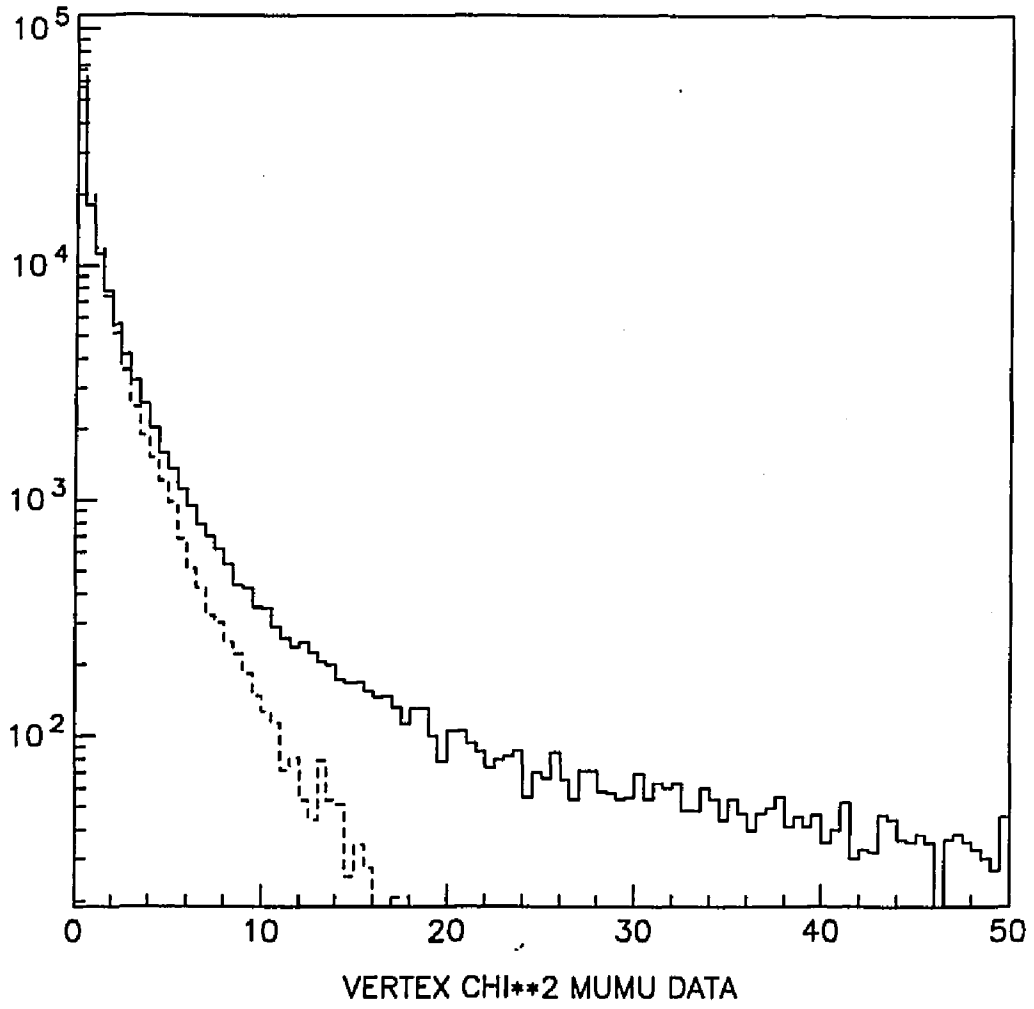


FIGURE 22

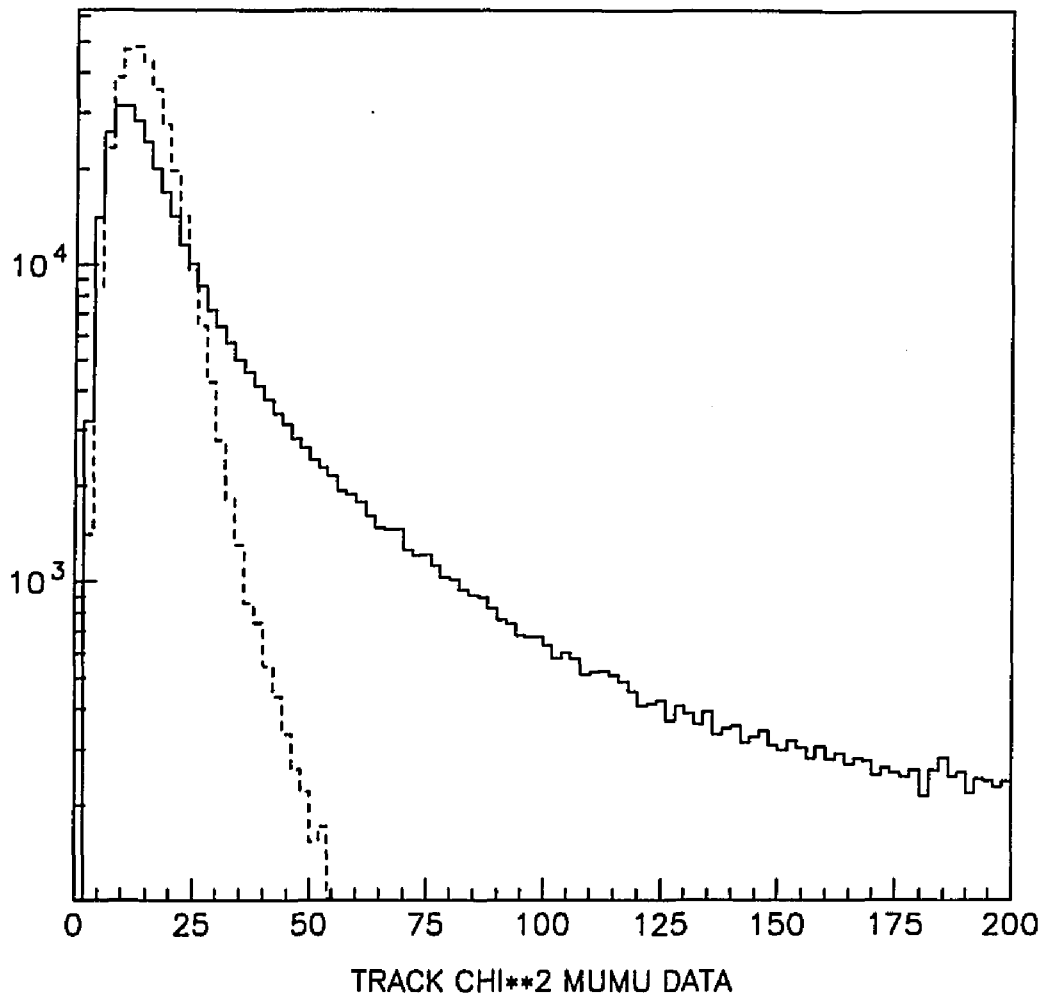


FIGURE 23

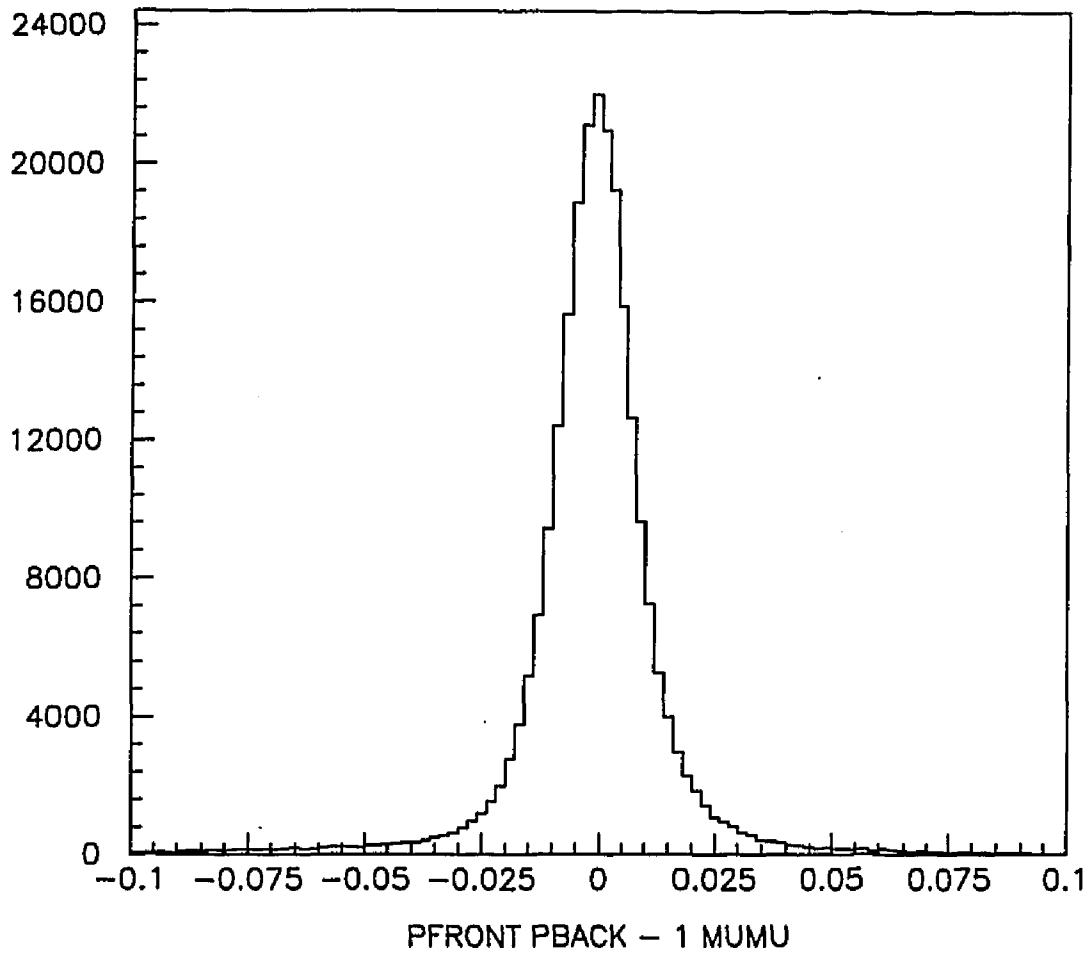


FIGURE 24

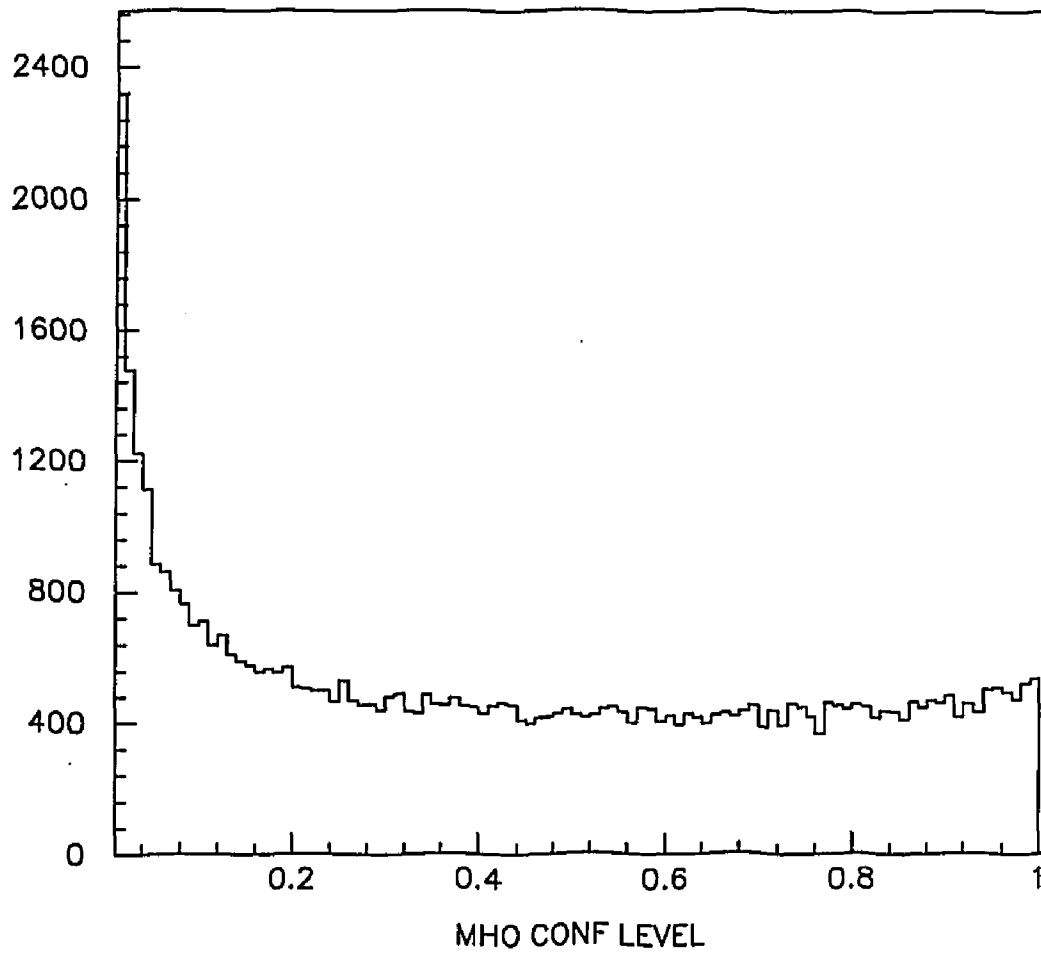


FIGURE 25

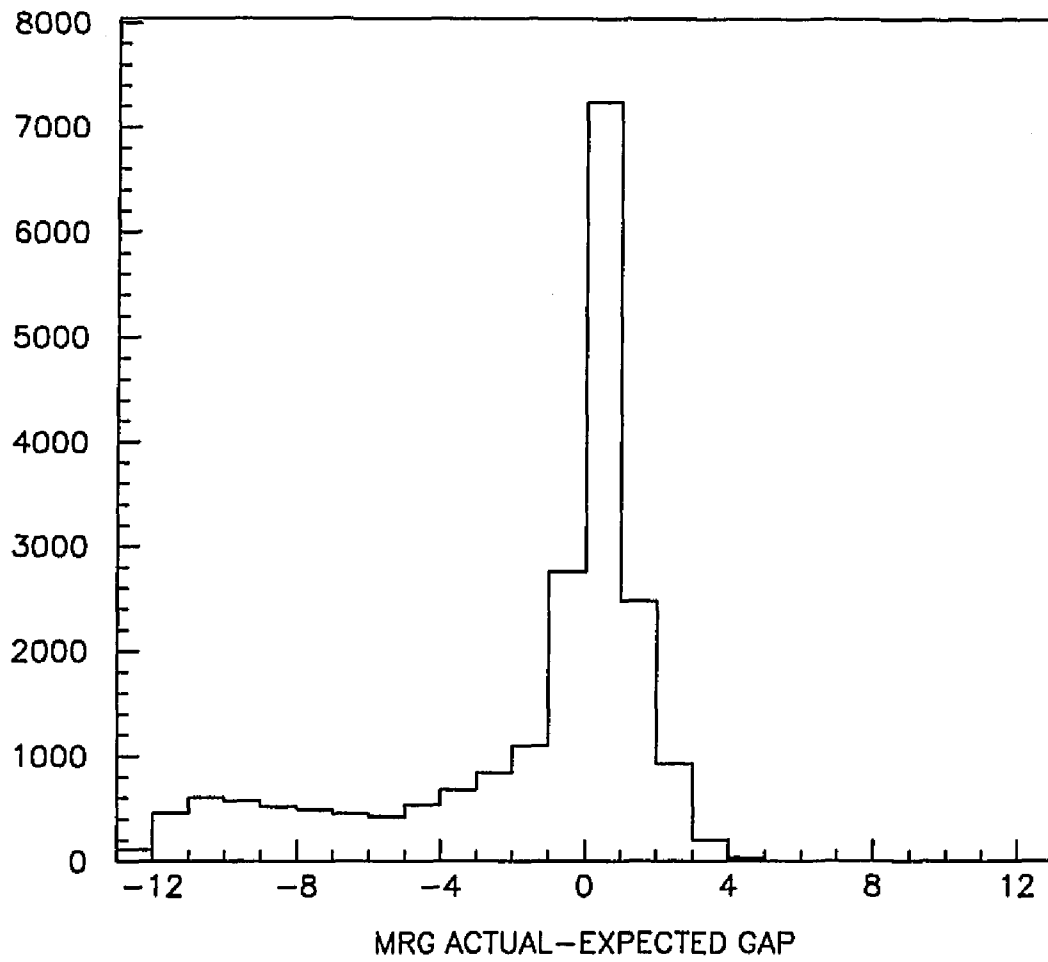


FIGURE 26

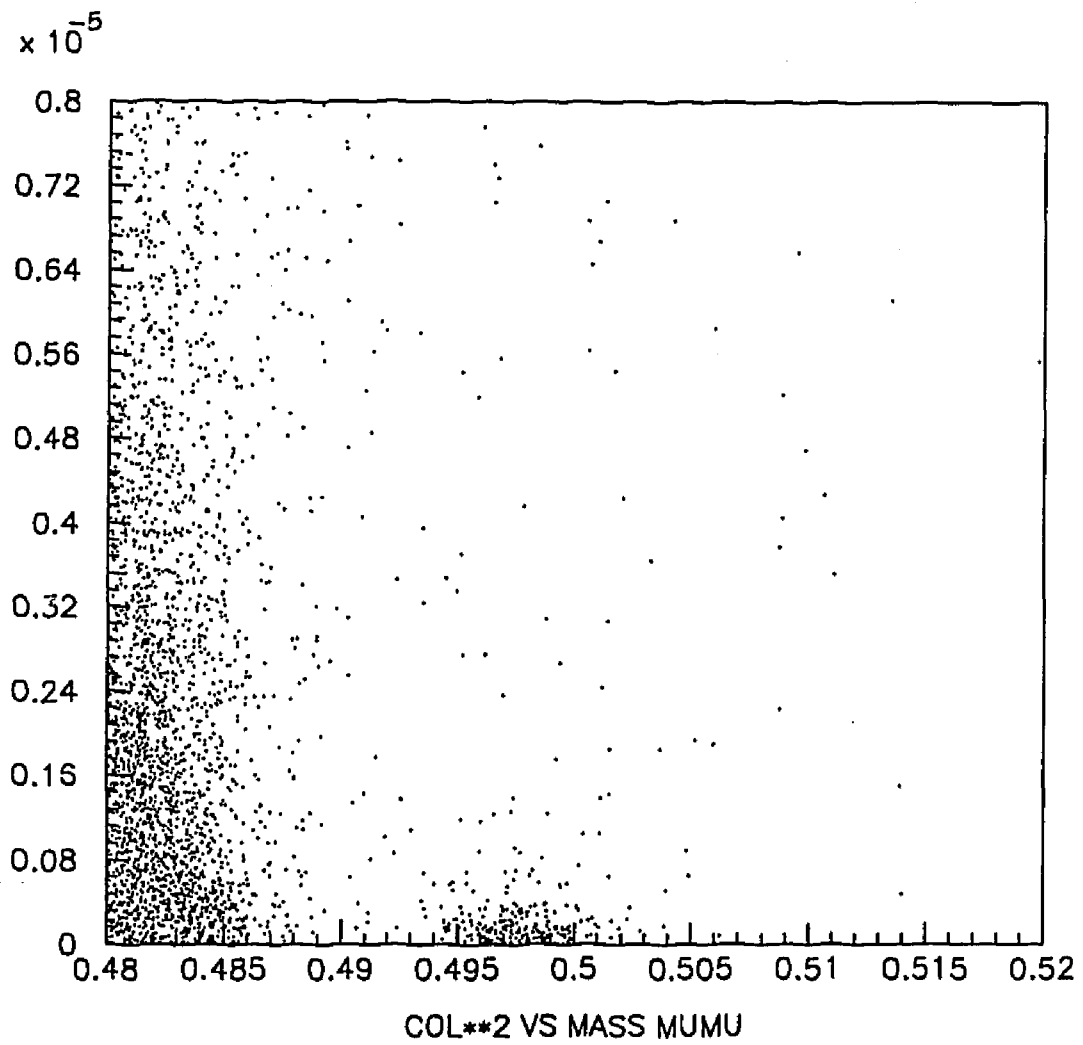


FIGURE 27

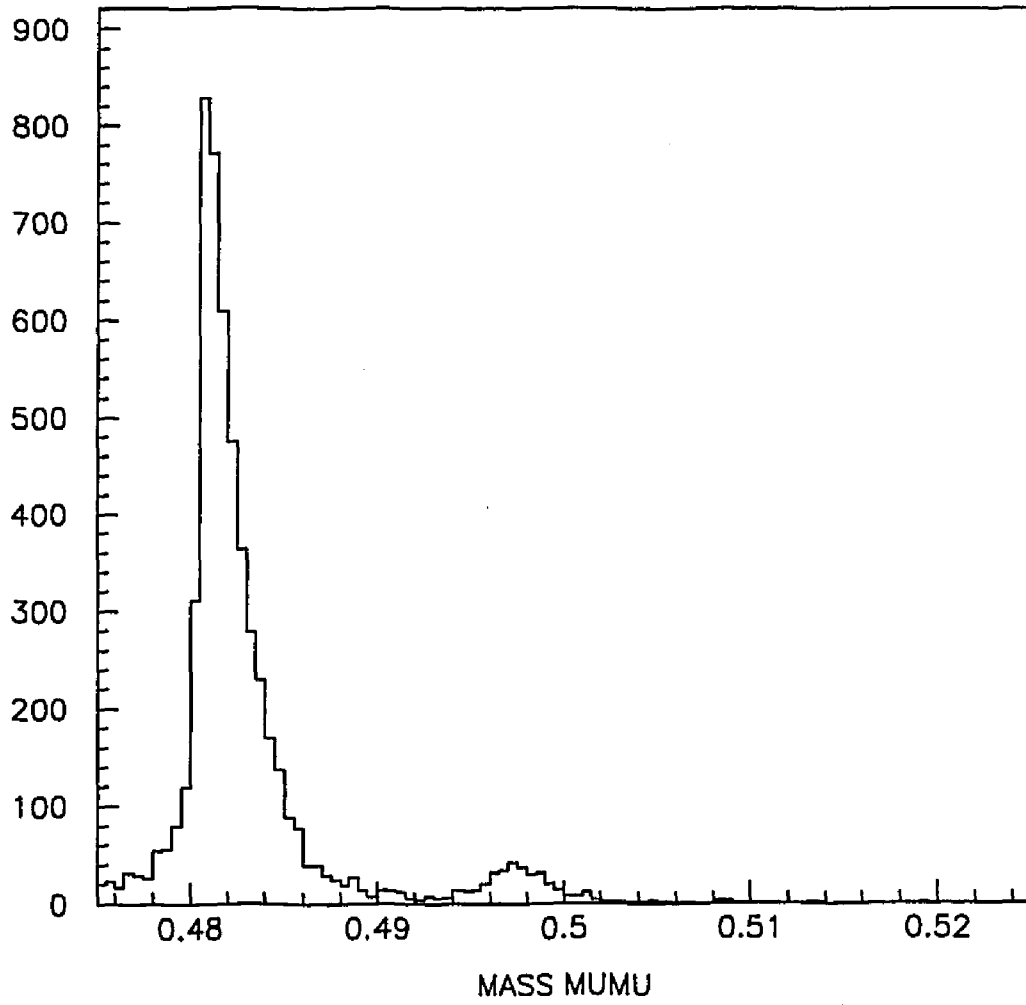


FIGURE 28

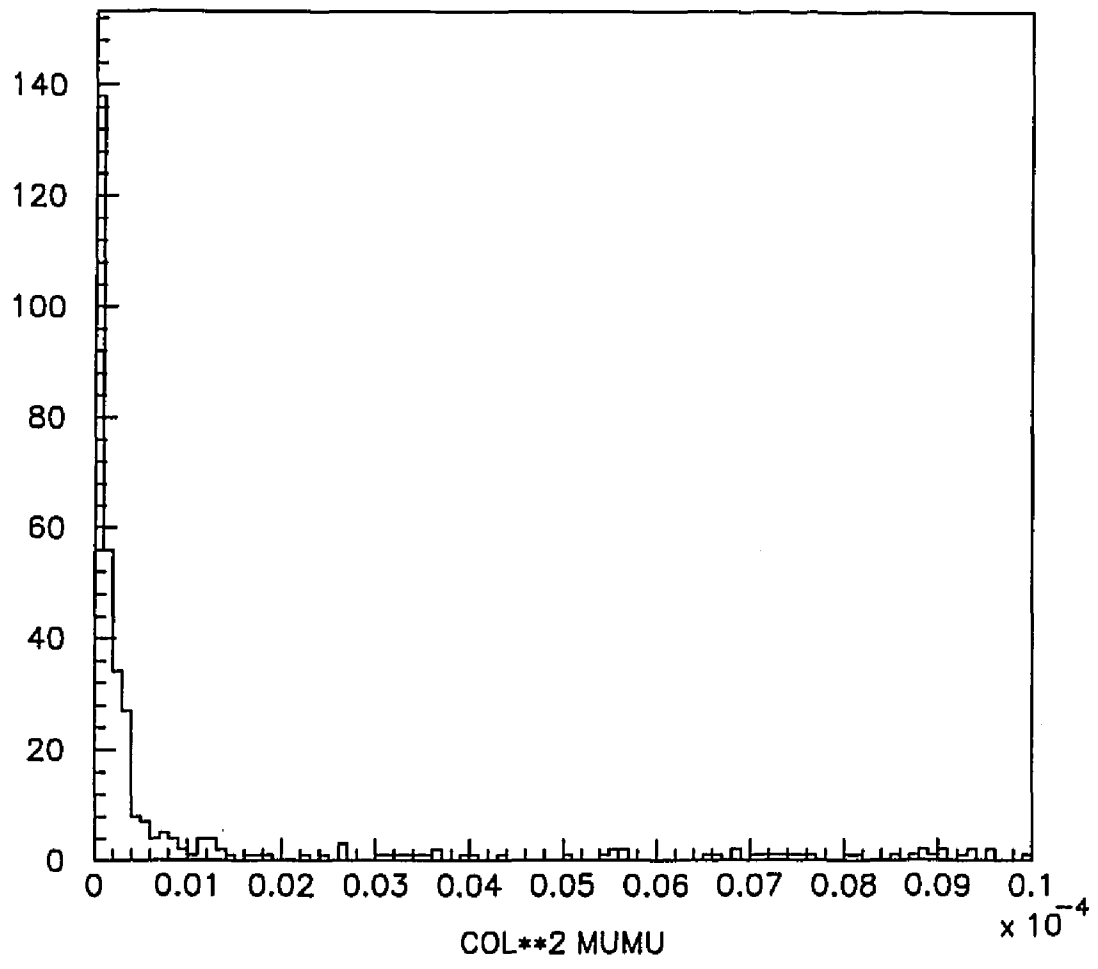


FIGURE 29

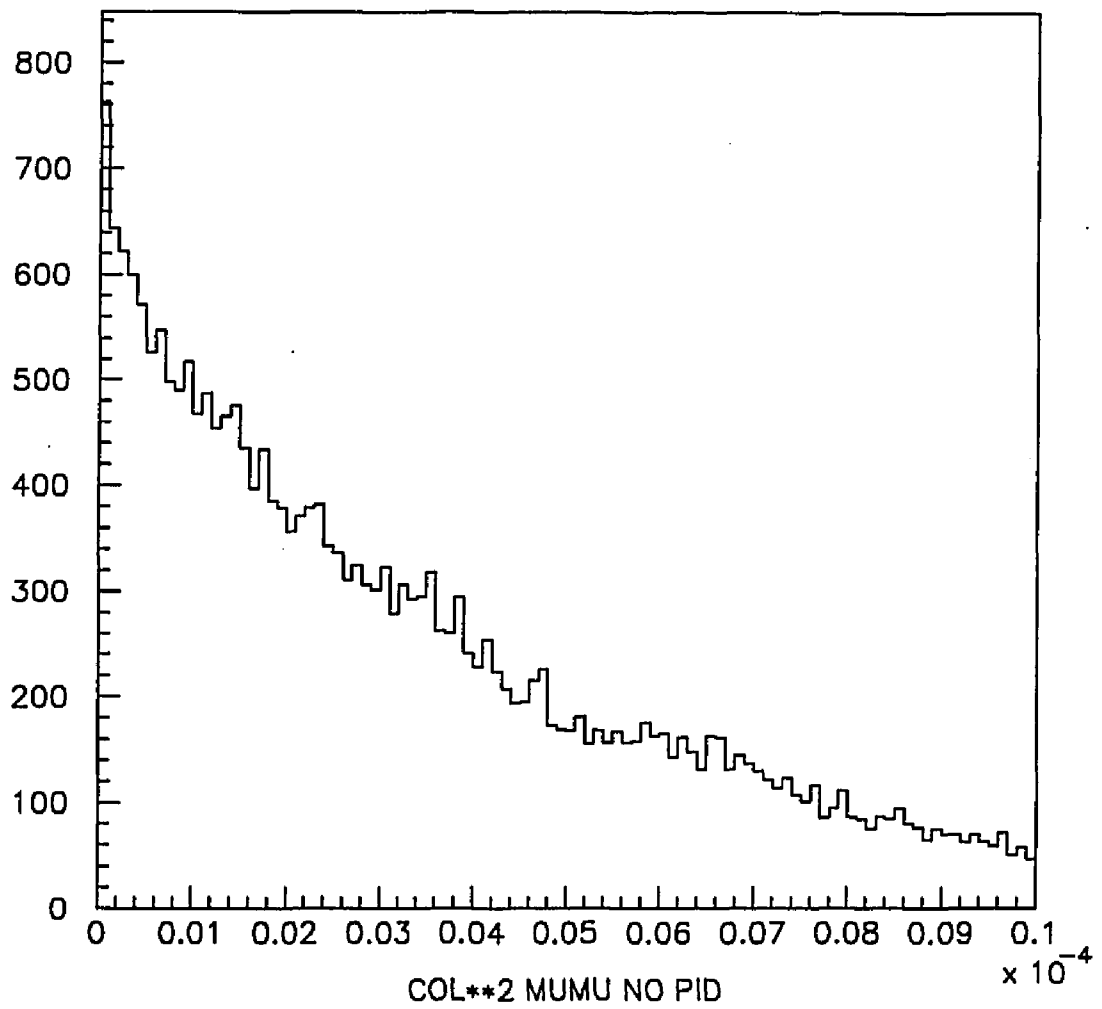


FIGURE 30

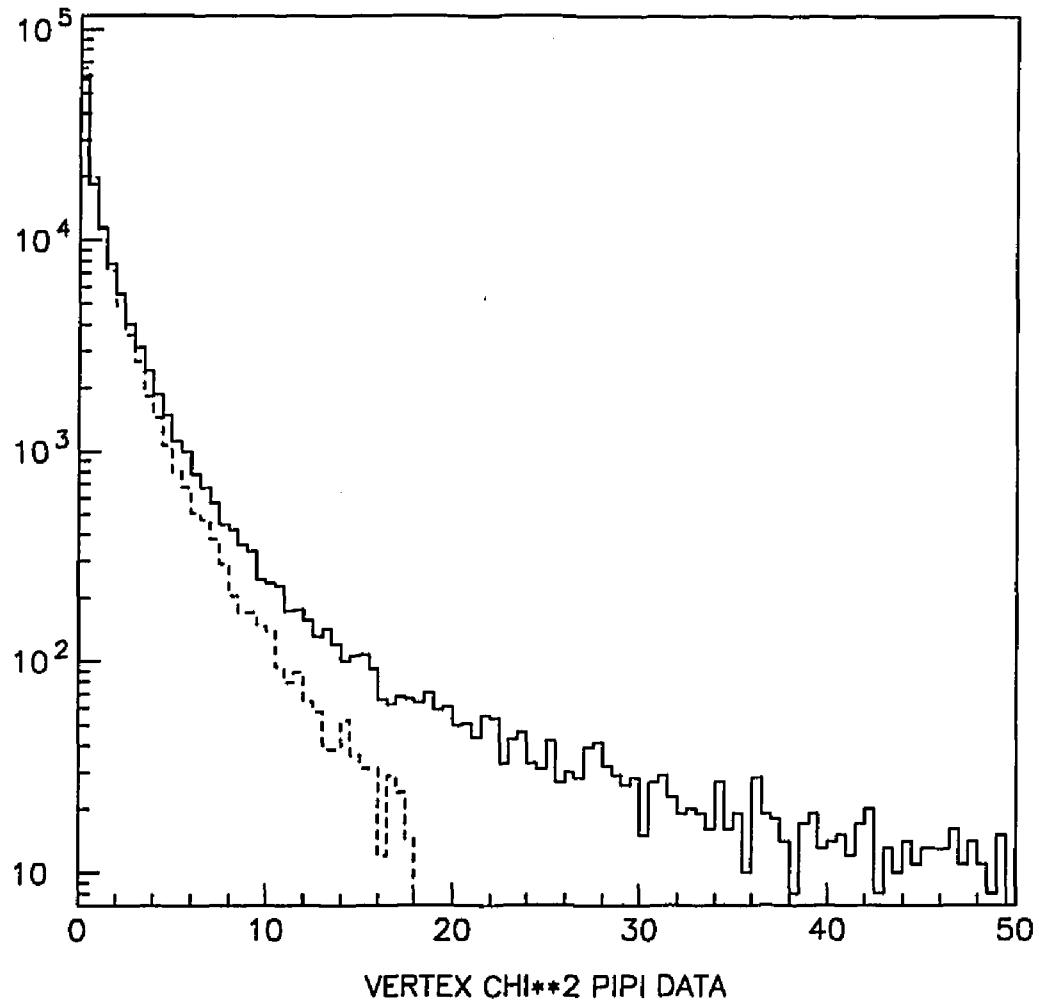


FIGURE 31

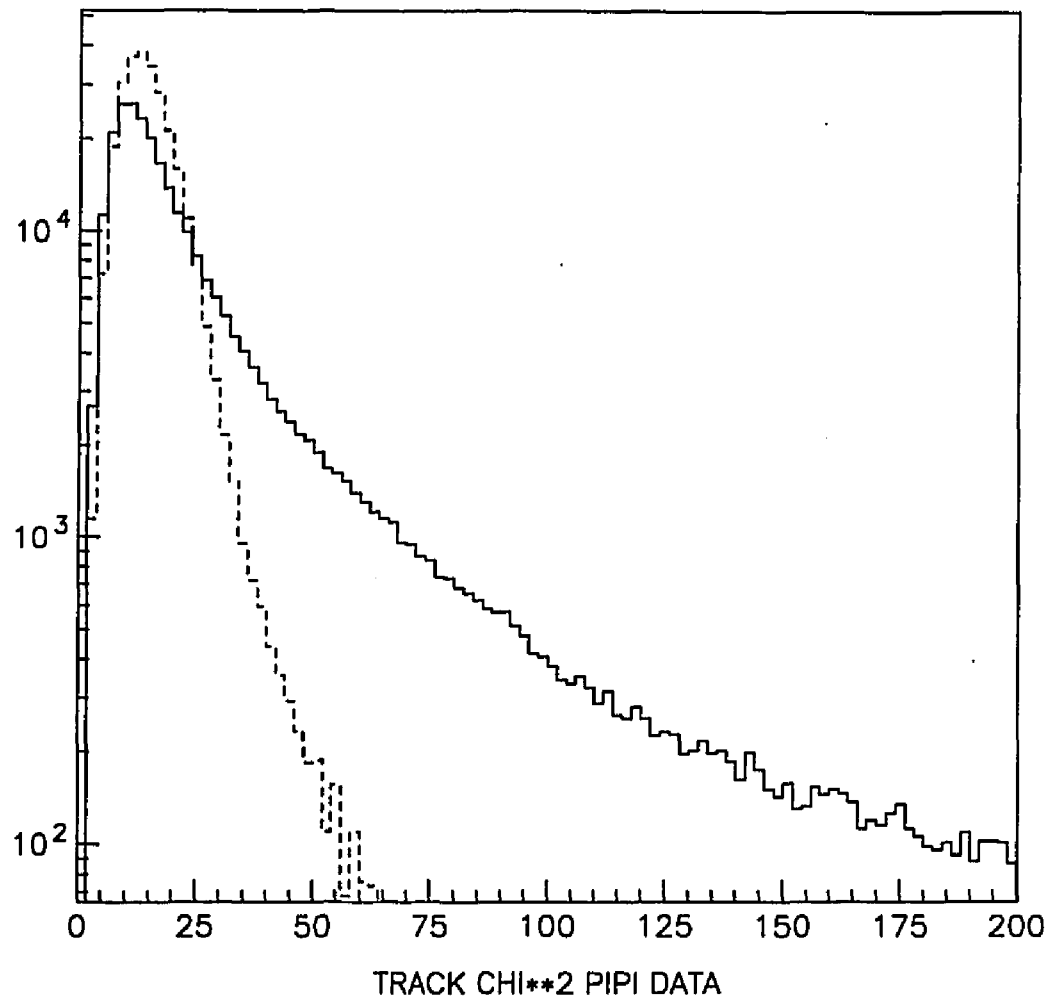


FIGURE 32

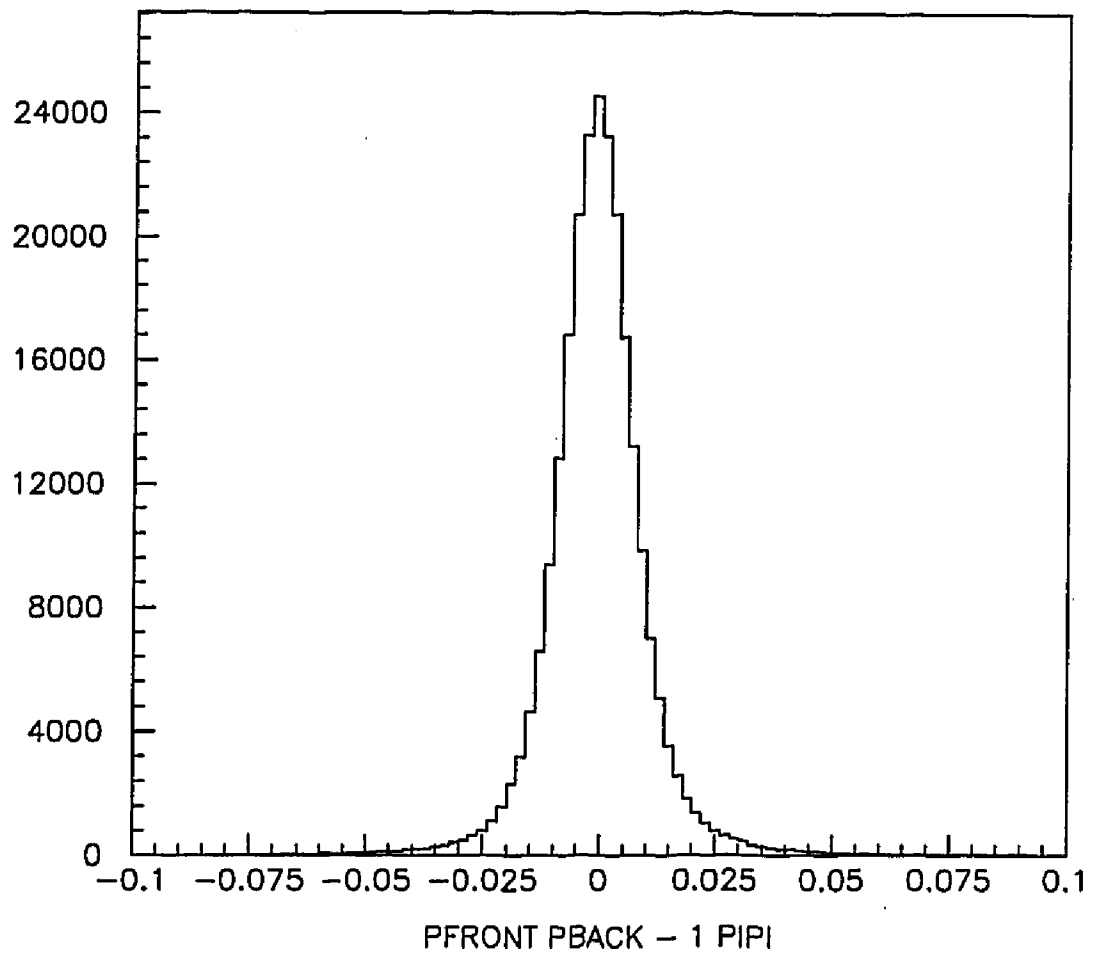


FIGURE 33

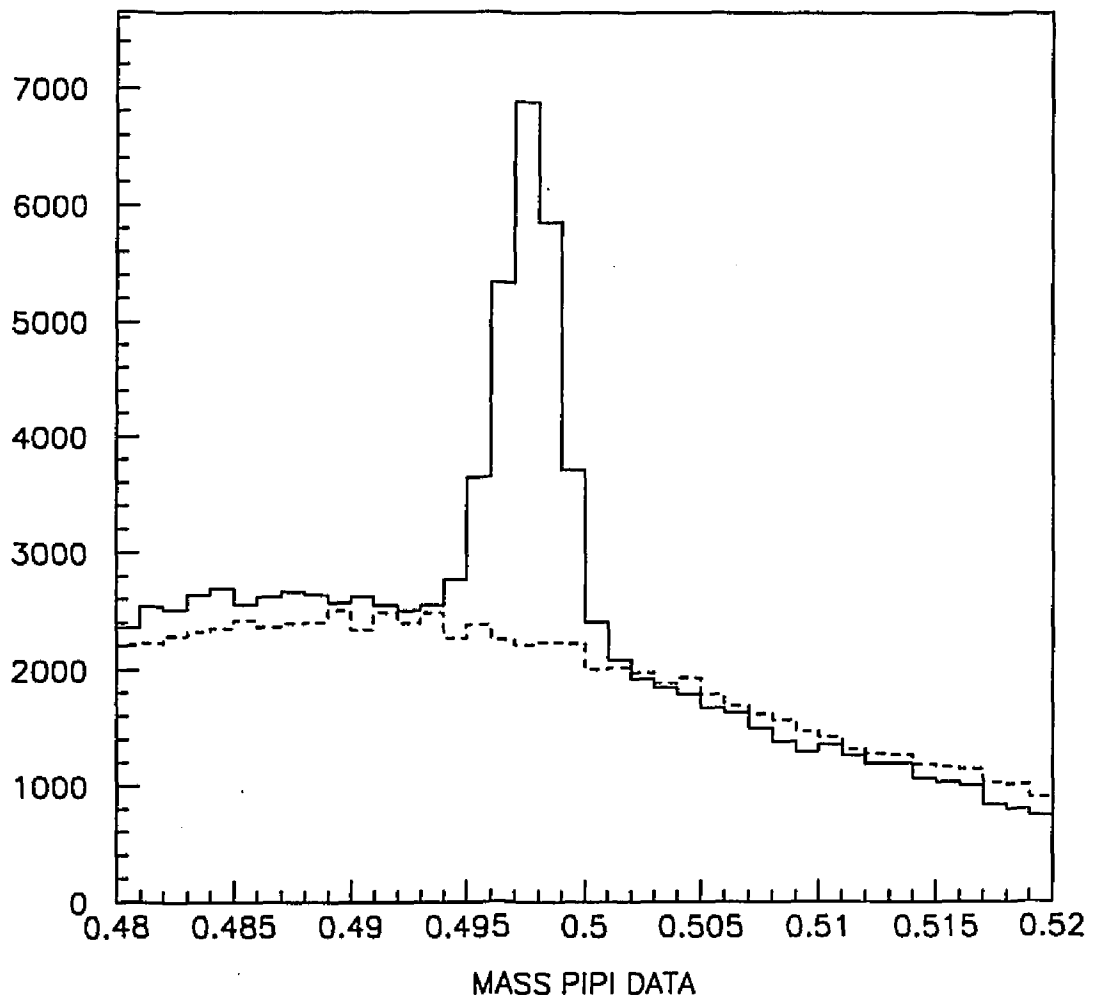


FIGURE 34

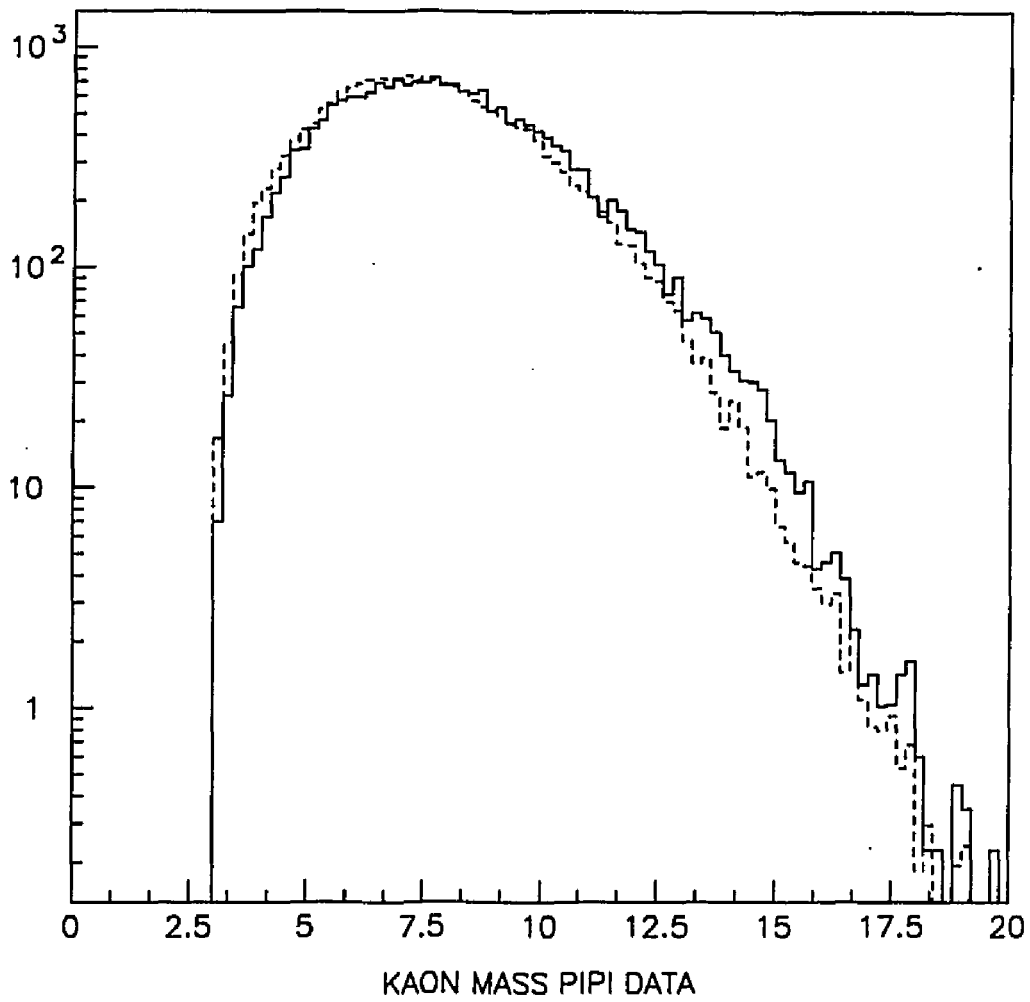


FIGURE 35

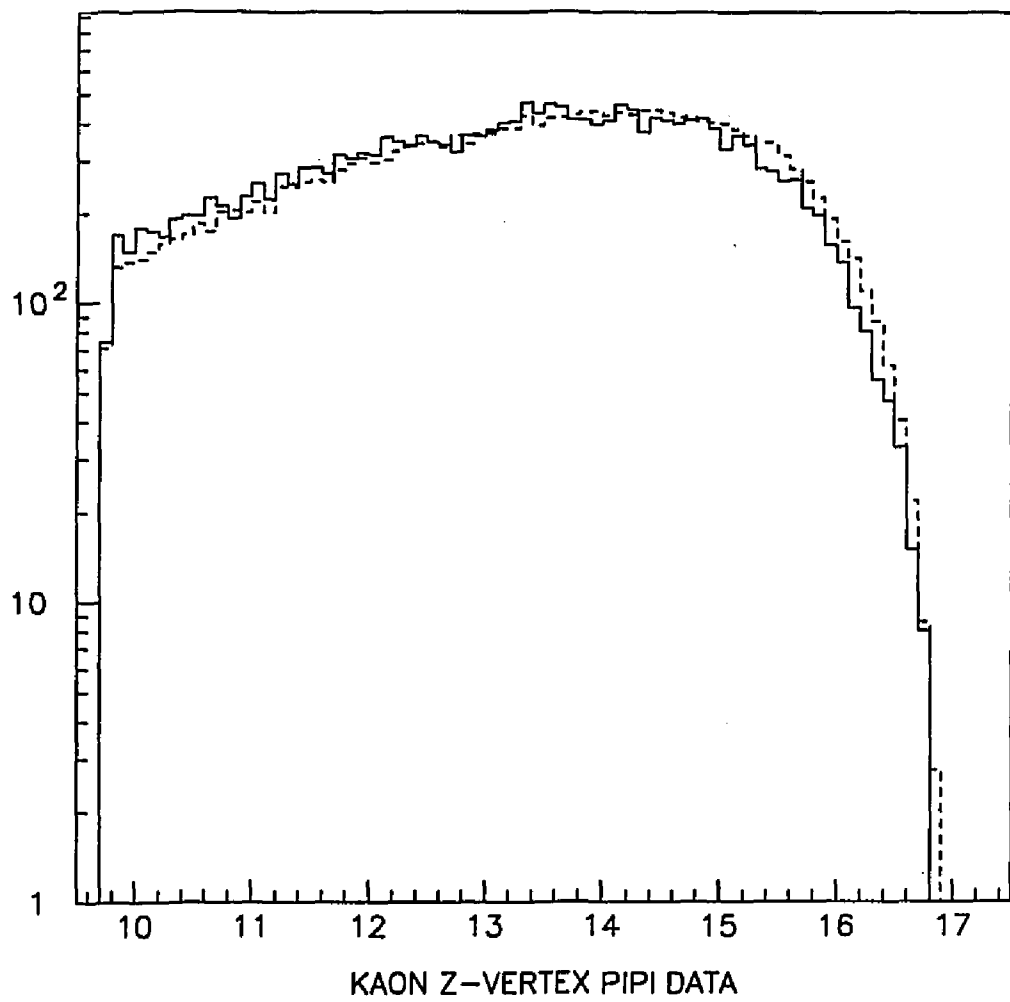


FIGURE 36

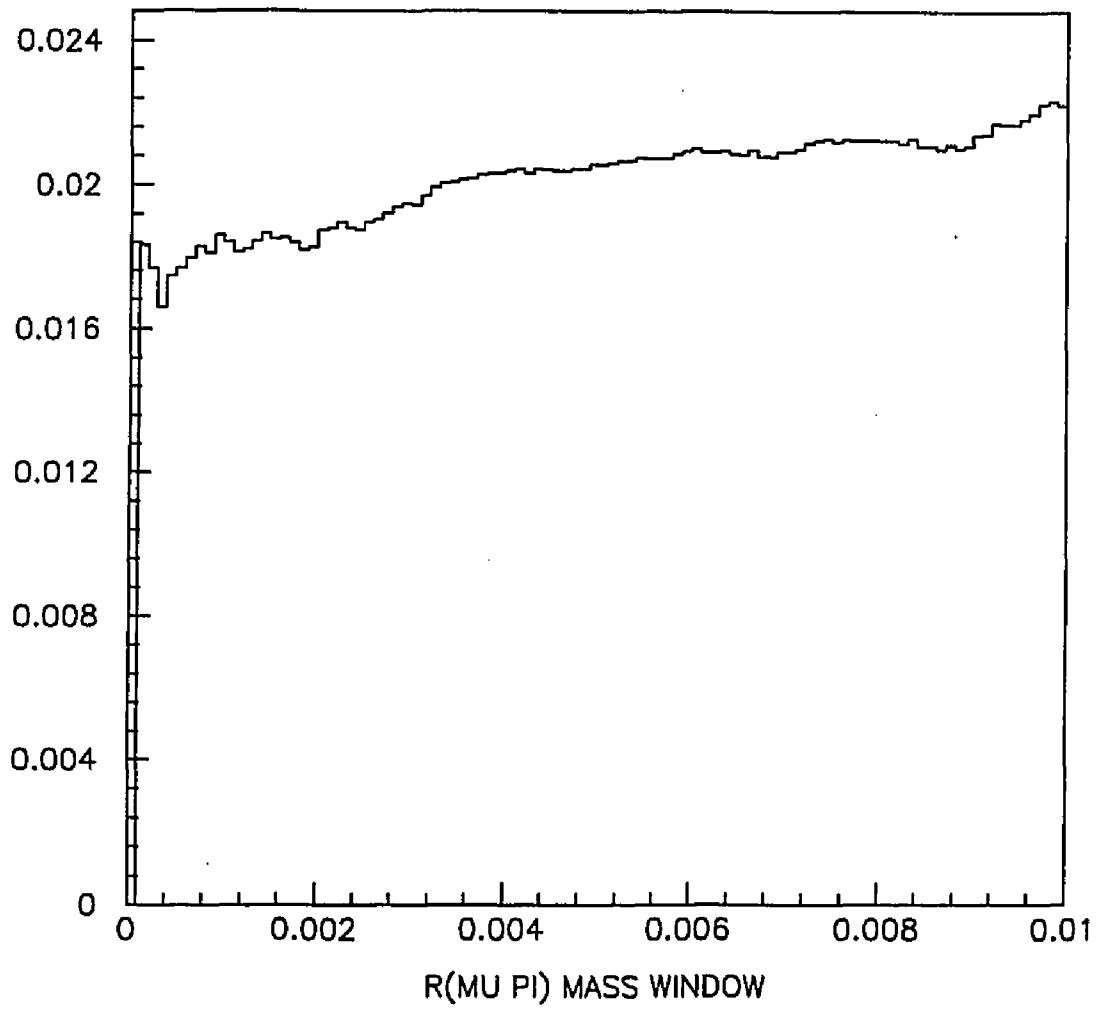


FIGURE 37

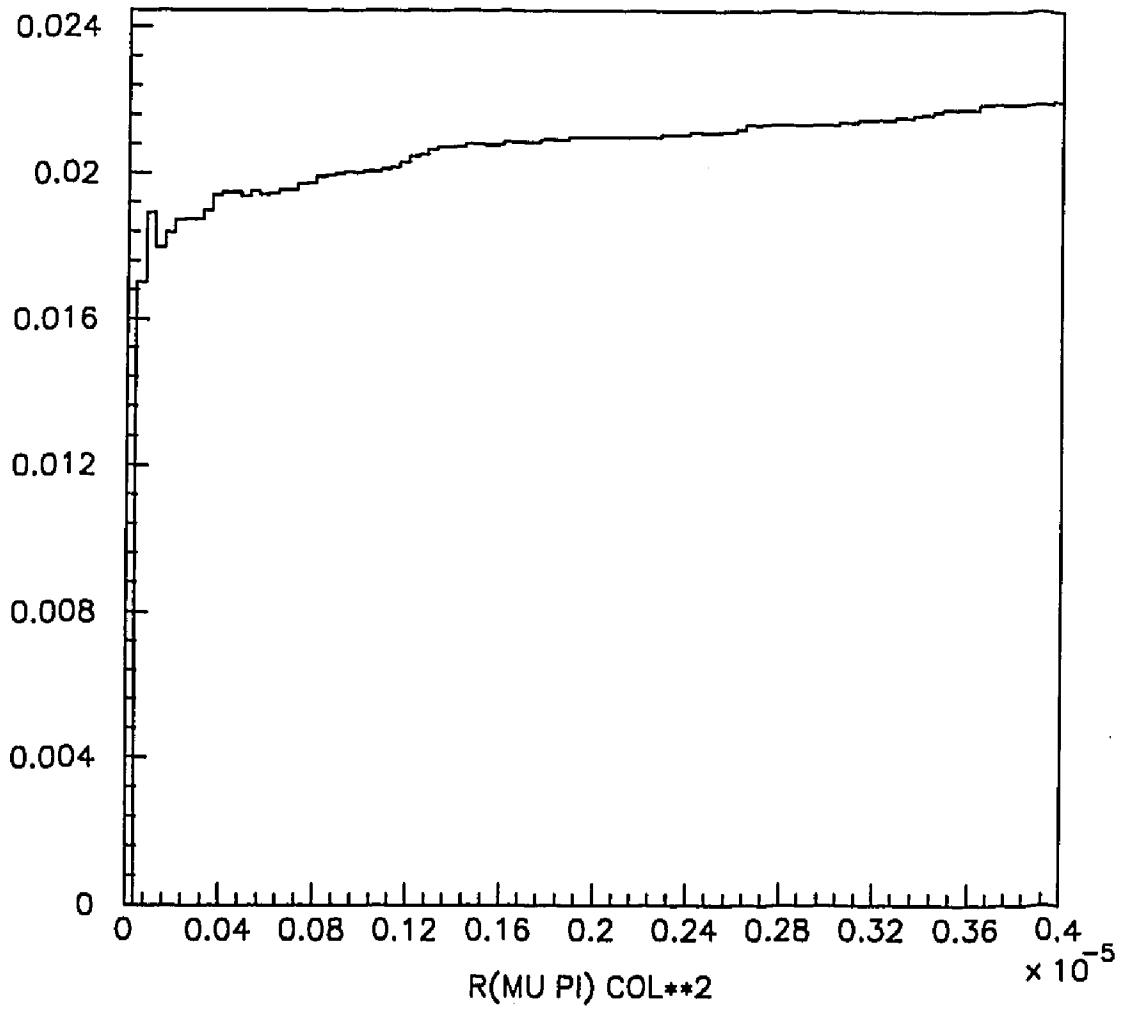


FIGURE 38

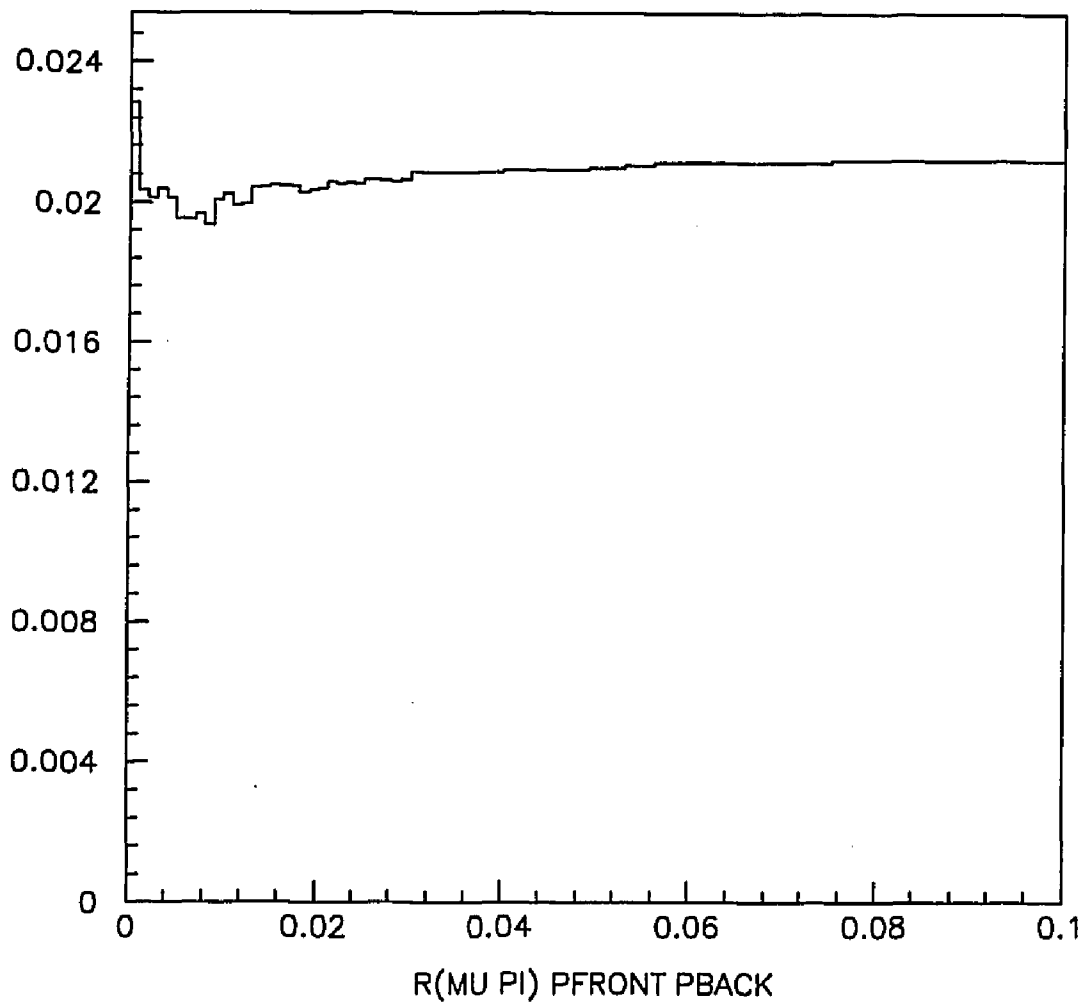


FIGURE 39

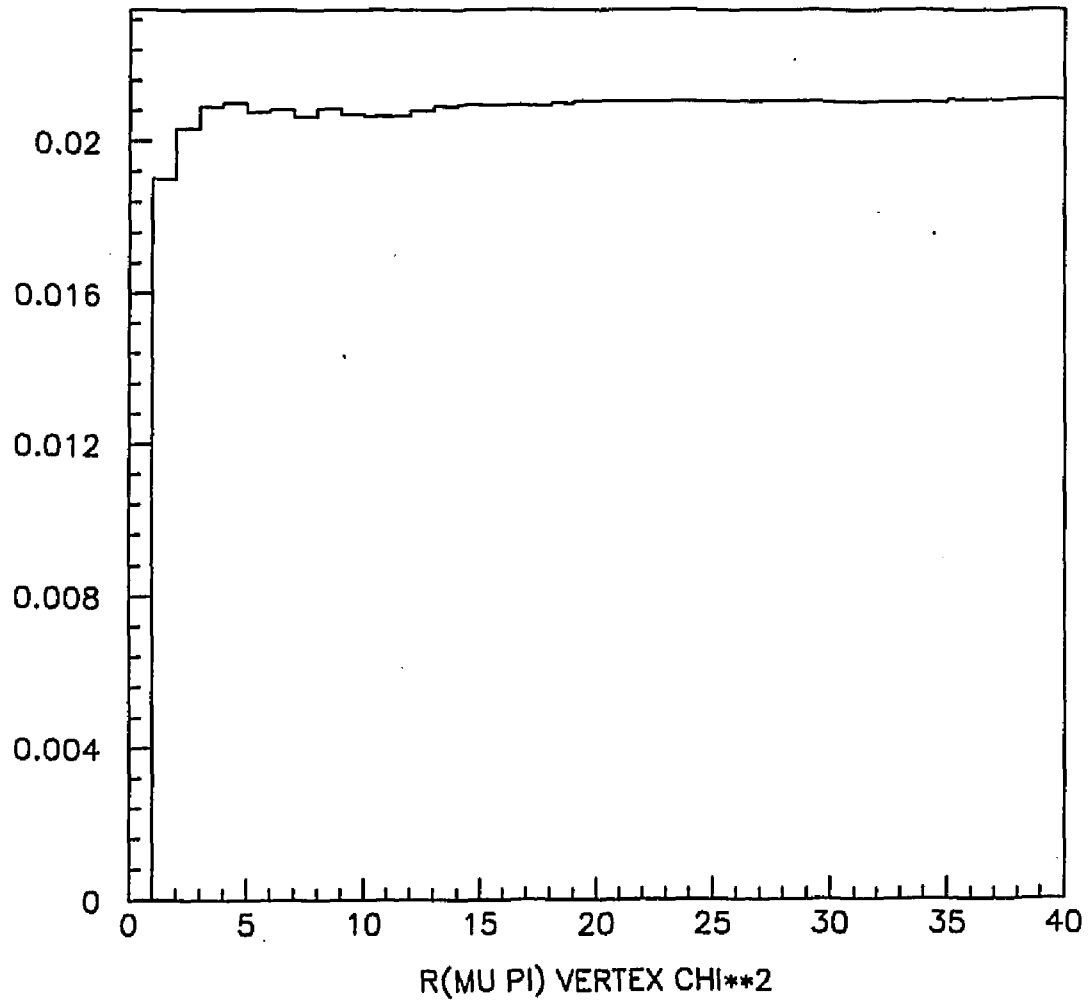


FIGURE 40

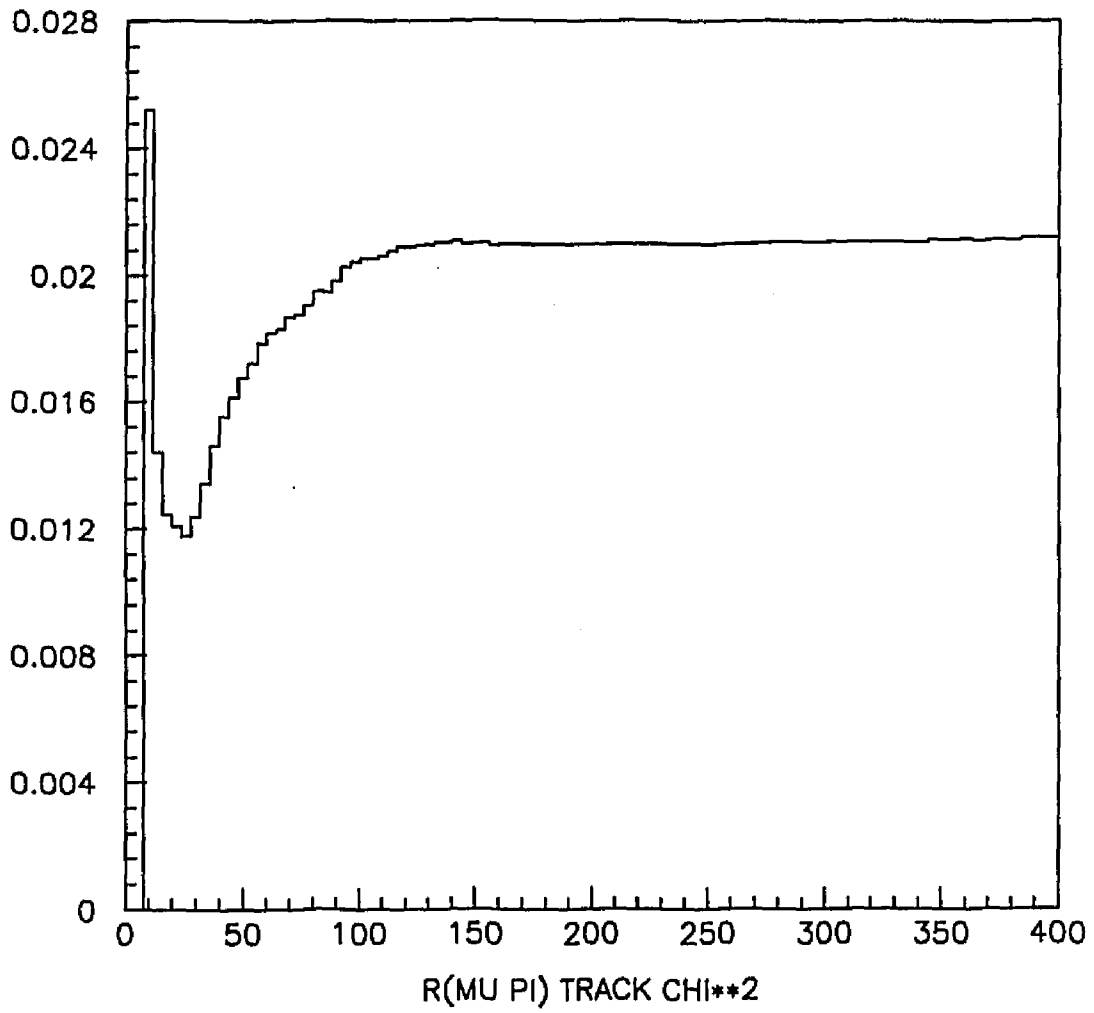


FIGURE 41

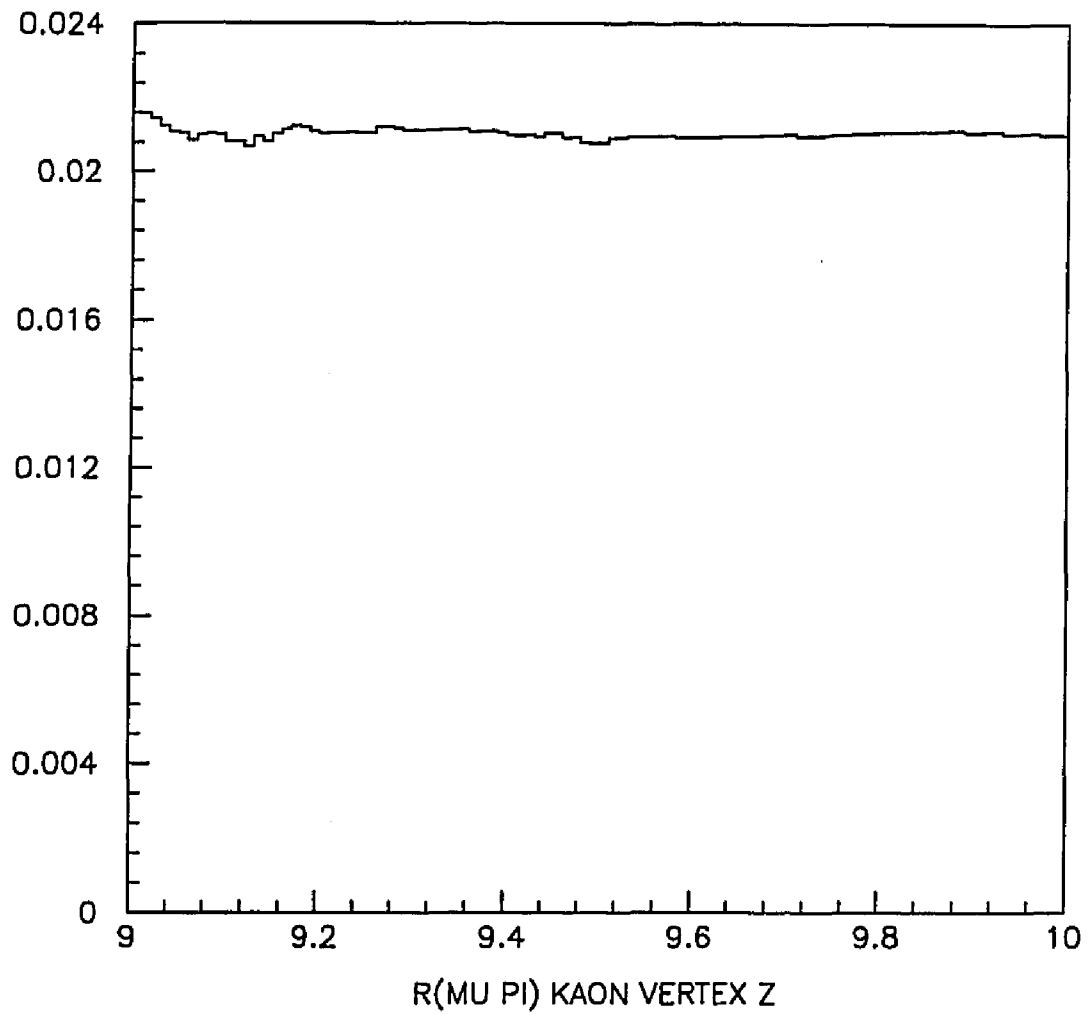


FIGURE 42

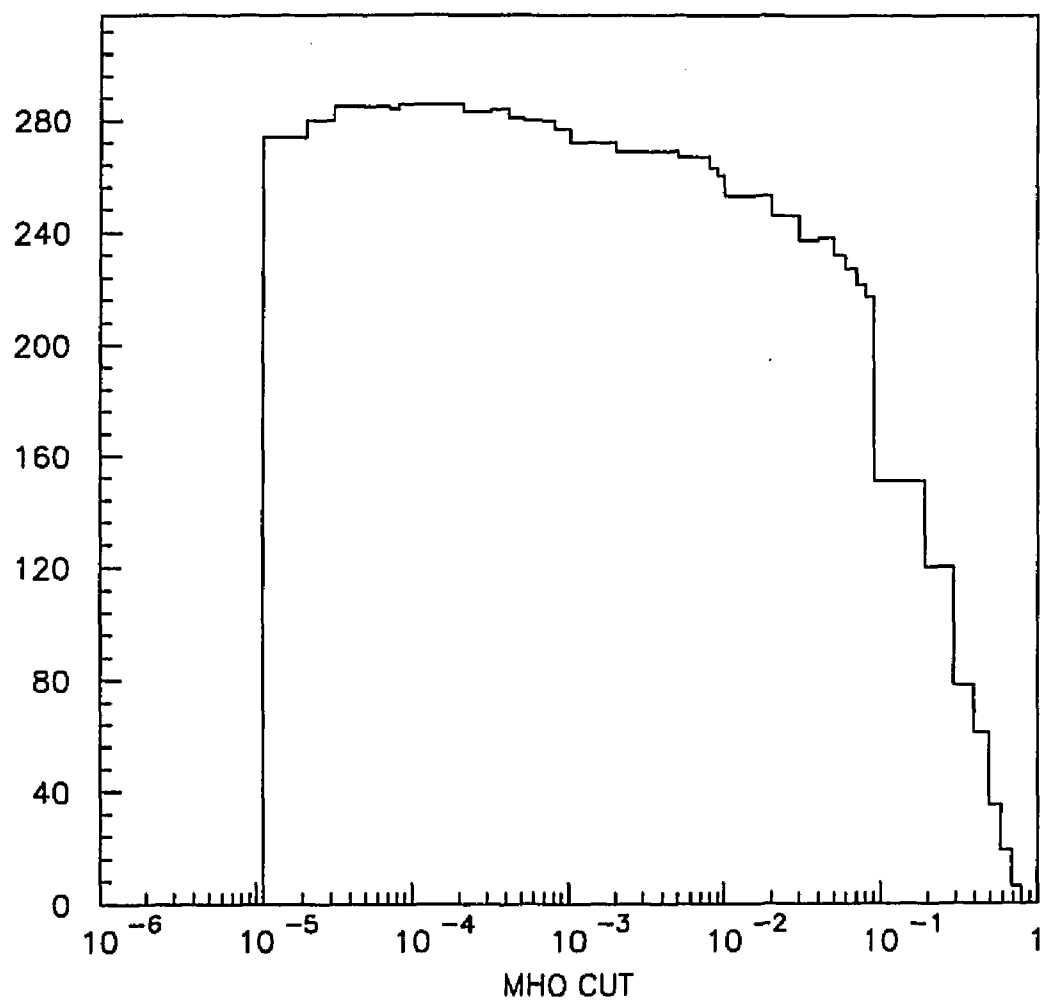


FIGURE 43

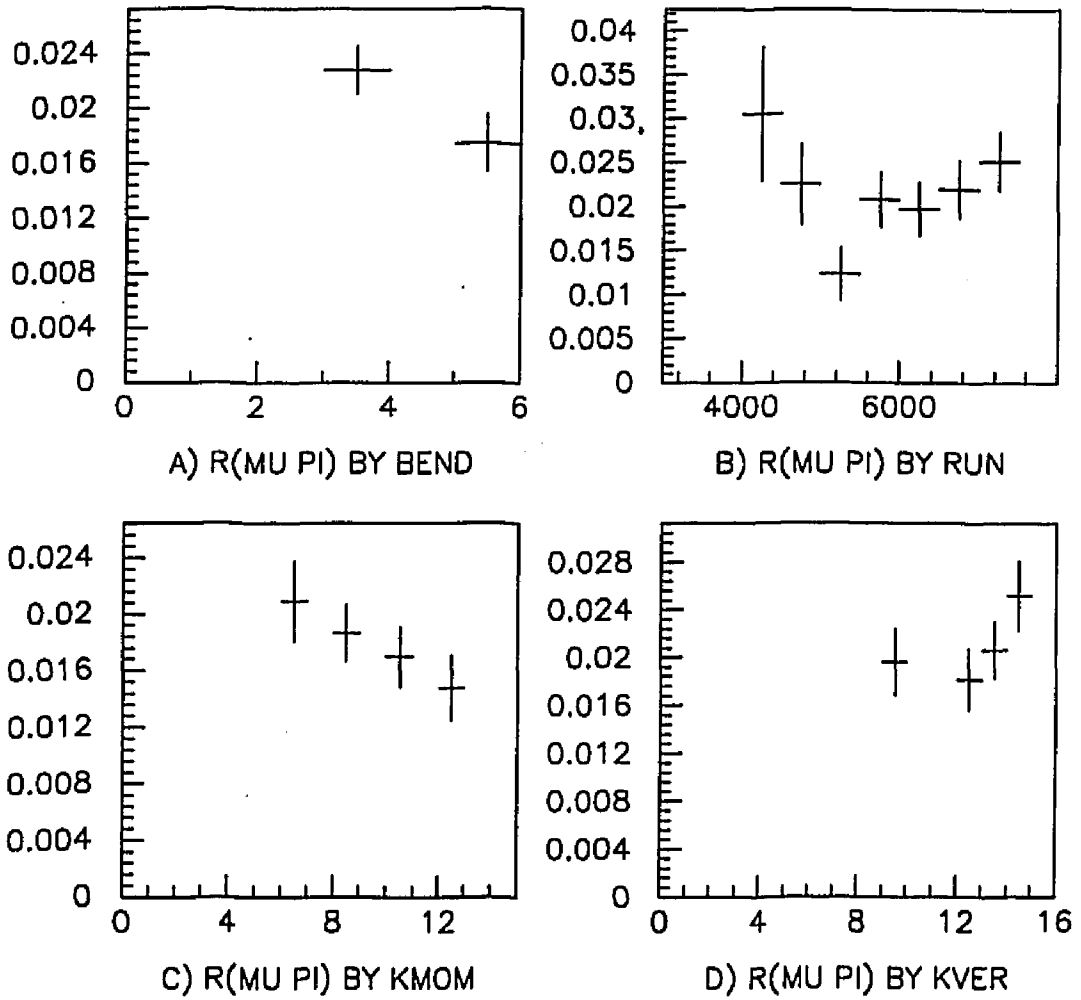


FIGURE 44

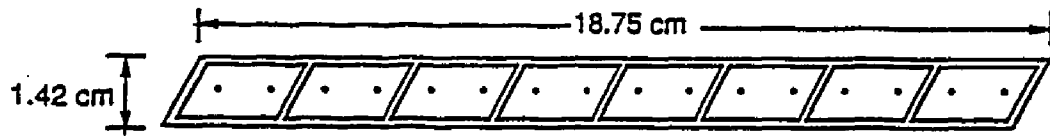
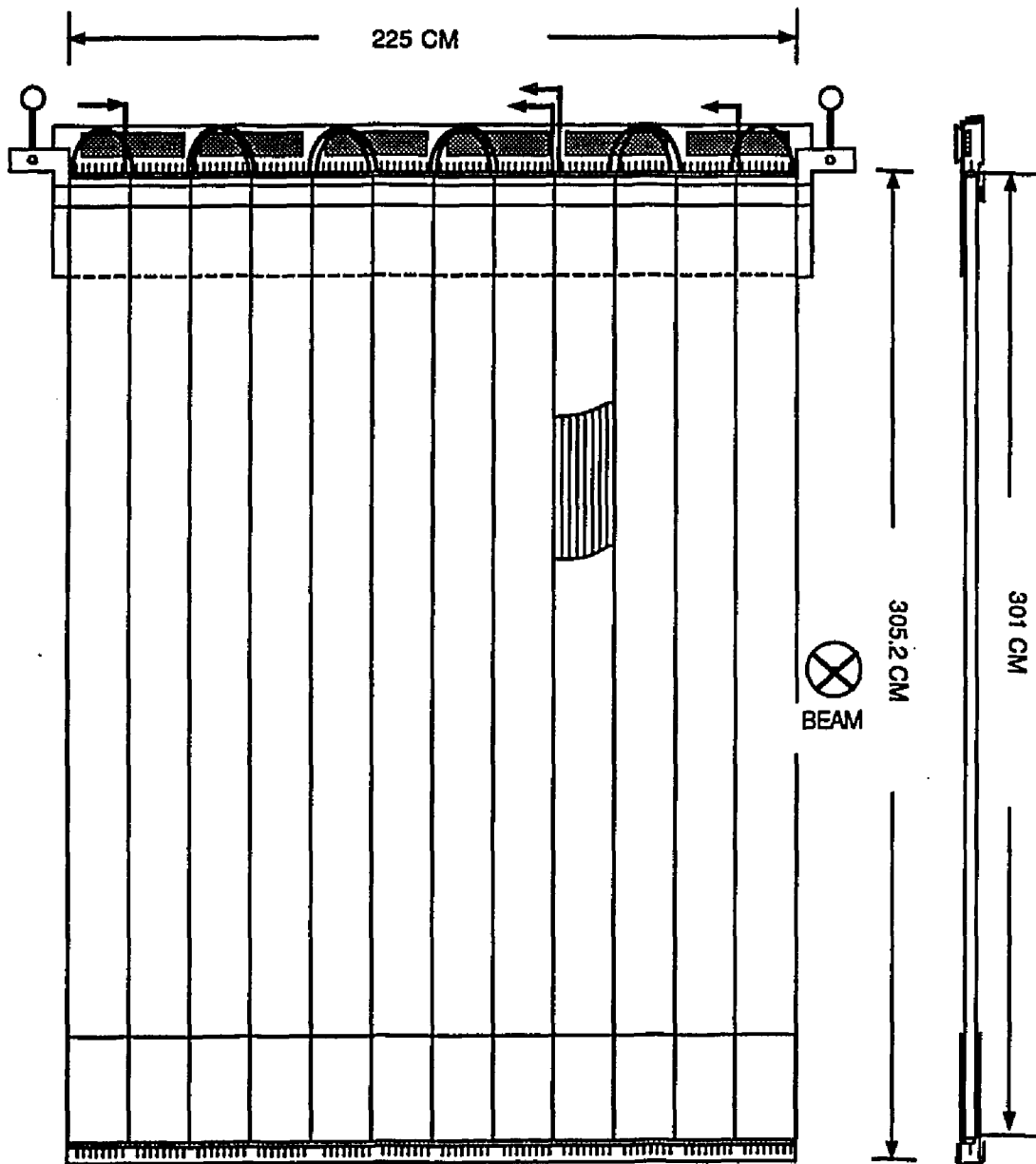
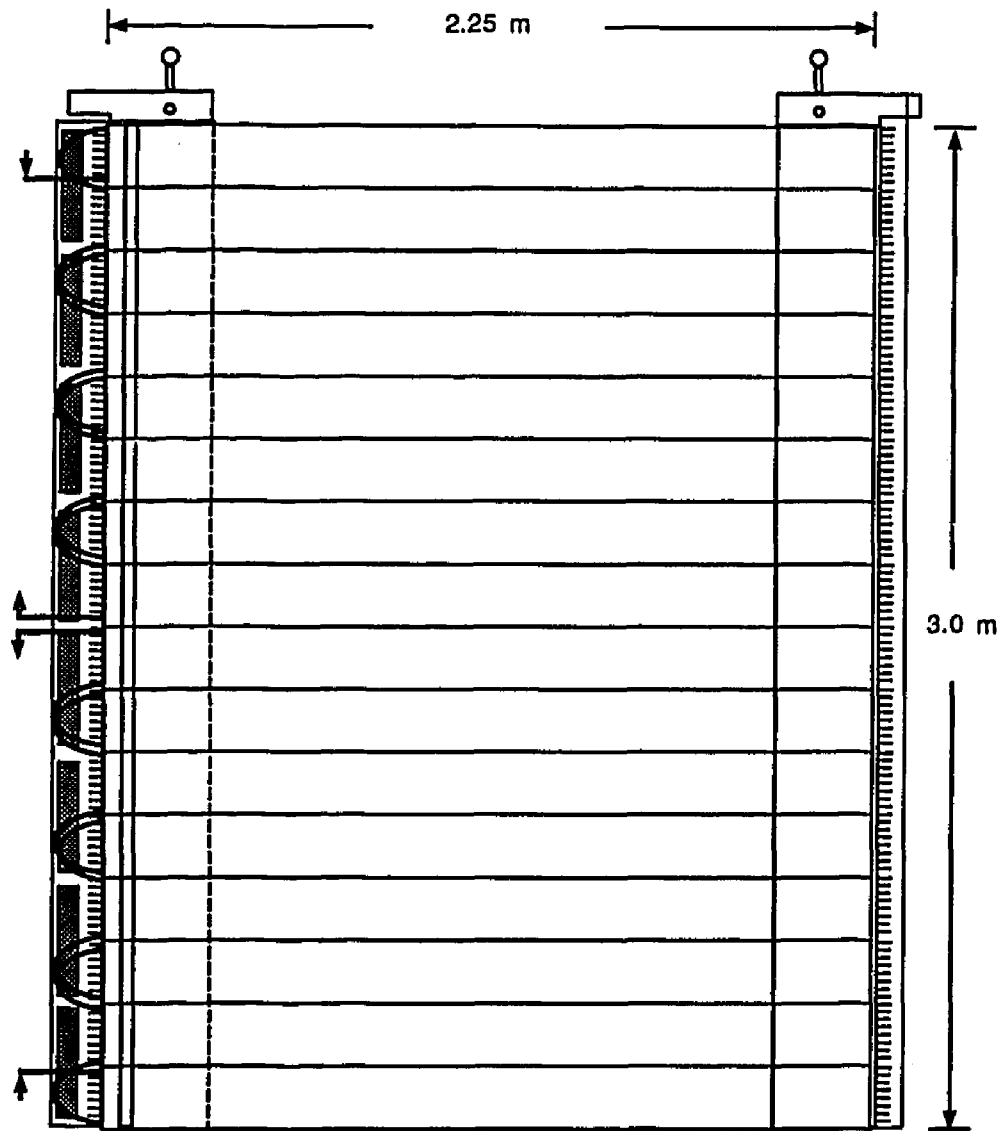


FIGURE 45



X-PLANE BEAM LEFT

FIGURE 46



Y-PLANE ASSEMBLY

FIGURE 47

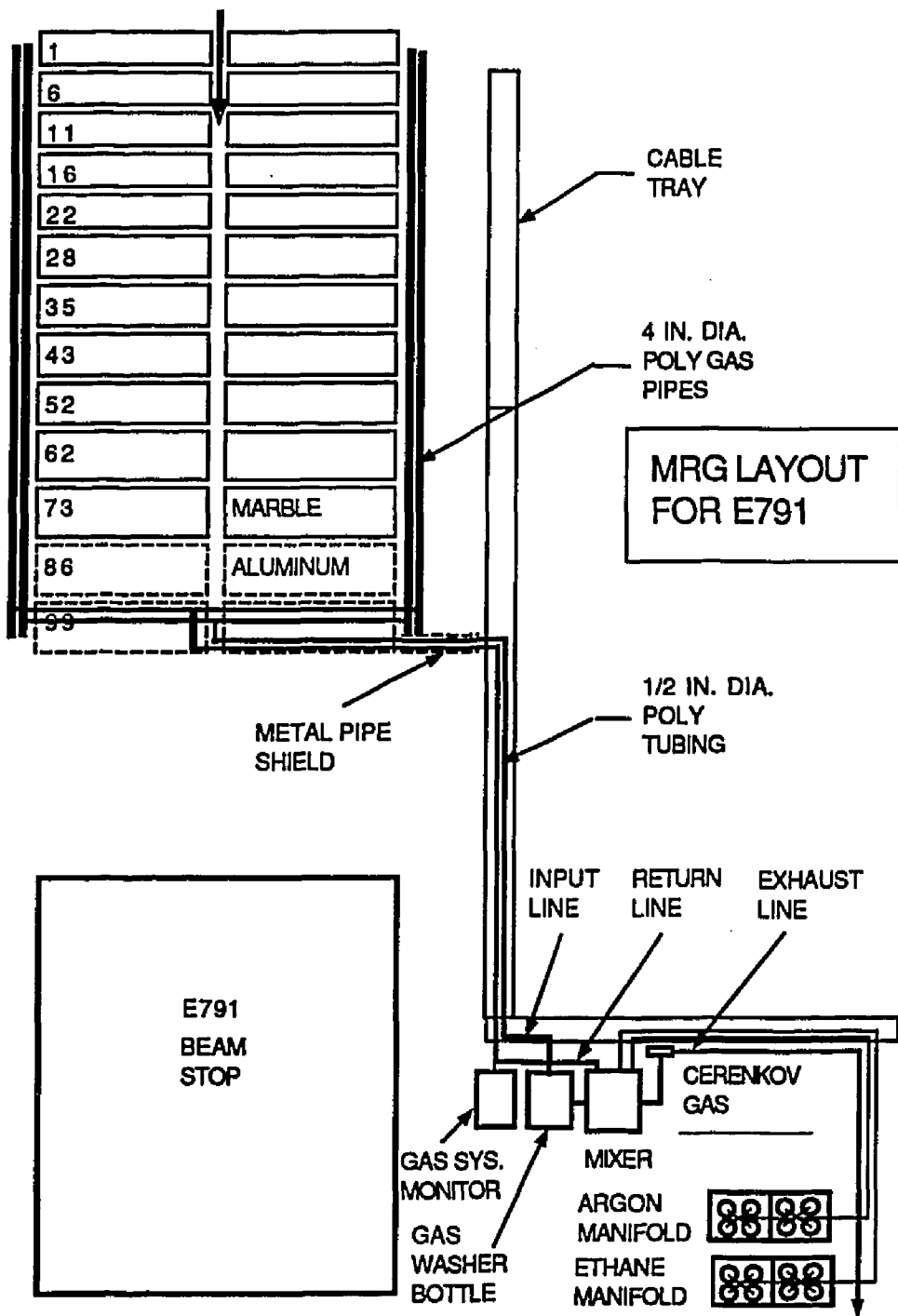


FIGURE 48

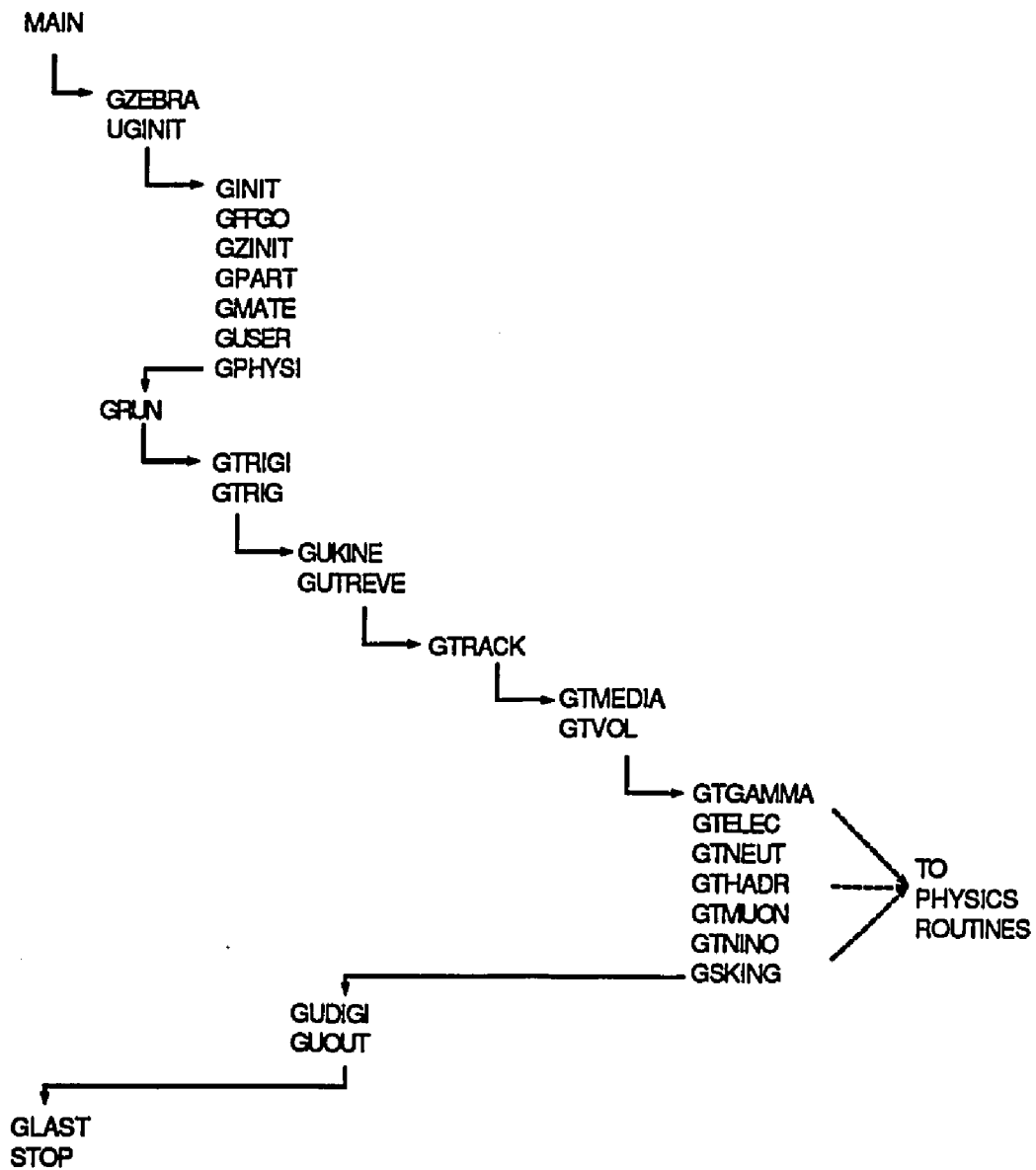


FIGURE 49

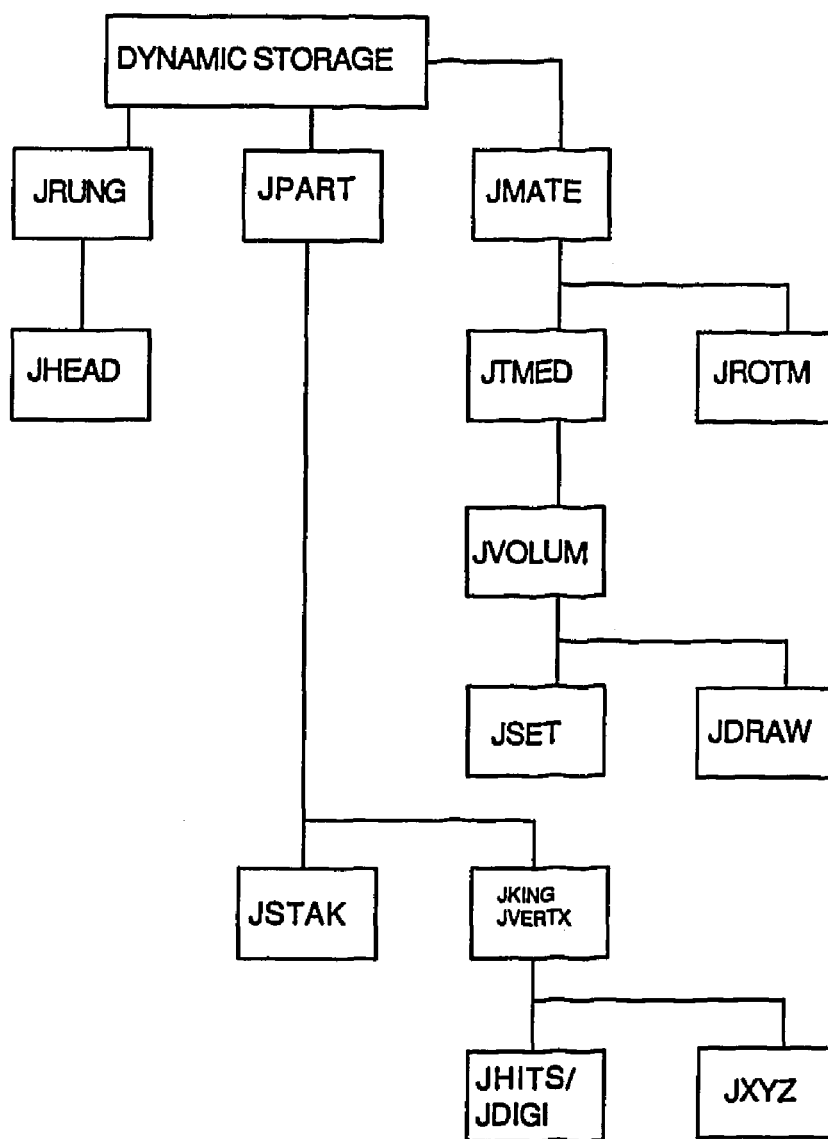


FIGURE 50

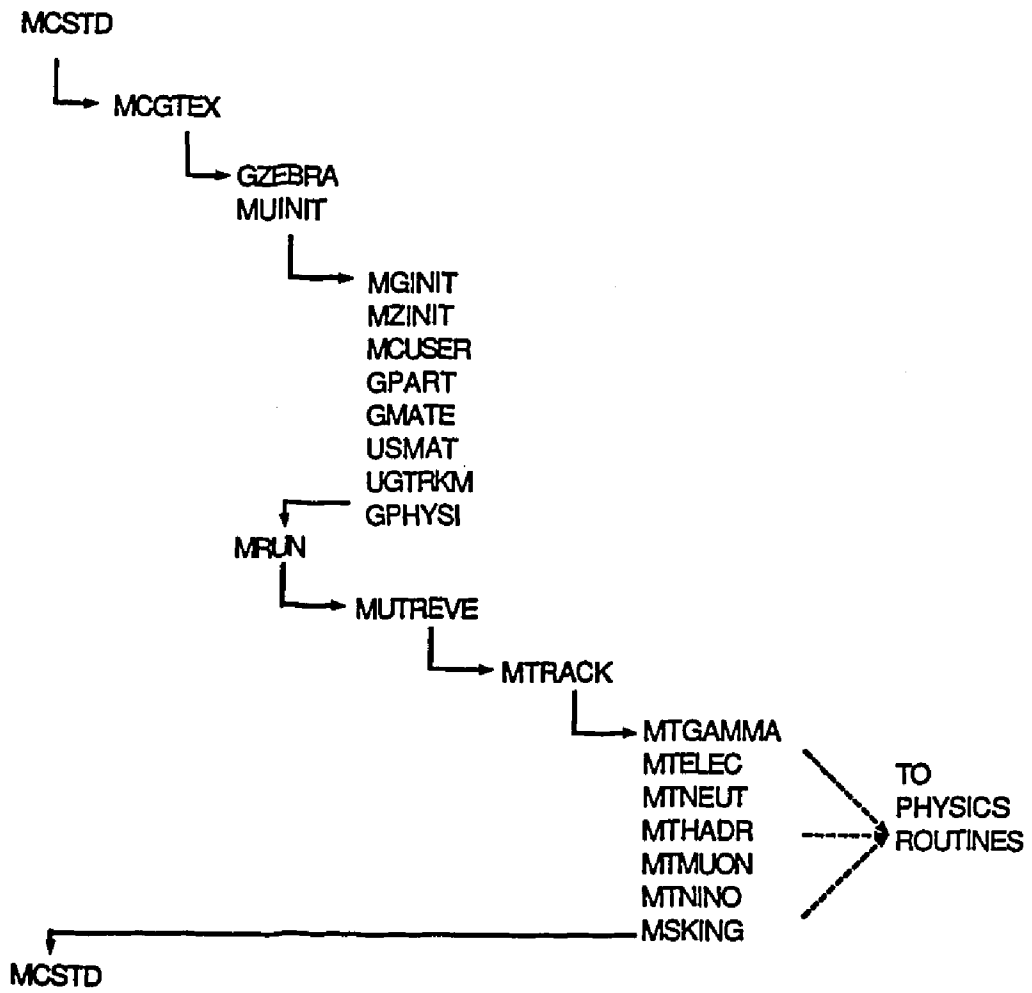


FIGURE 51

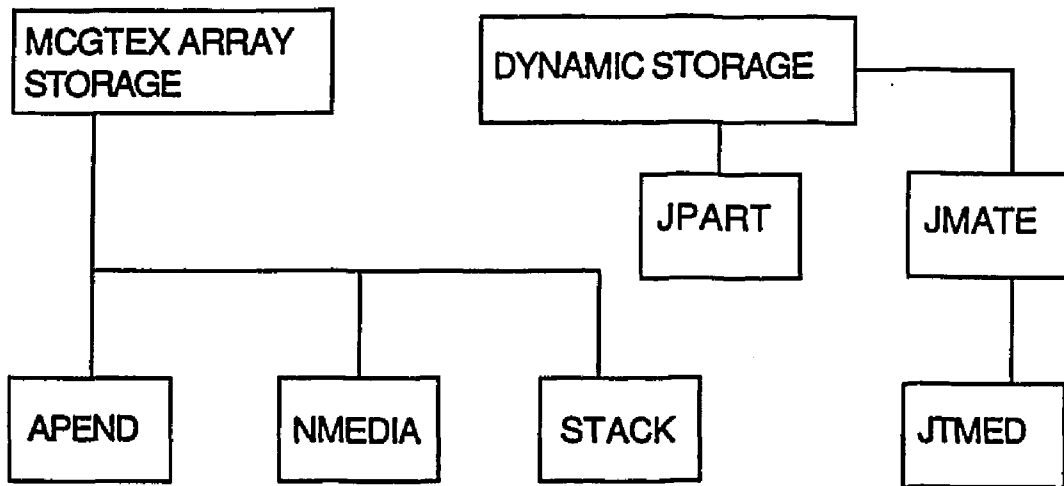


FIGURE 52

VITA

Michael David Chapman

Born in Wrightstown, New Jersey, November 27, 1962. Graduated from Miramar High School, Miramar, Florida, May 1980, B.S. in physics, Rensselaer Polytechnic Institute, 1984. In August 1984, the author entered the College of William and Mary as a graduate research assistant in the Department of Physics. Graduated with M.S. in physics, 1985, Ph.D. in high energy particle physics, 1992.